QUEEN MARY UNIVERSITY OF LONDON

PhD Thesis

Ferroelectric Barium Titanate

For Semiconductor Photocatalytic Application

Yongfei Cui

School of Engineering and Materials Science

Supervisor: Dr Steve Dunn

Submitted in partial fulfilment of the

requirements of the Degree of Doctor of Philosophy

Declaration

I, Yongfei Cui, confirm that the research included within this thesis is my own work or that where it has been carried out in collaboration with, or supported by others, that this is duly acknowledged below and my contribution indicated. Previously published material is also acknowledged below.

I attest that I have exercised reasonable care to ensure that the work is original, and does not to the best of my knowledge break any UK law, infringe any third party's copyright or other Intellectual Property Right, or contain any confidential material.

I accept that the College has the right to use plagiarism detection software to check the electronic version of the thesis.

I confirm that this thesis has not been previously submitted for the award of a degree by this or any other university.

Signature:

Date:

2015-09-09

Abstract

Semiconductor photocatalysis has received extensive attention due to its wide applications in water and indoor air purification, solar fuel production, etc. Charge carrier separation is a crucial step in semiconductor photocatalysis and influences the overall efficiency. It has been demonstrated that internal depolarisiation field of ferroelectric materials can drive spatial separation of charge carriers, which results in spatial separation of reduction and oxidation reactions, and improved charge carrier separation. In this thesis, ferroelectric barium titanate was chosen and its photocatalytic performance in decolourisation of organic dye molecules was investigated.

Photodeposition method was adopted to deposite silver nanoparticles on the surface of barium titanate. Silver modified barium titanate showed increased photodecolourisation rate compared with bare barium titanate due to its role of electron traps and hindered charge carrier recombination. A simple thermal treatment was used to alter the phase composition of the as-received barium titanate. Samples which contained more ferroelectric tetragonal phase were found to possess higher photocatalytic activity compared with non-ferroelectric samples. This was associated with stronger ferroelectricity after thermal treatment, which enhanced dye molecule adsorption and aid charge carrier separation.

The mechanism and intermediates generated in photodegradation of Rhodamine B with silver modified ferroelectric barium titanate were studied. Cleavage of chromophore was demonstrated to dominate in the initial process. Benzoic acid was identified as the main intermediate and no siginificant discrepancy in intermediates distribution between ferroelectric photocatalytic system and non-ferroelectric system was observed.

The influence of ferroelectric dipole of barium titanate on photocatalytic activity of heterostructured barium titanate/hematite was also studied. The synthesised

heterostructured barium titanate/hematite showed higher photodcolourisation rate than both barium titanate and hematite. This phenomenon was attributed to the improved charge carrier separation and extended charge carrier lifetime arising from heterojunction and an interaction between the ferroelectric dipole and the carriers in the hematite.

Contents

List of Figures

List of Tables

Chapter 1

Introduction

1.1 Background

With the rapid development of human civilization, the discharge of industrial effluent containing organic pollutants is becoming a serious challenge all over the world as it severely deteriorate our freshwater resources. Various efforts are being made to remove these pollutants, including filtration, sorption processes, biological treatment, catalytic oxidation, and combination treatments[1]. The ideal technique should chemically transform these toxic pollutants into non-hazardous compounds efficiently and eco-friendly[2]. Among these techniques, semiconductor photocatalysis is regarded a novel strategy to degrade and remove hazardous compounds in the air and water through utilizing abundant solar energy[3,4] .

When a semiconductor photocatalyst is exposed under super-band-gap irradiation, electrons will be excited from valence band to its conduction band, leaving equal number of holes in valence band. Then these electons and holes can migrate to the surface, and involve in the reduction and oxidation reactions with adsorbates (H_2O and/or O_2 in the case of organic dye solutions), generating highly reactive species, e.g. hydroxyl radical $OH\cdot$, superoxide anion radical $O_2^-\cdot$, etc.. These active species can further mineralize orgainic dye molecules into mineral salts, CO_2 and H_2O and achieve water purification[5,6]. Meanwhile, the photoexcited electrons and holes can also recombine with each other during transportation from bulk to the surface, which will dissipate the energy in the form of heat or emitted light.

However, the prospect of efficient photocatalysis has not been reached which limits the industrial application of semiconductor photocatalysis. Taking hydrogen generation

through solar-driven water splitting using a particulate system as an example, it was proposed the quantum efficiency should achieve 30% at 600 nm for practical applications[7]. However the state-of-the-art is, at most, quantum efficiency of a few percentage at wavelength as long as 500 nm[7]. Therefore, how to increase the photocatalytic efficiency is still a big challenge. There are a number of factors limiting the efficiency of the photocatalyst, e.g. the low utilisation of visible light. Due to the large band gap of semiconductors, e.g. TiO_2 with a band gap 3.0-3.2 eV, it can only be excited by 3%-5% of solar irradiation[8,9]. The other bottleneck is the recombination of photoexcited electrons and holes. A high rate of recombination between electrons and holes reduces the amount of carriers available for photochemical reactions, and decreases the photo-efficiency of the system[10]. In addition, redox reactions occur in close proximity on the surface of the catalyst. This enables back reactions to proceed where products react to form the original starting species and so the equilibrium is not pushed toward final products[11].

Different materials and methods to overcome the factors mentioned above have been developed[12–14], e.g. surface decoration by noble metal nanoparticles, band-gap engineering, heterojunction between two semiconductors with appropriate band gaps, etc.. Despite this, the lack of significant progress with the existing materials encourages searching for new materials to make an impact in the area of photocatalysis. Ferroelectric materials may be this new candidate.

Ferroelectric materials have been regarded as wide band gap semiconductors for some time[15]. A ferroelectric material possesses a spontaneous polarisation arising from the displacement of the centre of the positive and negative charges in a unit cell[16]. The spontaneous polarisation induces macroscopic charges on the surface of ferroelectrics and the internal depolarisation field will drive charge carriers to flow in opposite directions,

further resulting in spatial separation of oxidation and reduction reactions[17–19]. The surface charge can be compensated by free charge carriers and defects in the ferroelectric bulk (internal screening) and/or by the adsorbed charged molecules from the environment (external screening)[20,21]. In addition, the spontaneous polarisation of ferroelectric materials can have interactions with dipoles of adsorbed molecules, decreasing the energy required to break bonds[22,23]. All these elements combine and make ferroelectrics intriguing materials which can be applied in photocatalysis.

1.2 Aims and objectives

Ferroelectric materials acting as photocatalysts is still an emerging research field, and the aim of this work is to investigate photocatalytic performance of ferroelectric barium titanate in photodecolourisation of organic dyes and contribute to understanding of the photocatalysts with internal electric field. The main objectives are:

1. Study the photocatalytic activity of Ag decorated as-received $BaTiO_3$, including the effect of photodeposition time and pH of initial dye solution on photocatalytic efficiency, and detection of main reactive species during photodecolourisation.
2. Demonstrate the advantage of ferroelectric materials acting as photocatalysts in photodecolourisation dyes through direct comparison between as-received non-ferroelectric $BaTiO_3$ and annealed ferroelectric $BaTiO_3$.
3. Develop a deeper understanding on the mechanism and pathways of photodegradation of Rhodamine B with Ag decorated ferroelectric $BaTiO_3$.
4. Investigate the influence of ferroelectricity on the photocatalytic activity of heterostructured $BaTiO_3/\alpha\text{-}Fe_2O_3$.

1.3 Thesis structures

The thesis comprises 8 chapters and the respective summaries are:

Chapter 2 is the literature review. It covers the background of ferroelectric materials, the surface properties of ferroelectric materials, the mechanisms and state-of-the-art of semiconductor photocatalysis, and current application of ferroelectric materials as photocatalysts.

Chapter 3 presents the details of methods used in this work.

Chapter 4 investigates photodeposition of noble metal Ag on the as-received $BaTiO_3$, and studies the influence of photodeposition time and pH of dye solution on photodecolourisation rate. The main reactive species generated during photodecolourisation in this system were determined as well.

Chapter 5 probes into the effect of ferroelectricity of $BaTiO_3$ on its photocatalytic activity in decolourisation of RhB under solar light. Ag decoration on two types of $BaTiO_3$, as-received $BaTiO_3$ and annealed $BaTiO_3$ were carried out and comparison between them was performed. The advantage of ferroelectricity in photocatalysis was discussed.

Chapter 6 provides a deeper understanding about mechanism and pathways in photodecolourisation of RhB with Ag decorated ferroelectric $BaTiO_3$. The structural changes of dye molecules and intermediates produced during the process were monitored and determined.

Chapter 7 studies the photocatalytic activity of heterogeneous photocatalyst $BaTiO_3$/α-Fe_2O_3. Photocatalysts with different ratio of α-Fe_2O_3 were synthesised, and their activity in photodecolourisation of RhB were investigated. The improved photocatalytic activity was discussed from the point of influence of ferroelectricity.

Chapter 8 is a summary of conclusions and suggests the future research areas related to this work.

Chapter 2

Literature Review

2.1 Ferroelectric materials

Ferroelectric materials are characterised by a spontaneous polarisation that can be switched in orientation between two or more distinct crystallographic directions by applying an external electric field[16]. Ferroelectricity was first discovered in Rochelle salt in 1921. Later in mid-1940s it was extended to the perovskite-structure $BaTiO_3$ with the unusually high dielectric constant[24]. In addition to the most widely researched perovskite structured group, some other types of ceramics were also found to display ferroelectricity, including the tungsten-bronze group, the pyrochlore group and the bismuth layer-structure group[25].

2.1.1 Crystalline structure and definition of ferroelectrics

Understanding the crystalline structure symmetry is important for learning the origin of ferroelectricity. Among the 32 crystal classes which can describe all crystalline structures in nature, only 21 of them have no centrosymmetry. Of these 21 non-centrosymmetric groups, all except one possess direct polarisation when subjected to an external homogeneous stress along polar axis. The positive and negative ions in the unit cell will have a net displacement and electric dipoles will be generated, this is polarisation. The phenomenon of stress induced polarisation is piezoelectricity and non-centrosymmetric structure is essential for piezoelectric[24,25].

Out of the 20 piezoelectric groups, 10 are characterised as having only one unique polar axis, and electric polarisation exist in the absence of an applied field, named spontaneous polarisation. The spontaneous polarisation is temperature-dependent, and an alteration in temperature will induce a change in polarisation. This is called pyroelectric effect[24,25].

If the direction of spontaneous polarisation of some pyroelectric materials can be reversed under an external electric field, these pyroelectric materials are called ferroelectric materials. Thus ferroelectric materials belong to pyroeletric materials, but not all of pyroelectric materials present ferroelectricity, as reversibility of polarisation is necessary for ferroelectric materials. All the pyroelectric materials show piezoelectricity while only piezoelectric materials with spontaneous polarisation can be classified into pyroelectrics. Figure 2.1 shows the relationship between piezoelectric, pyroelectric and ferroelectric materials and their features[26].

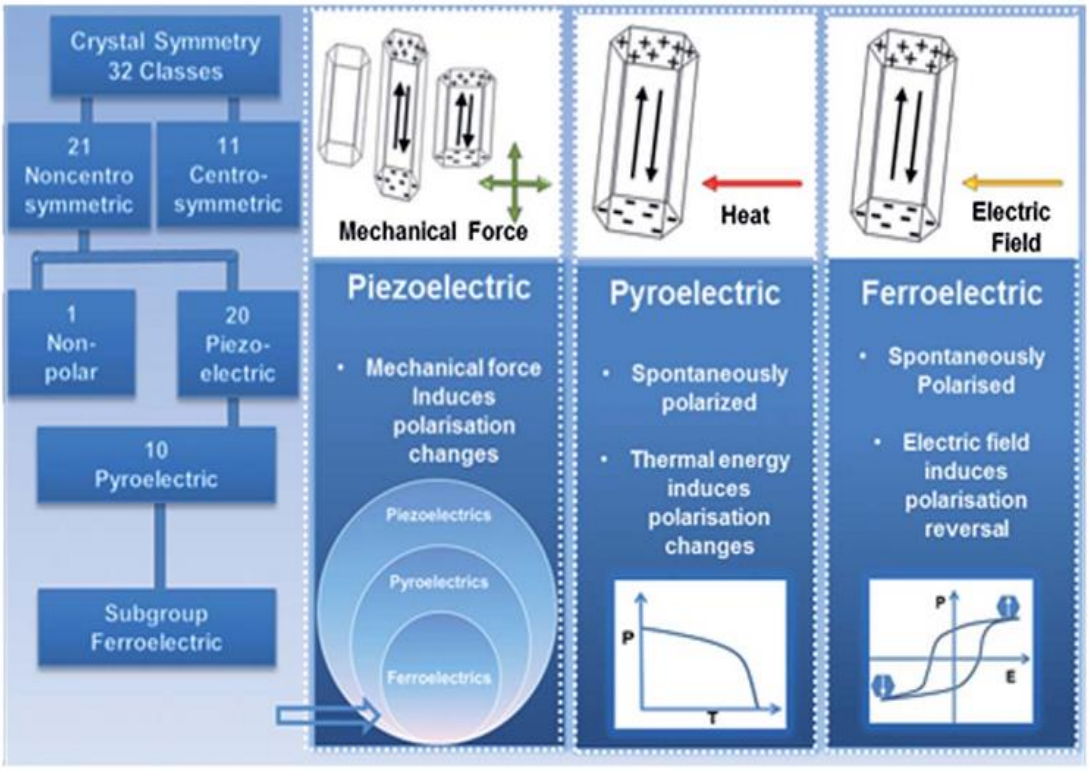

Figure 2.1 The relationshiop between piezoelectric, pyroelectric and ferroelectric. Adapted from Ref[26].

2.1.2 Spontaneous polarisation and screening

Reversible spontaneous polarisation stems from the displacement of positive and negative charge centre. Figure 2.2 shows schematically the spontaneous polarisation $\boldsymbol{P}_s$ in a typical perovskite structured ferroelectric, $Pb(Zr_xTi_{1-x})O_3$ (PZT)[27]. The perovskite structure is

widely adapted by many oxides with a chemical formula ABO_3, with larger A cations sitting in the corner of cube, smaller B cations in the centre of the cube and O anions in the middle of cube edge. Here in PZT, Pb ions are located in the corner and smaller Zr or Ti ions are sitting in the centre of the cube, as shown in Figure 2.2.

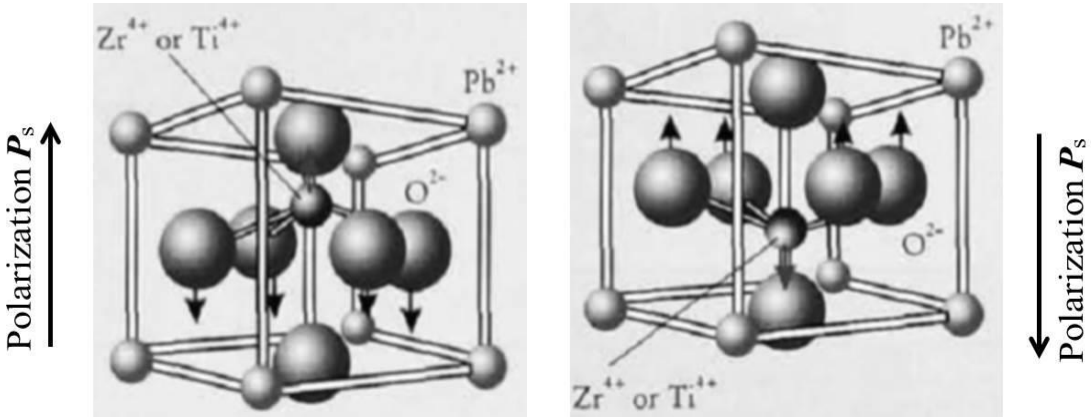

Figure 2.2 Perovskite structured $Pb(Zr_xTi_{1-x})O_3$ unit cell and the spontaneous polarisation Ps below Curie temperature, adapted from Ref [27]. Left shows an upwards polarisation while right shows a downwards polarisation, arising from varied-direction displacement.

Below the Curie temperature (T_c), body-centred Zr^{4+} or Ti^{4+} ions will have a displacement relative to the face-centred O^{2-}, resulting in the generation of electric dipole, i.e. polarisation. Different directions of the movement of charge centre will lead to a differently directed polarisation. It should be mentioned that displacement of the ions can also occur along **a** and **b** axis in addition to the **c** axis. Figure 2.2 only shows two of six possible polarisation directions. Spontaneous polarisation is defined by the value of the dipole moment per unit volume or by the value of the charge per unit area on the surface perpendicular to the axis of spontaneous polarisation[24].

Spontaneous polarisation will induce a polarisation bound charge on the surface and interface. The sign and magnitude of the charge depends on the orientation of the polarisation, structure and composition of the ferroelectric materials[28]. The presence of surface charge is not energetically stable and will be compensated in two ways, internal

screening and/or external screening. Internal screening normally takes the form of adsorption of free charge carries and defects with opposite sign in the materials whereas the external screening by the adsorption of opposite sign charged ions and molecules from the environment[17,29]. Figure 2.3 shows the surface charge and screening in a ferroelectric material.

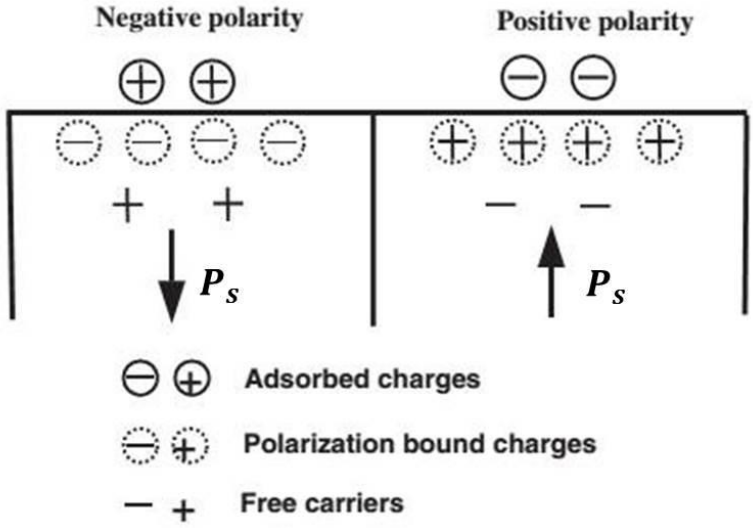

Figure 2.3 A schematic diagram showing polarisation bound charge and screening under different oriented polarisation conditions. Ps is the spontaneous polarisation. Adapted from Ref[17] .

2.1.3 Domain structure

The regions where the electric dipoles align uniformly in a ferroelectric crystal are named ferroelectric domains, and the interface separating domains are referred as domain walls. A ferroelectric crystal with one single domain is not thermodynamically favourable from an energetic view, as a strong depolarisation field will be generated. Thus the ferroelectric crystal prefers to split into multiple domains to achieve equilibrium between domain walls and the electrostatic self-energy [30], i.e. minimising the total relevant energies;

$$W_{tot} = W_M + W_E + W_{DW} + W_S = min, \quad (2.1)$$

Where W_M represents the strain related elastic energy, arising from the crystalline anisotropy and spontaneous polarisation; W_E is the electric energy from the depolarisation field; $W_{DW}$is the domain wall energy and $W_S$is the surface energy[29].

As shown in Figure 2.4, the domain walls are named by the angle between the adjacent polarisation vectors[31]. The formation of 180 ºdomain walls can reduce the electric energy W_E while the formation of non-180 ºdomain walls will release the elastic energyW_M. In a tetragonal ferroelectric crystal, this strain related non-180 ºdomain walls are 90 ºdomain walls whereas they are 71 ºand 109 ºdomain walls in rhombohedral crystal[25].

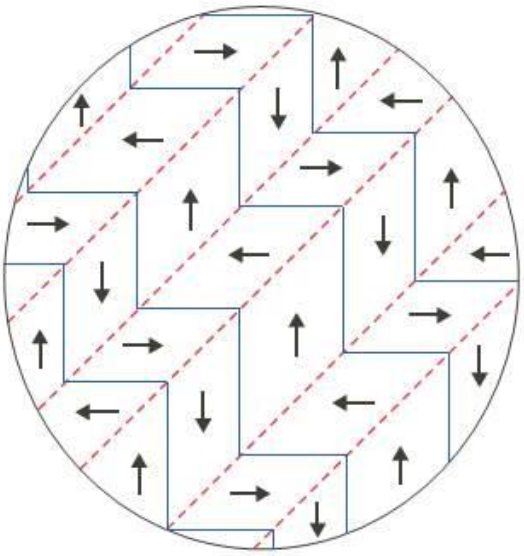

Figure 2.4 Domain structures in a tetragonal ferroelectric crystal. The dash lines are 90 ºdomain walls and the solid lines are 180 ºdomain walls. The arrows represent the directions of spontaneous polarisation in single domains. Adapted from Ref[31].

In multi-domain structured ferroelectric materials, the randomly oriented electric dipoles will cancel with each other and lead to a zero net polarisation, see Figure 2.5(a). When an appropriate external electric field is applied, the domain walls will move and the randomly oriented polarisation will align along with the direction of the electric field, which is named domain switching. Thus the net polarisation of the materials will be parallel to the direction of the applied electric field, see Figure 2.5(b). After removal of

the electric field, there will still be some domains remain the orientation, and result in the remnant polarisation, see Figure 2.5(c).

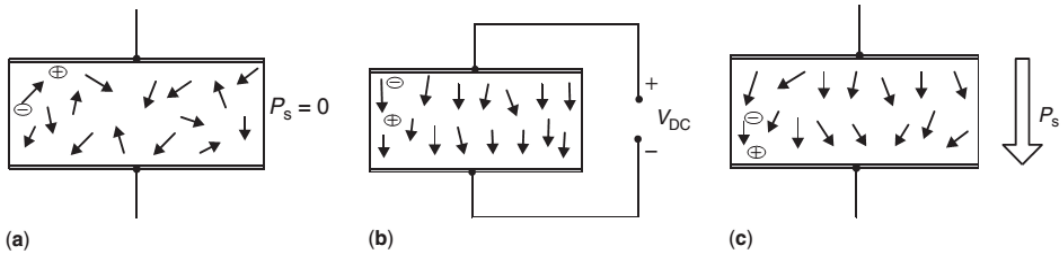

Figure 2.5 (a) randomly oriented domains, zero net polarisation; (b) domains align after external electric field applied, and (c) remnant polarisation remains even after removal of the electric field. Adapted from Ref[31].

2.1.4 Band bending, space charge layer and stern layer formation

In ferroelectrics, the internal screening by the free charge carriers and defect in the bulk will induce the free charge carrier concentration near the surface to be depleted compared with the bulk. This region is called space charge layer[32]. It can be accumulation layer or depletion layer, depending on the polarity of the surface charge. Meanwhile the energy band edges in this region will shift continuously and different from that in the bulk, which is named band bending. In the C+ domains (where the polarisation vector perpendicular to the surface and positive charged), electrons are accumulated for screening and give rise to a downward band bending, as shown in Figure 2.6 (top). On the other hand, in C- domains, where the surface charge is negative, holes are accumulated leading to an upward band bending[33], as shown in Figure 2.6 (down). The width of space charge region (L_d depletion layer, L_a accumulation layer) can be written as a function of surface potential V_s and Debye length L_D[34],

$$L_d = \sqrt[2]{\frac{2eV_s}{kT}} L_D \tag{2.2}$$

$$L_a = \sqrt{2}(1 - \exp\left[\frac{eV_S}{2kT}\right])L_D \tag{2.3}$$

where k is Boltzmann constant and T is the absolute temperature. It can be seen that the width of surface charge layer is proportional to surface potential V_s and Debye length L_D. The surface potential V_s depends not only the polarisation, but also the position of conduction band edge and adsorption layer on the solid surface. The Debye length L_D is a function of dielectric constant ε_r and donor concentration N_D[34],

$$L_D = \sqrt[2]{\left(\frac{\varepsilon_0 \varepsilon_r kT}{e^2 N_D}\right)} \tag{2.4}$$

where ε_0 represents the permittivity of free space. Base on Equation 2.2-2.4, it can be concluded that a higher charge carrier concentration N_D and a smaller dielectric constant ε_r will give rise to a shorter Debye length and then a narrower space charge region.

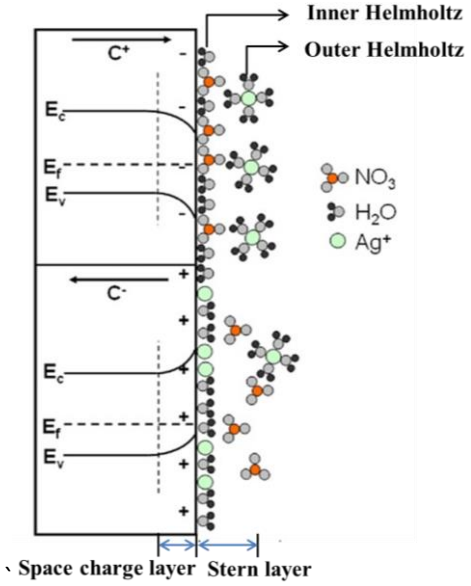

Figure 2.6 Band bending, space charge layer and Stern layer formation in C+ (top) and C- (down) domains in PZT with an external environment of $AgNO_3$ solution. Adapted from Ref[37].

The space charge layer and associated depolarisation field in this layer will impact the motion of photoexcited charge carrier in this region. In a positive-charged (C+) domain,

the electrons are driven to the surface while holes are driven to the other end. In a negative domain (C-), the situation will be inverse, holes moving to the surface and electrons to the bulk. This influence on the movement of electron-hole pairs will be reflected in the unique photochemistry properties of ferroelectric materials, which will be reviewed in detail in the next section 2.2.

The space charge region from internal screening in ferroelectric materials does not fully compensate the spontaneous dipole and the depolarisation field can penetrate into the wider environment[35]. This will result in external screening mechanism by adsorption of charged molecules or ions from the atmosphere, which will lead to the formation of Stern layer on the surface. This Stern layer is consisted of inner Helmholtz layer and outer Helmholtz layer[36], which is presented in Figure 2.6. The formation of Stern layer on the surface will influence the interactions between the charge carriers underneath the surface and the cations/anions in the external environment[37]. It is necessary to disturb the Stern layer for the charge carries below the surface to have reactions with external ions. As shown in Fig. 2.6, in order to reach C+ region and nucleate, Ag ions need to overcome the barriers of Stern layer. The disturbance of Stern layer usually takes place where there is a surface morphology variation, such as grain boundaries, where the surface potential is different from surrounding areas[37].

2.1.5 Size effect of ferroelectric materials

When the dimensions of ferroelectric materials are scaled down to nanometres, the dielectric properties will significantly deviate from the bulk and the size effect will arise. The size effect is a consequence of size-driven instability in polar phase, followed by the suppression of ferroelectricity below a critical size[38]. It has been reported that the spontaneous polarisation of $PbTiO_3$ nanoparticles decreases with the decreasing of particle size[38], as exhibited in Figure 2.7 (a). In addition, the size effect on ferroelectric

phase transition has also been observed in $PbTiO_3$, and the Curie temperature Tc of $PbTiO_3$ nanoparticles decreases as the particle size decreases when the particle size is below 50nm[39], as show in Figure 2.7 (b).

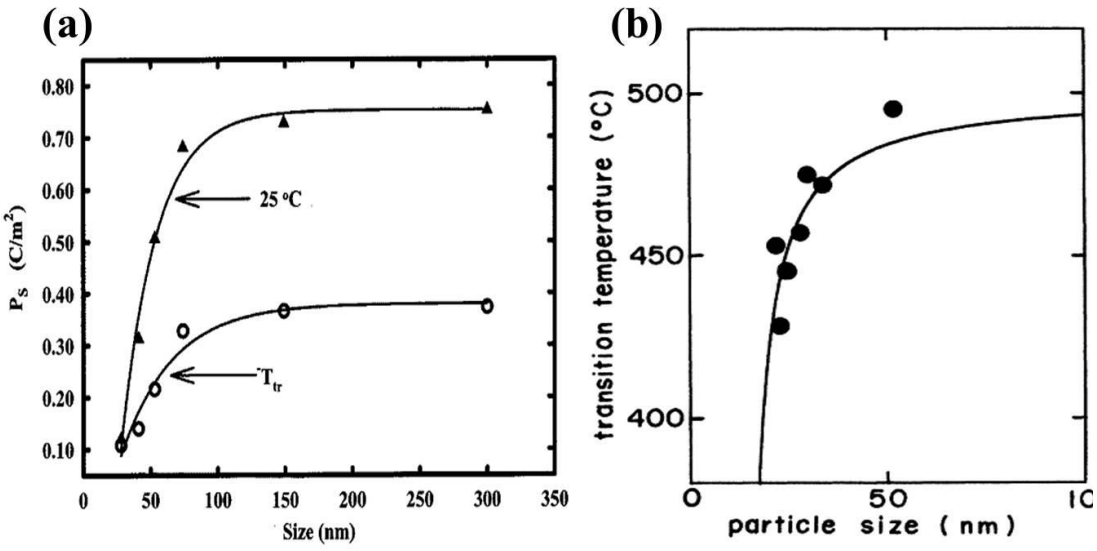

Figure 2.7 (a) The dependence of spontaneous polarisation in $PbTiO_3$ on particle size at room temperature and transition temperature (b) transition temperature of $PbTiO_3$ nanoparticles vs. particle size. (a) and (b) adapted from Ref[38] and Ref [39] respectively.

Furthermore, the same size effects were also reported in $BaTiO_3$[40,41]. It was found that the tetragonal distortion(c/a-1, c and a are the lattice parameter of the unit cell), Curie temperature T_c, heat of phase transformation and relative dielectric constant of dense $BaTiO_3$ ceramics were decreased along with the particle size decreasing from 1200 to 50 nm[40]. Uchino *et al.* proposed that the T_c dropped below room temperature at the critical size 120 nm for $BaTiO_3$ powder[42]. However, some other different values about the critical size of $BaTiO_3$ have been reported as well, e. g. 30 nm reported by Chang *et al*[43]. The discrepancies were considered to be related to the different sample processing and diverse characterization methodologies employed[43].

With respect for the origin of size effect of ferroelectricity, it is still not conclusive. However, it was accepted that the size effect can be intrinsic and extrinsic[44]. The intrinsic

factors are mainly related to the nature of ultrafine particles, including depolarisation field effects[45], the absence of long-range cooperative interaction [46]. When the particle size drops below certain critical size, the overwhelming depolarisation field which cannot be compensated completely in the nanoparticles will induce large free energy. This energy may exceed the energy reduction through ferroelectric phase transition, and thus the polar phases will not be thermodynamically stable[46]. The other factor is the absence of driving force for ferroelectric phase transition. The long-range interactions between the polar units support the development of a homogeneous spontaneous polarisation. However, the interactions are confined by some correlation lengths. When the crystalline size drops into this length range, one can expect some significant changes on phase stability.

In addition to the intrinsic effect, the extrinsic factors due to the modification of the microstructures or defects arising from processing also play an important role in size effect of ferroelectric materials[47]. For example, hydroxyl ions commonly exist as defects in the lattice of $BaTiO_3$ and the existence of these defects may upset the long-range polar ordering which drives the ferroelectric phase transition[46]. Therefore the existence of impurities may inhibit the formation of ferroelectric phase. Overall, due to the size effect of ferroelectrics, it needs to be carefully considered when designing the size of ferroelectric materials.

2.2 Polarisation-dependent surface properties of ferroelectric materials

The spontaneous polarisation, associated surface charge, band bending, and external/internal screening effects, all these elements combine and give rise to some particular surface properties of ferroelectric materials. Here the polarisation-dependent surface properties will be reviewed from three aspects, the interactions between metal ions/ charged particles and the ferroelectric surface, the interactions between the organic species and poled surface and some other intriguing surface properties.

2.2.1 Interactions between metal ions/charged nanoparticles and poled surface

As discussed, the space charge layer and the depolarisation field will drive the electrons and holes to separate and move in opposite directions. Therefore, it can be expected that the charge carries participated reactions, reduction for electrons and oxidation for holes, will proceed spatially separated as well. Rohrer *et al*. demonstrated this phenomenon in $BaTiO_3$[18,19]. It was found that when $BaTiO_3$ was exposed under super-band-gap irradiation, Ag^+ was preferentially reduced on the positive charged domain(C+) while Pb^{2+} was preferentially oxidized on the negative charged domain(C-) though the following reactions[19],

$$Ag^+ + e^- = Ag \tag{2.5}$$

$$Pb^{2+} + 2H_2O + 2h^+ = PbO_2 \tag{2.6}$$

The reaction-produced insoluble production allows researchers to observe the location of redox reactions, as shown in Figure 2.8. The location of Ag and C+ domain shows a one-to-one correspondence relationship. On the other hand, PbO_2 and C- domain presents this relationship as well. It should be noted that in Figure 2.8 (a), the straight line represents 90 ºdomain boundaries and 180 ºdomain boundaries, which are usually along curved lines on {001}surface, are not apparent in the unreacted samples.

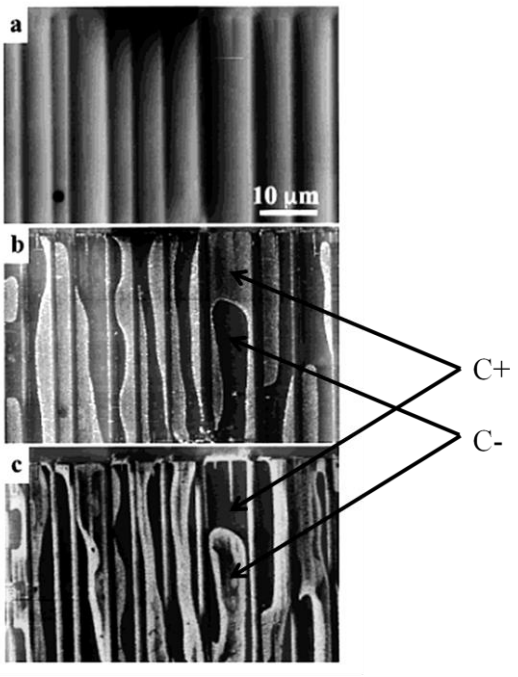

Figure 2.8 Topographic AFM images of the {001} surface of a $BaTiO_3$ single crystal. (a) Before the reactions. (b) After UV irradiation in the presence of $AgNO_3$ solution. The white contrast represents deposited Ag. It can be seen that Ag is preferentially located at C+ domains. (c) After the surface was cleaned and UV irradiation in the presence of lead acetate solution. The white contrast corresponds to PbO_2, which is preferentially located at C- domains. Adapted from Ref[19].

The selectively deposition of Ag nanoparticles on C+ domain were unlikely related to the adsorption of Ag ions before the reactions, because the positive surface charge will repel Ag ions with the same positive charge sign[18]. It was explained that in C+ domains, the static electric field will cause the electrons to flow to the surface where they can reduce Ag ions to metallic Ag nanoparticles. In C- domains, the holes will be driven to the surface and then oxidize Pb ions to PbO_2. These finding demonstrated that it is possible to use the electric field in ferroelectrics to separate photogenerated charge carriers by macroscopic distances and reduction and oxidation reactions can happened in distinct areas of the surface[19].

In addition to $BaTiO_3$, the same spatially separation of redox reactions were also observed in other ferroelectric materials, PZT [33,37,48–51], $LiNbO_3$[52–57], and $BiFeO_3$[58]. By

adjusting illumination with different intensities, it was observed that Ag nanoparticles can be deposited on C- domain in PZT[48], which was regarded as non-preferential position in the former report. This phenomenon was explained to be related to the change of band structure and width of space charge layer arising from excitation of electrons. The narrowing of space charge layer region allows electrons to tunnel through and have reactions with Ag ions. Due to the existence of this barrier, the rate of Ag nanoparticle grow on C- domain was about half of that on C+ domain[48].

Moreover, through a series of further investigation on metal salt reduction on PZT, it was found that many factors can have an impact on the metal particles size, deposition rate and location, e.g. different magnitude of remnant polarisation on different crystalline orientations[50], surface defects[51]. It was found that in negative domains, the possibility of electron tunnelling through space charge and electron reduction Ag ions was about 10^{19} smaller in a [111] orientation than in [100][50]. As shown in Figure 2.9, the width of space charge layer in [111] orientation is larger than [100], which is due to a stronger remnant polarisation in [111] orientation. The small change in the width of space charge region will significantly affect the availability of free charge carriers on the surface. Here, the electron-depletion layer in Figure 2.9 acts as a barrier for the electrons to arrive on the surface, and thus a thinner layer means an easier tunnelling through for electrons.

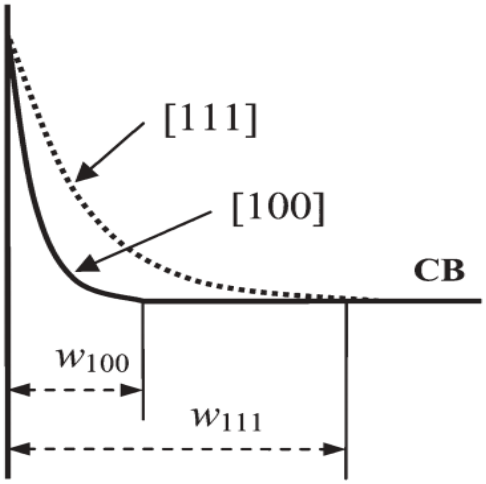

Figure 2.9 The space charge layer of PZT in different crystalline orientations [100] and [111] in C-domain. Due to a smaller remnant polarisation in [100] direction, the width of space charge layer is narrower than in [111]. Adapted from Ref [50].

The composition variances in PZT will also affect the photo-induced Ag reduction on the surface because different compositions will possess different spontaneous polarisations, and then different shape and width of space charge layer[49]. In addition to the polarisation state of the materials, surface defects such as grain boundaries will also affect the metal salt reduction. The Ag particles deposition rate was much larger at grain boundaries and line defect than the native domain region[51]. This was related to the band bending at grain boundaries arising from the atomic mismatch, as shown in Figure 2.10. More photo-excited electrons will flow to the grain boundaries, and more electrons are available for reactions. It was calculated that the free electrons available at grain boundaries were approximately 40 times that in positive domains[51].

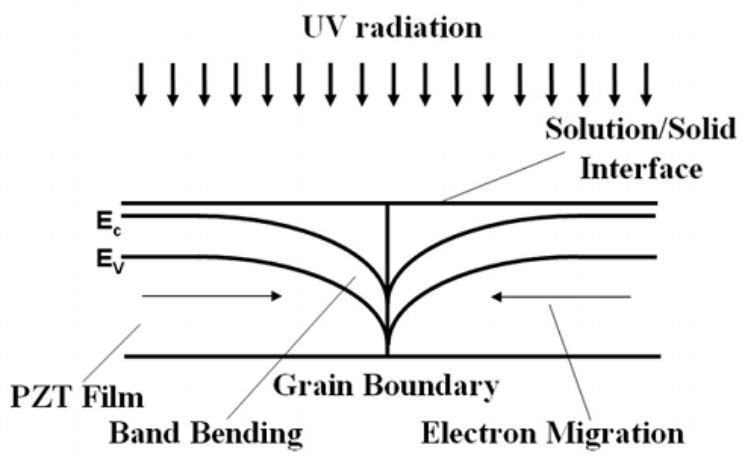

Figure 2.10 Schematic of band bending in the grain boundary in PZT film. Adapted from Ref[51].

Being different from PZT, which possess a large number of defects, $LiNbO_3$ is characterised by a low concentration of defects and high spontaneous polarisation[57]. Therefore, the studies on the polarisation-dependent surface phenomenon show some different explanations from that in PZT. It was observed as well that the metal nanoparticles deposition on C- domains in $LiNbO_3$[53,54,57]. However, due to the low defects density and high spontaneous polarisation, the space charge layer is large and then it will not be expected that the narrowing space charge layer by using higher intensity irradiation in the case of PZT[57]. Instead, the mechanism named photoelectric effect was proposed to account for this, where the electrons are excited to the vacuum level[57], as shown in Figure 2.11. In addition, it was concluded that the photovoltaic effect in $LiNbO_3$ accounted for the metallic nanoparticle deposition on the C+ domain, considering a weak local electric field and resultant inefficiently movement of electrons to the surface in C+ domain[52].

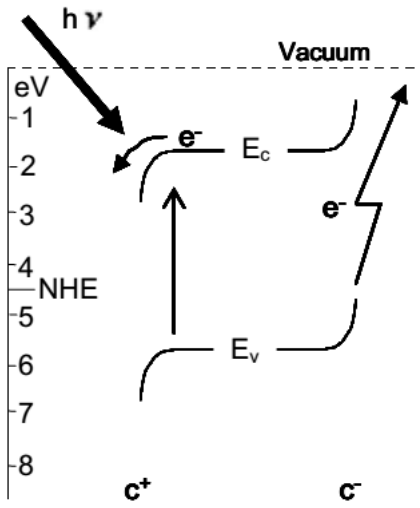

Figure 2.11 Photoreduction on C+ domain and photoelectric reduction on C- domain in LiNbO3. In photoelectric reduction, incident photon energy excite electrons to vacuum level whereas photoexciation below vacuum level in photoreduction. Adapted from Ref [57].

In addition to these intrinsic factors impacting the photoreduction of metal nanoparticles on the surface, exterior factors can also influence the deposition of metallic nanoparticles, e.g. incident energy. It was found there was a strong relationship between the incident photon energy and resultant Ag nanoparticle size. As the photon energy increased, more electrons will be excited from deeper density of states, and more electrons available for the reduction reactions. Thus a greater reduction rate and a larger area covered by the metallic Ag nanoparticles was obtained[37]. Sun *et al*. investigated the effect of irradiation wavelength, metal salt concentration and intensity on the photo-induced Ag nanoparticles deposition on $LiNbO_3$[54,55]. It was concluded that shorter wavelength will result in more charge carriers diffusion over field assist migration and then the selectivity deposition on domain boundaries will be obscure[54]. By tuning the Ag ion flux and photon flux ratio, Ag nanoparticle deposition can be controlled to be boundary-enhanced or boundary-depressed[55], as shown in Figure 2.12.

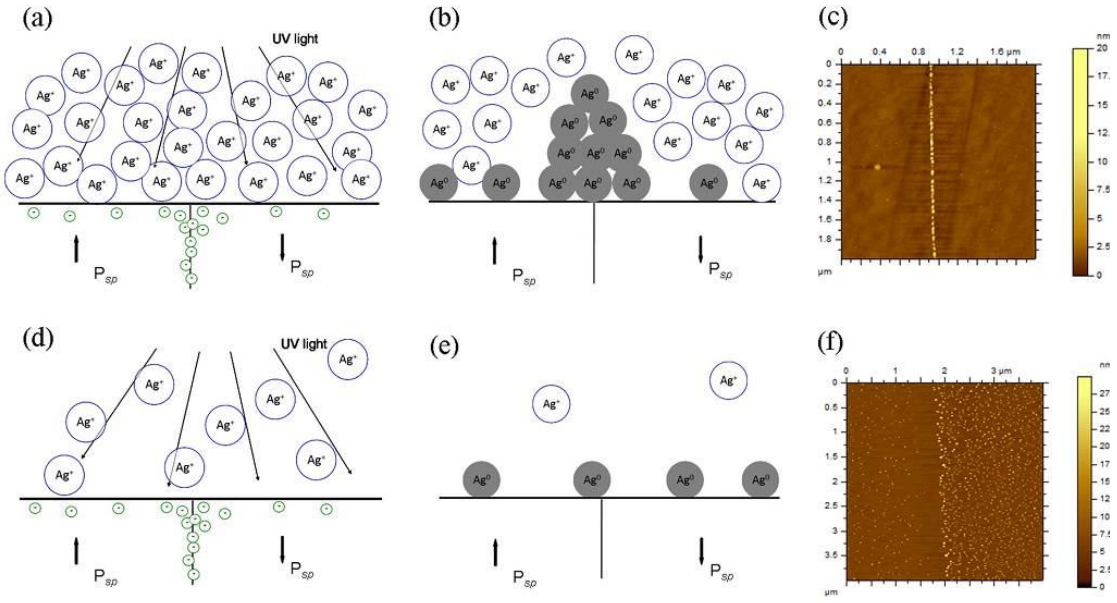

Figure 2.12 Schematic for the deposition of Ag nanoparticles with different Ag ion flux and photon flux ratios. (a) Ag+ flux is six orders of magnitude greater than photon flux. For each electron on the surface, there is an Ag ion available to be reduced. (b-c) the the resulting Ag^0 location and corresponding AFM image, showing the distribution reflects the electron distribution. Domain boundaries will be selectively decorated. (d) Ag^+ flux is four orders of magnitude greater than photon flux. Not every electron can have an available Ag ion. But for Ag ions, there will be plenty supply of electrons. (e-f) the resulting Ag^0 location and corresponding AFM image, showing the distribution reflects the Ag ion distribution. Ag nanoparticle will uniformly deposit. Adapted from Ref[55]

The impact of spontaneous polarisation of the underlying ferroelectric substrate is not only limited to the metal nanoparticles deposition, but also reflected in the terms of charged particles distribution. In contrast to the metal salt reduction on ferroelectric reviewed above, the charged particles selectively deposition normally relate to electrostatic attractions rather than redox reactions.

It was found that negatively charged polystyrene (PS) microspheres selectively deposited on the positive domain of $LiNbO_3$ at room temperature, which was due to the electrostatic interactions between the charged particles and the polarisation surface charges[59]. Under UV illumination, the stable balance between internal screening and external screening

will be disturbed, and internal screening will increase due to photo-excited charge carriers while adsorbed charge from external screening will reduce. When illumination was switched off, there is no more continuous electron supply and incomplete screening (polarisation surface charge σ_{pol} is larger than screening charge σ_{scr}) will occur. Therefore, the negatively charged PS particles will move to the C+ domain to compensate the excess surface charge. Interestingly, when the deposition process was carried out under elevated temperature, PS particles will preferentially distribute on the C- domain, which is opposite to the result observed at room temperature. This is arising from the pyroelectric effect of $LiNbO_3$. Heating of $LiNbO_3$ will result in the decrease of spontaneous polarisation and overscreening ($\sigma_{pol}<\sigma_{scr}$). Thus the excess positive screening charge on negative domain will attract negative charged PS particles.

The selective distribution of charged particles was also observed in the absence of any illumination. Positively charged tobacco mosaic virus (TMV) particles were demonstrated to preferentially deposit on positive domain and the negative domain effectively repelled the virus particles in PZT[35]. This was ascribed to the formation of an opposite charged Stern layer over PZT surface due to external screening. Positive domain will be surrounded by negatively charged ions while negative domain covered by positively charged ions. Thus the electrostatic attractions will explain the virus particles selectively location on positive domain.

The spatial separation of electron and holes was not only limited in bare ferroelectric materials, but also in the non-ferroelectric thin films on ferroelectric substrate[60–63]. It was found that the photogenerated charge carriers in $BaTiO_3$ substrate can transfer through the TiO_2 thin film and participate in the redox reactions, as indicated in Figure 2.13. This explained the same pattern of reaction products as the underlying ferroelectric domain

pattern. The influence of polarisation on the pattern on the thin film diminished with the increasing thickness of the film. These observations imply the influence of polarisation can be extended into the composite structures.

The spontaneous-polarisation-dependent spatial separation of electron-hole pair in ferroelectric materials provides a new routine to direct chemical reactions and assemble complex nanostructure[21]. Ferroelectric lithography was proposed based on this method [64,65]. Through manipulating domains at small scale by contact electrode patterning, scanning probe patterning or electron beam patterning, multiple nanostructures of different materials, ranging from metal nanoparticles to organic molecules, can be assembled to the pre-defined positions. Ferroelectric lithography opens a new avenue in the potential application in molecular electro-optic transducers, information storage devices, integrated biochemical sensors, and wireless communication components[64].

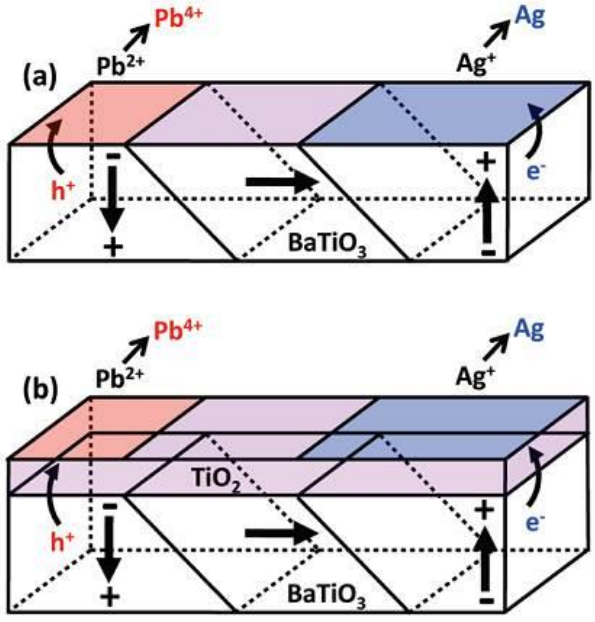

Figure 2.13 Schematic showing the influence of polarisation on the movement of charge carriers. (a) bare ferroelectric $BaTiO_3$ (b) thin TiO_2 film on ferroelectric $BaTiO_3$. Adapted from Ref[61].

As a summary, the spontaneous polarisation in ferroelectric materials influences the selectively location of photodeposited metallic nanaoparticles and other charged particles.

The opposed sign of surface charge on C+ and C- domains, the spatially separation of charge carriers, the associated space charge layer and band bending combine and account for these interesting surface phenomena.

2.2.2 Interactions between molecules and poled surface

Spontaneous polarisation also influences the adsorption and interactions of molecules on the surface, e. g. water, carbon dioxide and other organic species. A dipole-dipole interaction mechanism was tentatively proposed based on the investigation of adsorption of CO_2 on $BaTiO_3$[23]and $LiNbO_3$[22] powder particles. It has been claimed that a dipole between C and O atoms will be induced when CO_2 was adsorbed on $BaTiO_3$ with C atoms near the surface and O atoms stand up. The induced dipole in CO_2 interacts with the dipole in the ferroelectrics, and this mechanism was expected to be competitive in adsorption strength with adsorption through charge transfer mechanism[22]. Following these work, a series of further studies on the surface adsorption on ferroelectric thin film or single crystal were reported[66–72].

In the investigation of adsorption of 2-propanal on the poled $LiNbO_3$ (0001) surface, it was found that the desorption peak temperature on positive surface was over 100K higher than on negative surface, suggesting 2-propanal adsorbed more strongly on positive surface. Furthermore, the desorption activation energies on C+ and C- were calculated. As shown in Figure 2.14, the desorption activation energy can be calculated from the slop of the fitted line, and it was 73 kJ/mol on positive surface and 62 kJ/mol on the negative surface at 200K[66]. A higher desorption activation energy on positive surface was concluded. Furthermore, it has been demonstrated that the adsorption sensitivity to the poling directions only limited to polar molecule, 2-propanal and acetic acid, and the adsorption of nonpolar dodecane was independent to the poling directions[67] by comparing their adsorption/desorption on $LiNbO_3$(0001). The adsorption difference between polar

and nonpolar molecules indicated that interactions between polar molecules and dipoles in ferroelectric were dominated by electrostatic interactions.

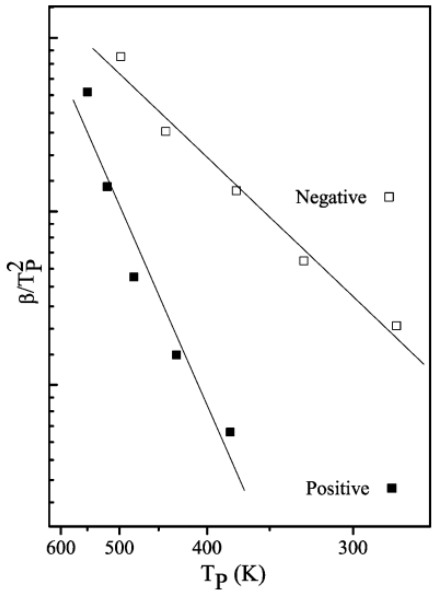

Figure 2.14 Log scale plot of β/Tp^2 versus Tp. β represents heating rate and Tp represents temperature of desorption peak. A steeper slope indicates a higher desorption activation energy on positive surface. Adapted from Ref[66].

Contrary to the work reviewed above where the positive and negative surface were obtained by poling separately, Bonnell *et al.* used an *in situ* method to pole the surface and investigate the physisorption of CH_3OH and CO_2 on $BaTiO_3$(001) and PZT thin film[68]. The advantage of this method is to keep the polarisation direction as the only varied parameter. The temperature programmed desorption (TPD) results, as shown in Figure 2.15, illustrated that the amount of adsorption increased following the order: C+< unpoled< C-. The integrated TPD peak area reflected that the reactive sticking coefficient and physisorption energy were polarisation dependent whereas the similar TPD peak shape indicated that the chemisorption energy was not. Furthermore, the authors proposed the adsorption of molecules onto ferroelectric oxide followed a precursor-mediated adsorption mechanism, which is schematically shown in Figure 2.16. A state of weakly

trapped in a shallow physisorption well is the precursor of chemisorption state, which is formed after overcoming a higher activation energy barrier. The physisorption energy reflects the time resident of molecules on the surface, which will determine the possibility of the precursor state encountering with defects and chemisorbed. This work provides the first definite evidence of polarisation- dependent physisorption energy[68].

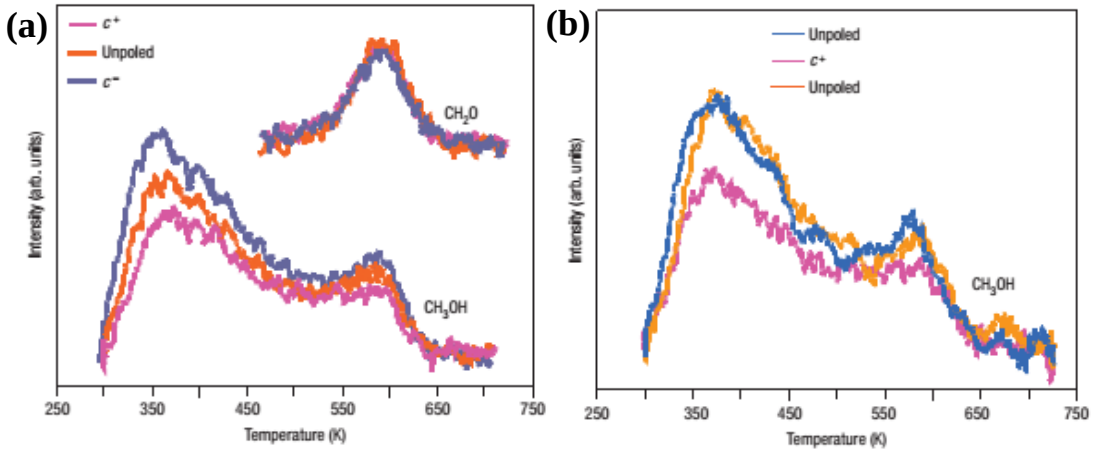

Figure 2.15 Temperature programmed desorption spectra of different-orientation-poled $BaTiO_3$ thin film surface after exposure to 20L dose of methanol. (a) desorption peaks of CH_3OH and CH_2O, poling order: C+, unpoled, C-;(b) desorption peak of CH_3OH, poling order : unpoled, C+, unpoled. Adapted from Ref[68].

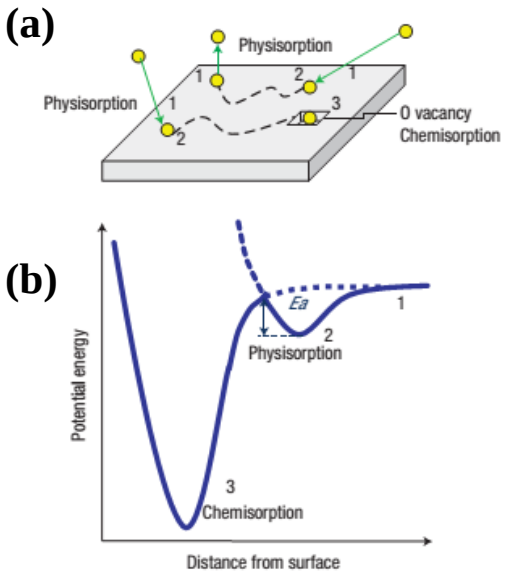

Figure 2.16 Schematic of precursor-mediated adsorption mechanism on ferroelectric oxide surface with defect on the surface. (a) physically adsorbed molecules can diffuse on the surface and desorb eventually, or encounter with an reactive site, e.g. oxygen vacancy , to result in chemisorption. (b) the accordingly potential energy as a function of distance from surface. Adapted from Ref[68].

Following this work, the study of adsorption of alcohols on ferroelectric surface was expanded to ethanol[69] and 2-fluoroethanol[70]. C_2H_5OH was found to adsorb most on positive surface[69] of $BaTiO_3$ thin film, which was different from CH_3OH which was observed to be adsorbed more on negative surface[68]. This discrepancy was related to different polarity of methanol and ethanol. A molecule with a stronger polarity will have interactions with surface more strongly. Moreover, it was demonstrated that the polarisation can also impact the activation energy of surface catalysed reactions[70]. 2-fluoroethanol was dissociatively adsorbed on $BaTiO_3$ thin films and fluoroethoxide intermediates were observed as intermediates. The temperature at which acetaldehyde was produced was polarisation sensitive, and the activation energy for this reaction was 4 kJ mol^{-1} higher on positive surface than on negative surface. This observation suggests a potential application of ferroelectric materials in adjusting pathways of surface reactions by manipulating the surface polarisation.

Inoue *et al*. reported that Pd deposited on ferroelectric $LiNbO_3$ single crystals presented different activation energy of CO oxidation between positive surface and negative surface[73]. The activation energy on positive surface was 126 kJ/mol when the thickess of Pd thin film was 0.2nm and decreased to 96 kJ/mol when thickness was 0.02nm, while it was 128 kJ/mol on negative surface no matter the thickness. The phenomenon was ascribed to the depolarisation effect through electron transfer from Pd to positive surface, altering the energy state of Pd thin films and weakening the CO adsorption bond. When the Pd thin films are thick enough, the thin film will behaviour like bulk metal, and the electron transfer will not effect of the energy state. This observation demonstrated that the polarisation effect can penetrate the thin films on top, and impact the surface properties of the thin film.

2.2.3 Other polarisation-dependent surface properties

Apart from the reviewed interactions between the metal ions/ charged particles, small molecules and ferroelectric surfaces, there are some other polarisation-dependent physical and chemical phenomena. It was reported that $BaTO_3$ crystals exhibited surface conduction which is sensitive to the polarisation direction and non-conduction along the directions of perpendicular to the surface[74]. As shown in Figure 2.17, the current-voltage line indicated an Ohmic relationship on positive surface, and the conductance was about 10 times higher than the negative poled surface and random-oriented surface. This conductance was due to the existence of charge carrier layer on the surface arising from polarisation, and on the positive surface it is the electron accumulation layer.

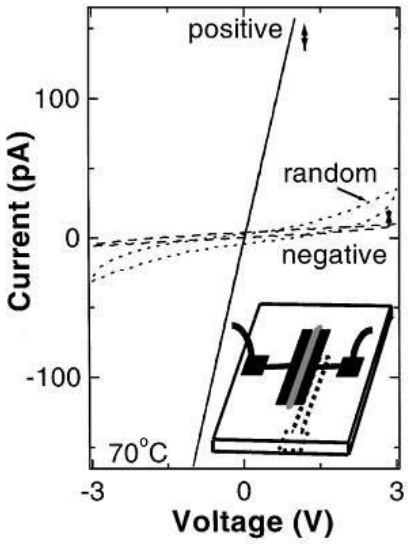

Figure 2.17 Current-Voltage (I-V) curves of $BaTiO_3$ single crystal with different polarisation directions. Inset schematically shows the measurement setup. Two metal electrodes are deposited on the top and bottom of the crystal and the gap area are poled. Adapted from Ref [74].

The variation of surface electrical conductivity was observed in the NiO thin films on $LiNbO_3$ as well[75]. It was found that the surface electrical conductivity of NiO on positive suface was considerably higher than that of negative surface. It was proposed that the ferroelectric $LiNbO_3$ susbtrate altered the charge carrier disctribution of NiO. The polarisation of positive surface will give rise to hole accumulation on the NiO surface. As for p-type semiconductor NiO, the major charge carrier is positive hole and thus hole accumulation will result in a higher electrical conductivity. On the other hand, NiO on the negative surface will show a reverse condition, hole depletion on the surface and a low electrical conductivity.

Based on the images of periodically poled $LiNbO_3$ obtained by UV-photoelectron emssion microscopy, it was found that a higher photoelectric field generated from negative domain, indicating a lower threshold (~4.6 eV) of negative domain compared with that of positive domain(~6.2 eV)[76]. This discrepancy was ascribed to the varitation of surface electron affinity due to the different surface dipole indued by surface adsorbates.

The schematic plot of band structures of positive and negative domains and the associated surface electron affitinity χ_s, photothreshold E_{th},electron affinity varitation $\Delta\chi$ was shown in Figure 2.18. In the positive domains, the positive surface charge will be screened by the negative-charged adsorbated, which will induce electron affinity to increase. Then accordingly the photothreshold will increase.

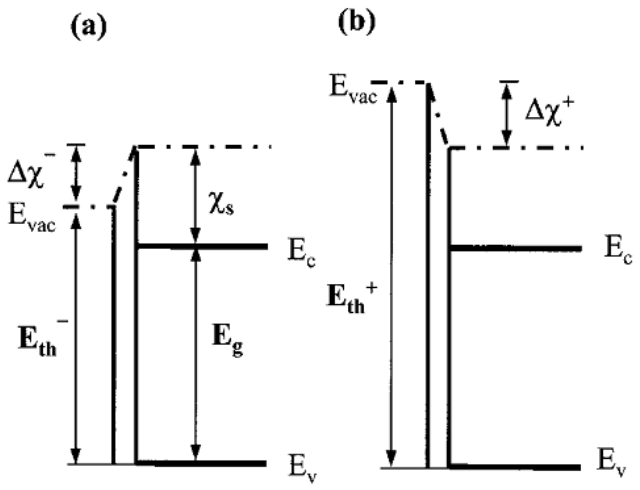

Figure 2.18 Energy band structures of adsorbate-covered (a) negative domain and (b) positive domain. χs, Eth, Δχ and Eg represent surface electron affinity, photothreshold, variation of electron affinity due to adsorbate and band gap respectively. Adapted from Reference [76].

In addition, the different etching rate on positive and negative domains in acid solutions were observed in $BaTiO_3$[77] and $LiNbO_3$ single crystals[78,79]. The authors related this phenomenon to an rate-deterimining protonation step, which is discrepant on domains with opposite surface charges[79].

Overall, the polarisation in ferroelectrics and associated properties, e.g. internal/external screening, band bending, dipolarisation field, combine to contribute to the above reviewed polariation-dependent adsorption and interaction phenomena and some other particular surface properties. The contributions from these factors depend on both interior properties of ferroelectric materials, e.g. band gap, magnitude of polarisation, defect density, and exterior enviroment, e.g. intensity of illumination, thermal effect, sample

processings. The polarisarion-dependent surface properties of ferroelectric materials provide some new directions in the applications of ferroelectric in ferroelectric nanolithography, chemical sensors based on swtiching the polairsation directions[80], etc. Furthermore, it can be expected these intriguing polarisarion-dependent surface paroperties can impact on the photocatalytic performance, which will be disscussed below.

2.3 Semiconductor photocatalysis

The conflict between the substantially increasing of energy demand and the gradually shortage of traditional fuel is becoming more and more serious challenge. Furthermore, the globally environmental deterioration arising from the excessively rely on traditional fuel, e.g. greenhouse gas from combustion of coals and fossil oil, accelerates the calling for a renewable and enviromental-friendly energy. Since Fujishima and Honda discovered water photolysis using TiO_2 as photoanode and Pt as photocathode in 1972[81], semidonductor photocatalysis has received extensive attention and research in past decades. It has been demonstrated to be potentially applied in hydrogen generation from water splitting[13,82,83], organic fuel synthesis from photoreduction of carbon dioxide[84–86], water and indoor air purification[6,8,87–89]. Semiconductor photocatalysis provides new avenues to utilize the expansively available natural sunlight to produce green solar fuel and remediate environmental issues.

2.3.1 Mechanisms of semiconductor photocatalysis

Under super-band gap illumination, semiconductors will absorb photons, and electrons will be excited from valence band (VB) to conduction band (CB), leaving equal-number holes in valence band. Then the generate electons and holes will migrate to the surface,during which process a large portion of electron-hole pairs will recombine and dissipate the input energy in the form of heat or emitted light. The electron and holes transferred to the surface can participate the reduction and oxidation reactions with the

adsorbates on the semiconductor surface respectively[9]. The basic mechanisms of semiconductor photocatalysis were schematically shown in Figure 2.19.

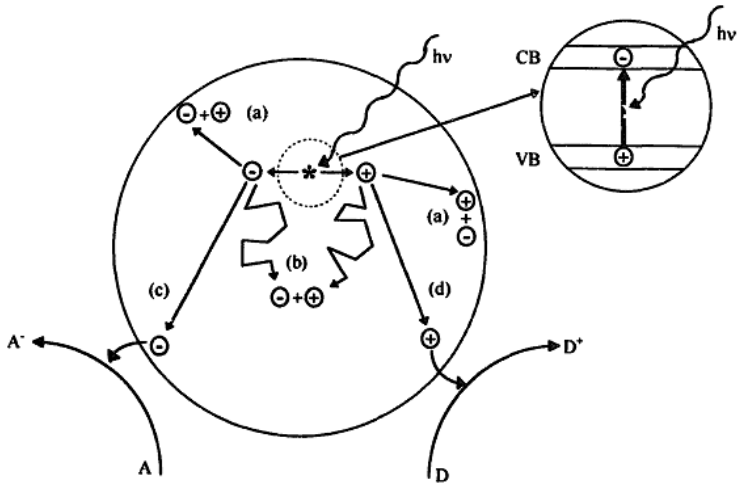

Figure 2.19 Schematic of semiconductor photocatalysis. Recombination of electron-hole pairs can happen both in surface (a) and bulk (b). (c) and (d) represent reduction and oxidation reactions involving photogenerated electrons and holes respectively. Adapted from Ref[9].

2.3.2 Main factors affecting photocatalytic efficiency

Depending on the specific application of semiconductor photocatalysis, there are a range of different aspects influencing the overall efficiency. Taking photodegradation of organic polluctants in waste water as an example, it was stated that the amount of catalyst, wavelength of illumination, initial concentration of target organic compound, temperature and radiant flux, all these paramenters combine and impact on the kinetics of reactions[8,90]. In addition to these physcial parameters, the inherent properties of photocatalysts also contribute to the efficiency, which are more attractive for material scientists.

2.3.2.1 Intrinsic factors

The inherent properties of photocatalysts which affect photocatalytic activity can be grouped into intrinsic and extrinsic factors. The intrinsic factors are mainly related to the basic mechanisims of semiconductor photocatalyst while the extrinsic factors mainly relate to the morphogies, size, defects of photocatalysts, etc.

There are mainly three intrinsic elements affecting the activity from the view of the primary steps in semiconductor photocatalysis. The first one is the band-gap configuation of photocatalysts, which determines the absorption of photons, photoexcited of photocatalysts and the redox capability of photoexcited charge carriers.The band gap of photocatalysts should be appropriate narrow so that it can absorb the majority of solar spectrum –visible light. Meanwhile, the band-gap positions of semiconductor should overlap the according electrochemical potentials of the redox reactions which are expected to proceed. The valence-band edge is required to be more positive than electrochemical potential of the oxidation reactions while the conduction-band edge needs to be more negative than the reduction reactions. Figure 2.20 shows band-gap positions of some common semiconductors and energy levels of some redox reactions in water. Therefore, band-gap configuation influences the generation of photoexcited electron-hole pairs and the redox potentials of these charge carriers, which impact the overall photocatalytic efficiency.

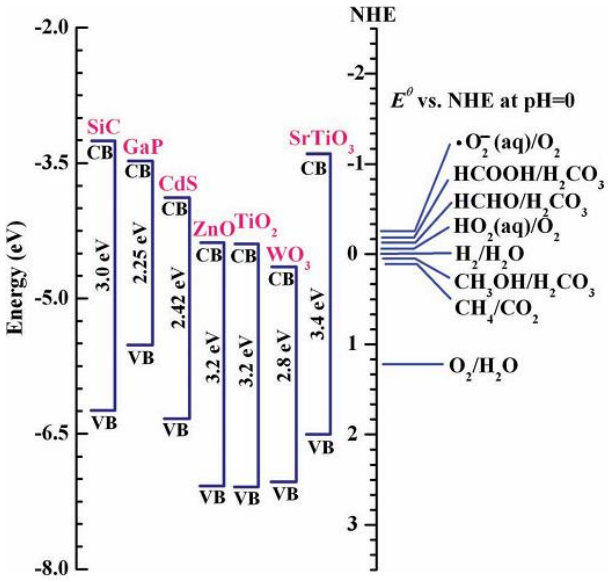

Figure 2.20 Band-gap positions of some semiconductor photocatalysts relative to energy level of some redox couples in water. Adapted from Ref[14].

The second intrisic issues limitting photocatalytic efficiency is electron-hole

recombination. After electrons and holes generated, they will encounter defects during the migration process to the surface, which will act as recombination centres. Electons and holes will recombine with each other, and photoenergy will dissipate in the form of heat or light, which is useless for photocatalysis. In addition to bulk recombination, recombination can happen on the surface as well. Bulk and surface recombination will reduce the chance for charge carriers to transfer to the surface and participate in the redox reactions successfully.

The third intrisic element is the possible back-reactions of intermediates during photocatalysis[11]. It is likely that the reaction products and intermediates have reactions and push back the photocatalytic reactions because the intermediates and products are held adjacently to each other. Take water splitting as an example, back reactions to form H_2O between H_2 and O_2 are easy to proceed because the water spitting is an uphill reaction[82].

2.3.2.2 Extinstic factors

Besides these three intrinsic factors, some extinstic elements also influence the efficiency. The extinstic factors mainly include the photocatalyst size and morphology, polymorphy form, crystallinity and defects, etc. [91].

The paticle size of photocatalysts is an important factor influencing the reaction rate. Smaller particle size gives rise to larger surface area, more reactive sites on the surface and a prompted reaction rate. Furthermore, smaller particle size means a shorter diffusion pathway for charge carriers to reach the surface. However, an ultra fine size of particles will increase the possibility of electron-hole recombination due to they are confined to proximity locations and offset the benefits of more reactive sites to some extent[92,93]. Thus a balance between the positive side of more reactive sites and negative side of increasing recombination should be considered when designing the size of efficient photocatalysts.

Apart from the size, the shape of photocatalytic materials also impact on the efficiency. Various architectures of nano-dimension photocatalysts have been widely developed, including nanorods, nanowires, nanobelts, nanosheets. These particular structures can facilitate charge carriers transport from bulk inside to the surface and/or guide the lateral charge carriers movement along axis directions[13,14]. It has also been reported that the different facets of single crystals present different photocatalytic activities due to a discrepancy in surface energy on different facets[94,95]. As shown in Figure 2.21, the catalysts with rhombic dodecahedron shape shows an enhanced photodegradation rate compared to cubic and sphere shapes. This was attributed to the exposed{110}facets in rhombic dodecahedron shape and {100}facets in cubic facets. The former facets possesss a higher suface energy(1.31 J/m^2) than the latter one(1.12 J/m^2), leading to a higher photocatalytic activity.

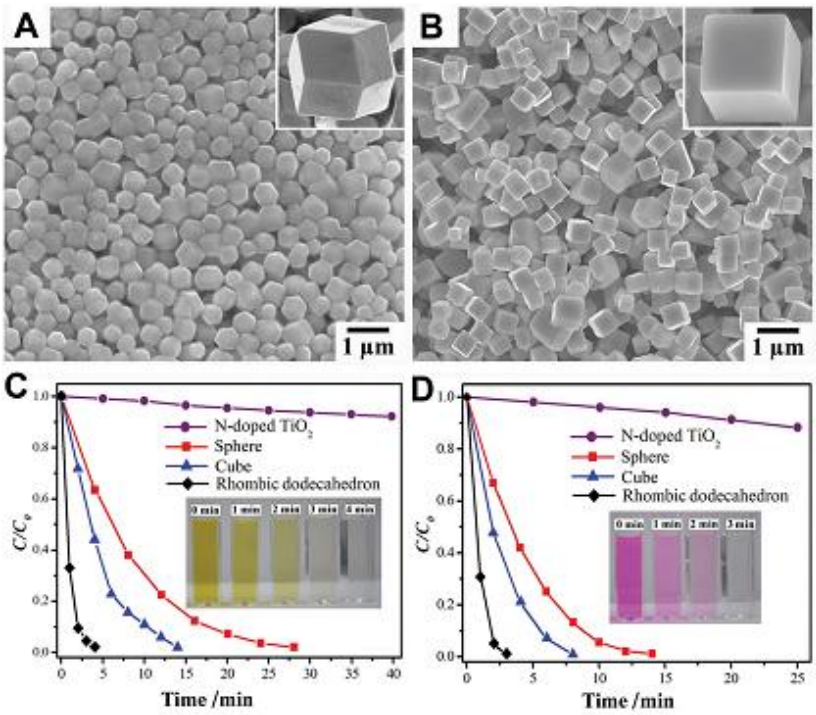

Figure 2.21 SEM images of Ag_3PO_4 sub-microcrystals with different morphologies (A) rhombic dodecahedrons (B) cubes.The degradation profiles of (C) Methyl Orange dye and (D) Rhodamine B dye under visible light with catalysts of different shapes. Adapted from Ref[94].

The crystallinity of the photocatalysts and associated defects concentration also play an important role in determining the efficiency. As described, defects can act as recombination centres. Therefore, photocatalysts with higher degreee of crystallinity and lower defects density will lead to a higher photocatalytic activity[82]. Generally, thermal treatment for a long period time will drive out the non-equilibrium defects, increase the degree of crystallinity and inhibit recombination. However, on the other side it will also induce the agglomeration of particles and a decrease in surface area, which will induce less reactive sites on the surface and deterioration of photoactivity. Therefore compromise between the high degree of crystallinity through thermal treatment and a risk of reduced surface area should be taken into account.

2.3.3 Strategies to improve photocatalytic efficiency

The factors reviewed above combine and limit the overall photocatalytic efficiency, hindering the industrial applications of semiconductor photocatalysis. Thus how to improve the photocatalytic performance and enhance the activity of photocatalysts has been a hot spot in the research field of semiconductor photocatalysis. Various methods to overcome the efficiency limitation have been developed, mainly include ion doping, heterogenous combination, and morphology control.

Ion doping have been widely adopted to improve the photocatalytic acitvity, and both metal and non-metal ions have been investigated. Doping with metal ions (mainly transitional metals) will induce an impurity energy levels in the forbidden band, make the wide band gap narrower, and get photocatalysts more active in visible-light region[13]. Depending on the dopant, it can provide an donor level above the valence band or an acceptor level below the conduction band, as shown in Figure 2.22. The role of metal-ion doping in altering band gap and improving visible-light absorption can be demonstrated by the red-shift of photoabsorption onset of doped materials. The extent of red-shift

depends on the amount and type of dopants and it was found that the red-shift decrease in the following order: V > Cr > Mn > Fe > Ni when these metal ions are implanted into TiO_2[96].

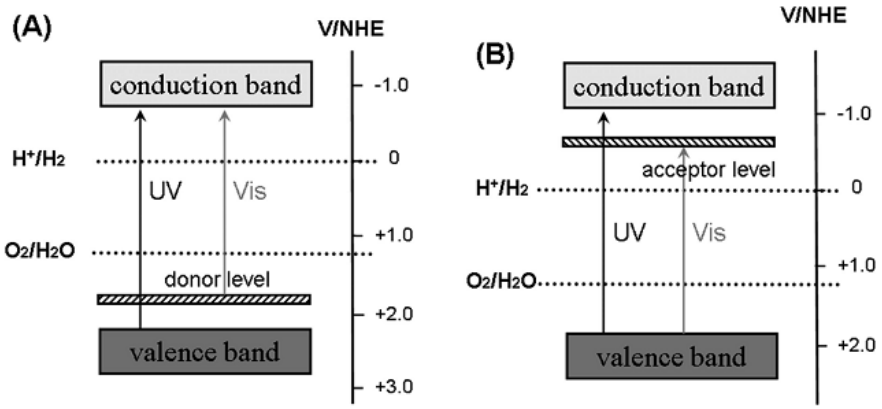

Figure 2.22 Schematic of (A) donor level and (B) acceptor level through metal-ion doping in the application of water splitting . Adapted from Ref[13].

In addition to the altering the band-gap configuration, metal-ion doping can significantly influence photoreactivity through altering charge carrier recombination rates and interfacial electron-transfer rates. Choi *et al*. systematically investigated the role of various metal ions dopants in effecting the photocatalytic activity of quantum sized TiO_2[97]. It was found that while doping with Fe, Mo, Ru, Os, Re, V, and Rh ions at 0.1-0.5 at.% can enhance photocatalytic activity, Co and Al ions cause detrimental effects. The discrepancy between different elements was related to the efficiency of dopants in trapping charge carriers and mediating interfacial charge transfer. The dopant can act as electron and/or holes trapping sites, as indictaed in the following equations[97],

$$M^{n+} + e_{cb}^{-} \rightarrow M^{(n-1)+} \qquad \text{electron trap} \qquad (2.8)$$

$$M^{n+} + h_{vb}^{+} \rightarrow M^{(n+1)+} \qquad \text{hole trap} \qquad (2.9)$$

If the doped ions can trap both electrons and holes, for instance Fe^{3+}, the hole trapped in Fe^{4+} will have longer lifetime due to the immobilized electrons trapped in Fe^{2+}. Thus the recombination between electrons and holes will be inhibitted. If the doped ions can only

trap one type of charge carriers, then the trapped carriers will easily recombine with the mobile counter charge carriers. Thus Cu and Fe, which can trap both electrons and holes, are recommended for doping to improve the photocatalytic activity[98]. However, the metal doping can also cause deterioration of photoactivity. The excess dopants will induce considerable defects in the bulk, which will increase the possibility of recombination. Furthermore, the generated impurity levels are often discrete, which supress the migration of charge carries[99]. Therefore, it should be noted that an optimum doping concentration when utilizing this method to enhance the photocatalytic rate. In addition it should be mentioned that the effect of metal ion doping cannot be simply generalized to all systems, and the actual doping effects depends on doping method, doping conent, doping depth[98,100], and needs to be analysed specifically.

Non-metal ions (N, C, B, S, etc.) have also been investigated to improve the photocatalysts activity in long-wavelength spectrum range. But unlike metal ions, non-metal dopants are less likely to form donor levels, but instead shift the valence band edge upward, as indicated in Figure 2.23. It was observed that X-ray photoelectron spectrum of C, N and S doped TiO_2 showed an increased electron density of state above the valence band of TiO_2, which resulted in red-shift of light absorption[101]. The density of state of substitutional doping with C, N, F, P or S for O in anatase TiO_2 were caculated, and it was concluded that nitrogen doping was the most effective, due to its *p* states mixing with O *2p* state and reducing band gap[102]. N doping has also been successfully applied to other host catalysts, like Ta_2O_5[103], $Sr_2Nb_2O_7$[104], to improve their performance in water splitting.

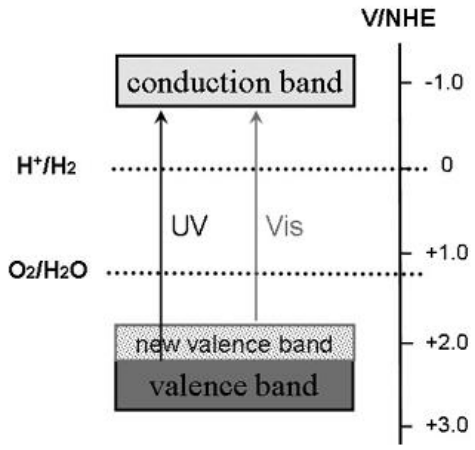

Figure 2.23 New valence band formed through non-metal ions doping. Adapted from Ref[13].

Noble-metals decoration, including Pt, Ag, Au, Pd, etc, has been widely accepted as an effctive strategy to faciliate charge carriers sepraration and enhance the overall activity[105–107]. The Fermi level of the noble metals are usually lower than that of the semiconductors. Thus the noble metal nanoparticles deposited on the surface can play a role of electron trap to prompt the separation of the electron-hole pairs[13,98], as shown in Figure 2.24 (a). In addition to the role of electron trap, the nobel metal nanoparticles have also been demonstrated to induce surface plasmon resonance(SPR) and enhance visible light harvesting of photocatalysts[108–110]. The SPR refers to a phenomenon that the conducting electrons in metal nanoparticles undergo a collective oscillation when the frequency of incident photons matches the resonance conditions of the metal nanoparticles[109], and thus absorb the light. The mechanisms of SPR applied in increasing light-absorption are presented in Figure 2.24 (b). The resonance wavelength depends on not only the type of the noble metals, but also the size, shape and surroudings. Therefore, the light absorption range of the photocatalysts can be manipulated through tunning the size, shape, etc. of the metal nanoparticles[108].

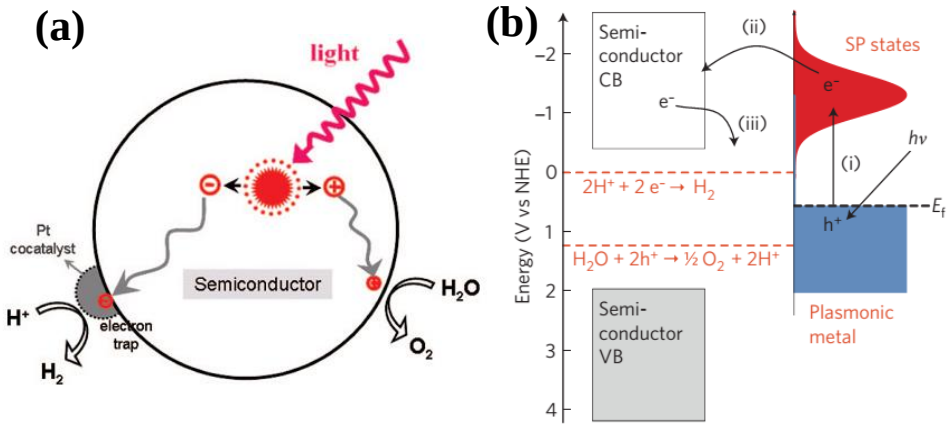

Figure 2.24 (a) the electron-trap role of Pt nanoparticles deposited on semiconductors (b) SPR induced charge transfer,(i) Electrons near Fermi lever are excited to SR states; (ii) the electrons are transferred to the conduction band of semiconductor;(iii) the electrons can participate the reduction reactions. (a) and (b) are adapted from Ref[13] and Ref[108] respectively.

In addition to coupling with these nobel metals, semiconductor-semiconductor combination is another strategy to increase the efficiency. When a large band gap semiconductor is coupled with a small band gap semiconductor, of which the conduction-band edge is more negative compared to the wide bandgap semiconductor, the photoexcited electrons in the small band gap will easily flow into the conduction band of the other semiconductor, inhibitting the recombination. Due to the narrow band gap, this method also sensitizes the large band gap semiconductor, and makes the overall system more active in long-wavelength-spectrum range[111]. The most representive example is CdS/TiO_2, as shown in Figure 2.25 (a). Besides, some semiconductors, like RuO_2, NiO, IrO_2, have been demonstrated to act as effective cocatalysts to prompt water oxidation[112–114]. Furthermore, when combine a n-type semiconductor with a p-type semiconductor, a p-n juction will be formed between the interface. The built-in electric field near the interface can assist charge separation and then enhance the photoactivity[91,115,116], as indicated in Figure 2.25 (b). Overall, the heterostructure has shown its superiority in light

absorption and charge carriers sepration, and has become a widely accepted strategy in designning an effective new type photocatalyst.

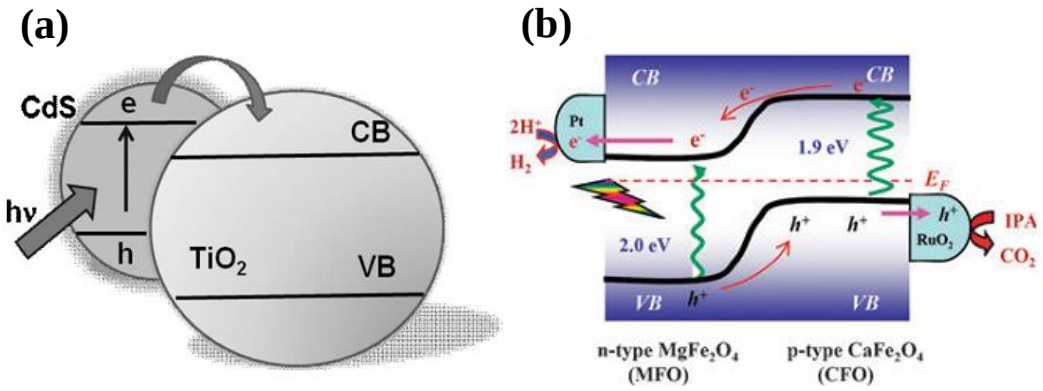

Figure 2.25 a) Electron transfers in CdS/TiO_2 composited structured photocatalyst. (b) Prompted charge carriers seapration in p-n junction applied in photocatalysis. (a) and (b) are adopted from Ref[111] and Ref[116]

As described in section 2.3.2, the morphology of photocatalys plays an important role in determinte the overall efficiency as well. Therefore, morphology control is an effective way to improve the photocatalytic activity. Apart from the various nanostrutures which shows unique priority in charge carrier transport, mesoporous structure demonstrates its advantage in application in photocatalysts[117–119]. It was reported that mesoporous Au/TiO_2 nanocomposites showed high photocatalytic activity in phenol-oxidation and chromium-reduction reactions[118]. It was claimed that the mesoporous provided a huge surface area and reactive sites for photocatalytic reactions. In addition, the thin wall of mesopores allows the charge carriers to migrate to the surface promptly and avoid recombination in the bulk[117,119].

2.4 Ferroelectric materials in the application of photocatalysis

Considering the unique polarisation-dependent surface properties of ferroelectric materials and its semiconductor properties as discussed in the former sections, it can be expected that the application of ferroelectric materials in photocatalysis would be appealing. A number of ferroelectric materials has been successfully employed in organic

dye degradation, water splitting and photoreduction of carbon dioxide, including $BaTiO_3$[120,121], $LiNbO_3$[122], $BiFeO_3$ [123–126]. However, these publications did not relate the ferroelecricity of the catalysts to the efficiency of photocatalysis, and only treated these materials as other non-ferroelectric semiconductors. Herein, more attention are given to the work wherein the effect of ferroelectricity on the performance of photocatalysts are discussed.

2.4.1 Single-phase ferroelectric materials as photocatalysts

Inoue *et al*. firstly reported that the anormalous photovoltatic effects of PZT can give rise to characteristic photocatalytic properties[127]. The anormalous photovoltatic effect of PZT was related to a microscopic asymmetric potential. The direction of photovoltatic current was opposite with polarisation direction, indicating that the movement of charge carriers in ferroelectric can be controlled by the polarisation field. In positive polarized surface, the density of electrons generated under illumination will be higher than that in negative surface due to the migration of electrons to the positive charged surface. Therefore, the photocatalytic activity for water dcomposition was 10 times higher on positive poled surface than negative poled surface. The similar phenomenon was observed in Sr doped PZT[128] and K doped $PbNbO_3$[129].The advtange of postive poled surface in water splitting disappeared above Curie temperature. This is in accordance with disappearance of anormalous photovoltatic effects[128], further supporting the role of ferroelectric polarisation in modifying the photoactivity.

Rohrer *et al*. investigated the photocatalytic activity of solid solution $Ba_{1-x}Sr_xTiO_3$ in degradation of methylene blue[130]. Interestingly it was found that there was a sharp maximum activity at the tetragonal-cubic phase transition boundary, as shown in Figure 2.26. This credit was given to the abnormal high dielectric constant at the phase transition boundary, which will increase the width of space charge layer and charge carrier

separation in this region. The same maximum activity in the composition of phase transition was also observed in Gd doped BFO[131]. These observations demonstrated the feasiblity of utilizing the dipolar field in space charge layer to prompt chagre carrier separation and then photoactivity.

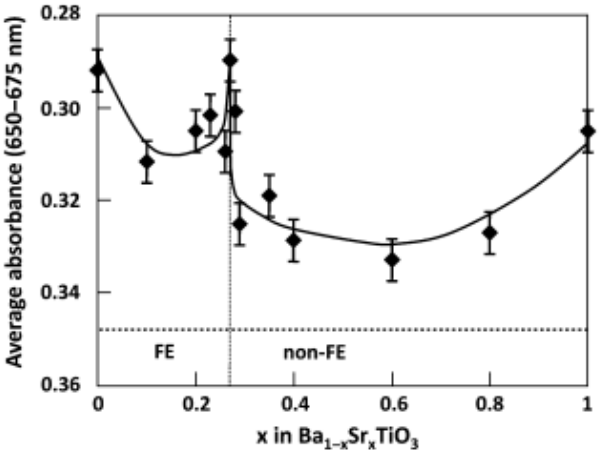

Figure 2.26 Absorbance of methylene blue solution after photoillumination for 200 minutes using a series of photocatalysts with different compositions. Vertical dash line represnts the boundary between ferroelectric and non-ferroelectric. Horizon dash line indicates the initial absorbance of methylene blue solution before photocatalytic reactions. Adaped from Ref[130].

$LiNbO_3$ has also been successfully employed in photocatalysis, ranging from indoor air purification, organic dye decolourisation to photoreduction of carbon dioxide[132–135]. The performance of $LiNbO_3$ in removing voltile organic compounds in indoor environment was found better than the widely used photocatalyst TiO_2 due to its strong remant polarisation(70 $\mu c/cm^2$) [132]. The spatial separation of reduction and oxidation reactions in $LiNbO_3$ powders enables a high rate in dye decolourisation despite its large band gap[133]. Moreover, the advantage of $LiNbO_3$ as a new catalysts in artificial photosynthesis was attributed to the interactions between the ferroelectric surface charge and reactants altered the adsorption energy, and the increased charge carriers lifetime[134,135].

Recently a corona poling method was proposed to polarise the particulate suspension and the polarized photocatalysts $K_{0.5}Na_{0.5}NbO_3$ showed a significantly improved

photoactivity (about 7.4 times) in hydrogen evolution with respect to the non-polarised photocatalysts[136] as presented in Figure 2.27. This phenomenon was due to the internal polarised field inhibiting charge carrier recombination and prolonging the lifetime, which was supported by the slower decay of photoluminescence. This powder-polarisation method provides a new strategy to modify the photocatalytic activity in other particulate-based photocatalytic systems.

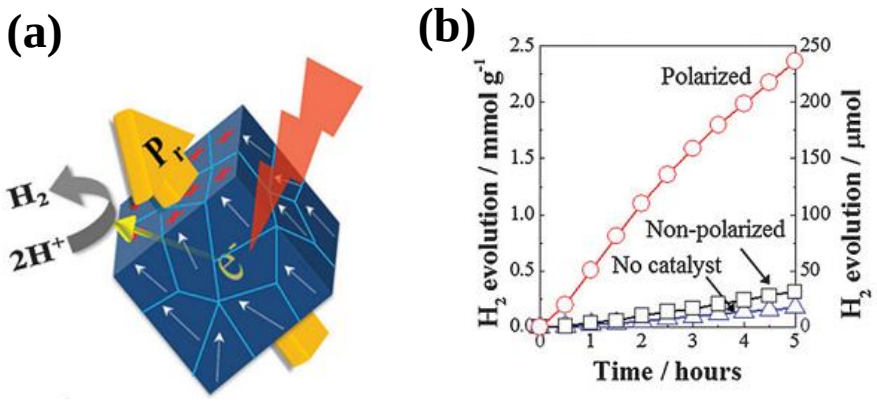

Figure 2.27 (a) Schematic showing mechanisms of polarisation affecting photocatalytic reactions (b) Comparison of H_2 evolution using different photocatalysts. Adapted from Ref [136].

The polarisation related photocatalytic performance has been observed in other ferroelectric materials[137]. As a nonlinear optical material, $K_3B_6O_{10}Br$ shows asymmetric positive and negative charge centres and belongs to ferroelectric materials. It was found that under UV illumination, the dechlorination efficiency of $K_3B_6O_{10}Br$ was two orders of magnitude higher than the commercial products P25. This discrepancy was again ascribed to polarisation field prompting electron-hole separation, as indicated in Figure 2.28. The reduction and oxidation reactions can take place on the surface of photocatalysts spatial separately, which will prohibit the possible back-reactions and enhance the overall efficiency.

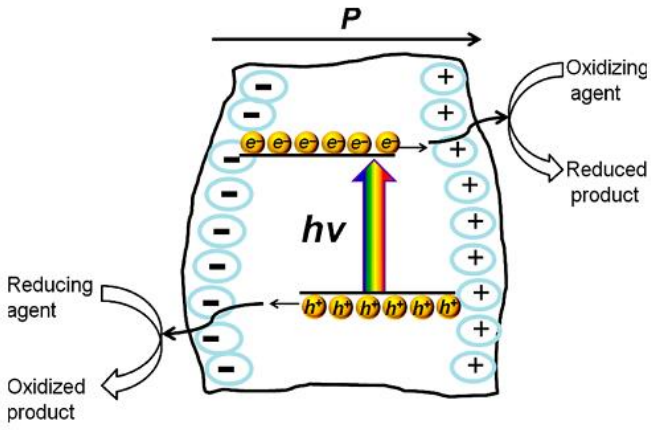

Figure 2.28 Schematic illustration of a non-centrosymmetric structured $K_3B_6O_{10}Br$. Adapted from Ref[137].

2.4.2 Heterostructured ferroelectrics as photocatalysts

As discussed in section 2.2, thin films on ferroelectric substrate show some intriguing polarisation-dependent properties, like surface electric conductivity, spatially separation of charge-carriers. Therefore it can be highly expected that coupling ferroelectric materials with non-ferroelectric semicondictors can exhibit some interesting properties in photocatalysis.

When a thin film of TiO_2 deposited on poled single crystal of $LiNbO_3$ with a polarisation direction perpendicular to the surface, the photocatalytic activity in water decomposition was improved remarkably[138]. It was discussed that the underlying polarisation can influence the movement of the photogenerated carriers in the thin film and then the overall photoactivity. The similar observation was reported in the other semiconductor-metal-ferroelectric device systems[139]. The positive polarised suface exhibited higher activity in hydrogen generation than the negative polarized surface bacause the underlying positive polarisation faciliate the electron transport from TiO_2 to Pt, which is the active site for hydrogen production.

A series of heterostructured photocatalysts combining ferroelectrics with non-ferroelectrics have been reported[140–145]. $BiFeO_3/TiO_2$ core-shell nanoparticles was

reported to show a high rate of photocataltytic degradation of Congo red under visible light[140]. Similarly $BiFeO_3/TiO_2$ nanotube arrays was successully synthesised and found to exhibit a higher photoelectrocatalytic activity then pure TiO_2 nanotube arrays[141]. The enhanced photovoltage and photochemical activity was related to the loaded ferroelectric $BiFeO_3$ nanoparticles on the surface of TiO_2. The polarisation in $BiFeO_3$ decrease the chance of recombination between photoexcited electrons and holes. The similar heterostructured PZT/TiO_2 has also been demonstrated to exhibit efficient photocatalytic activities in decomposing ethylene in gas phase under visible light irradiation[142].

Rhorer *et al.* sysmetically investigated the effect of ferroelectric core size on the overall photocatalytic efficiency[143]. They chose microcrystalline and nanocrystalline $BaTiO_3$ as different core and coated with nanostructured TiO_2. Under the same experimental conditions, the microcryatalline $BaTiO_3$-TiO_2 showed higher hydrogen generation rate than the nanocrystalline $BaTiO_3$-TiO_2. The authors proposed three possible reasons to account for this. The smaller core particle size will not permit siginificant band bending, and will result in a decrease in magnitude of spontanaous polarisation as well. In addition, the dielectric constant in the nano-size particles was smaller than that of micro-size particles. All these factors will reduce the width of space charge layer in the core, and decrease the chance for the charge carriers to be separated, transfered to the nanostructure shell and involved in redox reactions successfully[143]. The band diagram of heterostructured photocatalysts are shown in Figure 2.29, where the effect of polarisation on the band bending at the interface are schematically presented.

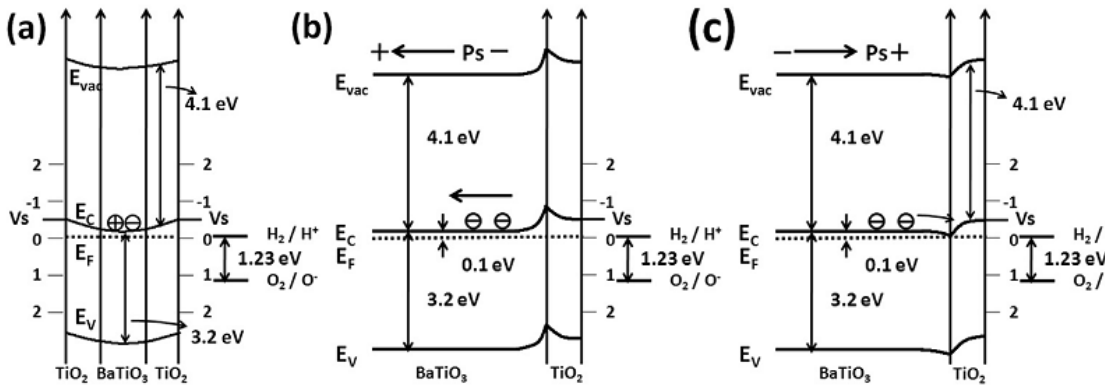

Figure 2.29 Schematic of band diagrams (a) nanocrystalline $BaTiO_3$-TiO_2, (b) microcryatalline $BaTiO_3$-TiO_2 with negative polarisation in ferroelectric core, and (c) microcryatalline $BaTiO_3$-TiO_2 with positive polarisation in ferroelectric core. Adapted from Ref[143].

The similar heterostructure coupling microcrystalline core and nanocrystalline shell was extended to $PbTiO_3$-TiO_2[144]. In addition to the prompted charge carriers separation arising from the ferroelectric polarisation, $PbTiO_3$ also played another role of visible light absorption centre due to its narrow band gap 2.85eV. This further enhanced the photocatalytic acitivity of the composited catalysts.

Overall, the internal polarisation field in ferroelectric materials can effectively separate photogenerated electrons and holes, and then further spatially separate the reduction and oxidation reactions. This provides a new strategy to overcome the bottlenecks which limits the photocatalytic efficiency as reviewed in section 2.3. Moreover, this polarisation effect can also be controlled to impact on the non-ferroelectric thin films/shell, which makes ferroelectrics an attracking group of materials to be combined with other materials to make an efficient composited photocatalyst[91].

2.5 Ferroelectric materials used in this research

2.5.1 Barium titanate

Barium titanate is the first reported perovskite structured ferroelectric material[146]. It can exist in different crystalline structures at different temperatures, as shown in Figure 2.30.

The Curie temperature(Tc) of $BaTiO_3$ is around 120 ℃, above which ferroelectric tetragonal phase transform into non-ferroelectric cubic[147]. The ferroelectricity of $BaTiO_3$ arises from the displacement of the body-centred Ti ions and the unit cell will exhibit distortion as shown in Figure 2.30. At room temperature, the spontaneous polarisation of tetragonal $BaTiO_3$ is 26~27 μC/cm^2 [148].The band gap of $BaTiO_3$ bulk was reported to be around 3.2 eV.When the size of $BaTiO_3$ particle smaller than 11.5 nm, it was observed that the band gap increased, and was approximately 3.47 eV for the particle size of 6.7 nm[149].

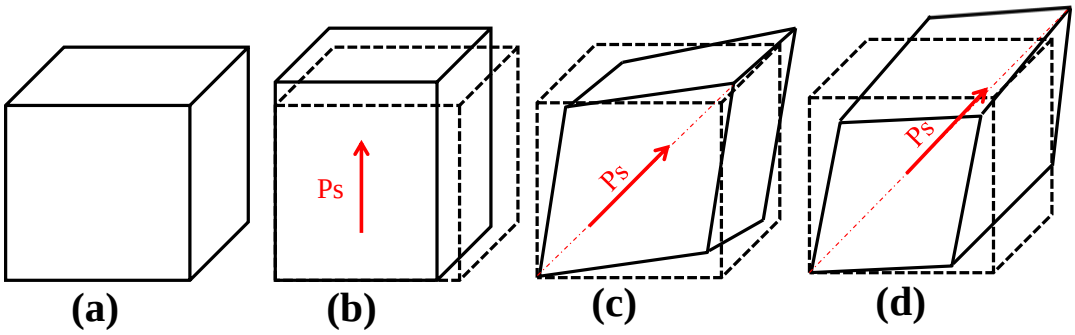

Figure 2.30 Unit cells of the four phases of $BaTiO_3$ (a) cubic, stable above 120 ℃ (b) tetragonal, stable between 5 ℃ and 120 ℃ (c) orthorhomic, stable between -90 ℃ and 5 ℃, (d) rhombohedral, stable below -90 ℃. The arrows show the direction of polarisation in ferroelectric phases. Adapted from Ref[147].

As discussed in section 2.1.5, the size effect of $BaTiO_3$ makes the non-ferroelectric phase – cubic, which is thermodynamically nonstable below 120 ℃, exist at room temperature if the crystalline size is smaller than the critical size. Therefore $BaTiO_3$ can exist in both non-ferroelectric cubic phase and ferroelectric tetragonal phase at room temperature.

Due to its outstanding dielectric and pielectric properties, barium titanate has been widely applied in various field of engineering, like multilayer ceramic capacitors and positive tempertature coefficient thermistors[150]. In addtion to that, more and more attention are given to the photochemical properties of ferroelectric $BaTiO_3$ which are closely related to its spantaneous polarisation, as reviewed in section 2.2 and 2.4. As a photocatalyst with

internal field, its promising applications in water purification and hydrogen generation open a new window for sustainable energy cycle[91].

Chapter 3

Experimental Procedures

3.1 Photodeposition of Ag nanoparticles on $BaTiO_3$

Barium titanate was supplied by Sigma ($BaTiO_3$, 99.9% trace metal basis, <2 μm). A portion of $BaTiO_3$ powder was thermal-treated. For thermal treatment, $BaTiO_3$ powder was placed in an alumina crucible and heated at 1200 ℃ for 10 hours in air in a tube furnace (Model ST 12 series of M.L.FURNACE) followed by natural cooling. After annealing, the agglomerated powder was ground in a pestle and mortar to produce a fine powder. The as-received $BaTiO_3$ and thermal treated $BaTiO_3$ was accordingly named as BTO and BTO-anneal.

Silver metallic nanoparticles were deposited on the surface of $BaTiO_3$ by using photoreduction methods. The mechanism of photodeposition of Ag nanoparticles is shown in Figure 3.1. The photo-generated electrons are excited from valence band to conduction band, and the conduction band edge of $BaTiO_3$ is more negative than the reduction potential of Ag^+/Ag. Therefore the electrons are capable of reducing Ag ions to metallic Ag nanoparticles.

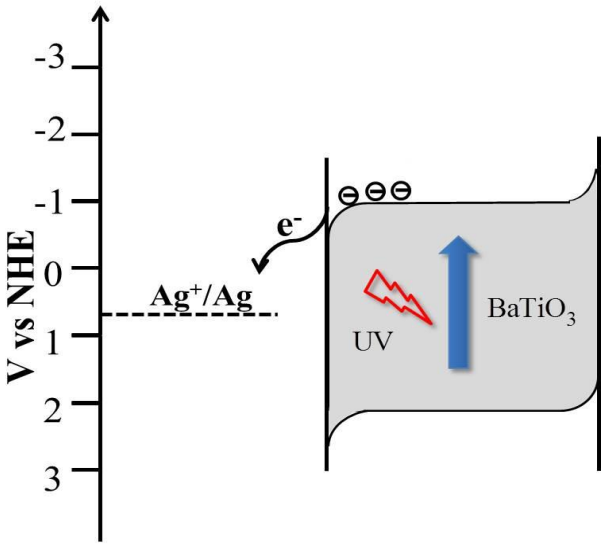

Figure 3.1 Band gap positions of $BaTiO_3$ (tetragonal) and the reduction potential of Ag+ against Normal Hydrogen Electrode (NHE)

1 g of BTO or BTO-anneal was weighed and loaded into a beaker holding 50 ml of 0.01 M $AgNO_3$ solution. The beaker was placed under a UV illumination source (Honle, UV Cube with a high pressure Hg lamp), which gives an irradiation of 5.54 mW/cm^2. The spectrum of UV irradiation is shown in Figure 3.2. The distance between the bottom of beaker and the light source was fixed at 5.5 cm and the powder was irradiated for different time (30s, 5min and 10min) under constant stirring. The powder was then separated from the solution using a centrifuge, followed by washing with DI water 3 times and drying at room temperature.

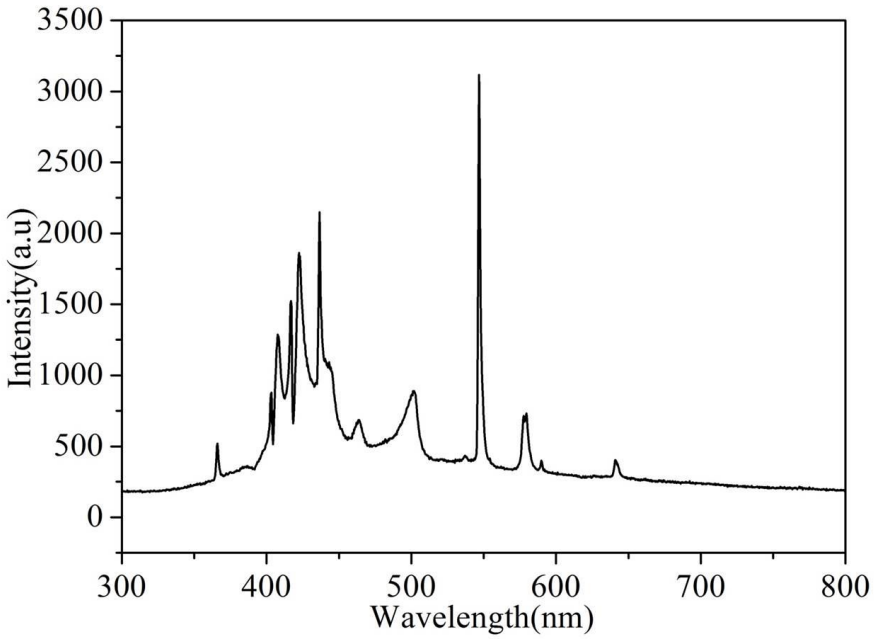

Figure 3.2 Irradiation spectrum of UV cube (high pressure Hg lamp) employed in photoreduction of Ag nanoparticles

3.2 Photodecolourisation of organic dyes under different irradiation conditions

The photocatalytic activities of photocatalysts were assessed by photodecolourisation of organic dyes under irradiations with different wavelength range. The organic dyes used in this research are listed in Table 3.1 and their chemical structures are shown in Figure 3.3.

Table 3.1 Organic dyes used in this research

Name	Chemical formula	Molecular weight (g/mol)	Supplier	Wavelength of maximum absorption (λ_{max})
Acid Black 1	$C_{22}H_{14}N_6Na_2O_9S_2$	616.499	Acros Organics	620nm
Rhodamine B	$C_{28}H_{31}ClN_2O_3$	479.01	Sigma, analytic grade, >97%(HPLC)	514nm

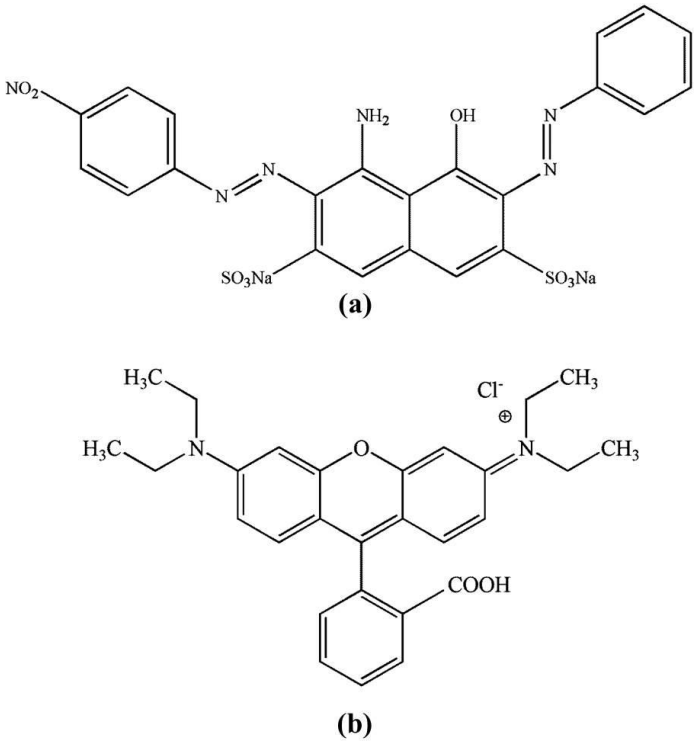

Figure 3.3 Chemical structures of (a) Acid Black 1 and (b) Rhodamine B

The organic dye solutions with a concentration of 10ppm were prepared by dissolving the required amount of dye into deionized water. Decolourisation of organic dye was performed in a quartz petri dish after mixing 0.15 g catalyst powder with 50 ml of 10 ppm dye solution， as shown in Figure 3.4. The mixture was stirred in the dark for 30minutes before exposure under a solar simulator (Newport, class ABB) fitted with an AM 1.5 filter at a distance of 17 cm from the light source. The irradiation intensity was fixed at 1 sun (100 $mWcm^{-2}$) using a silicon reference cell. 2 ml of solution was taken for sampling at

fixed intervals followed by centrifugation at 4000 rpm for 30minutes to remove any catalyst powder. The obtained dye solutions were ready for UV-Vis analysis.

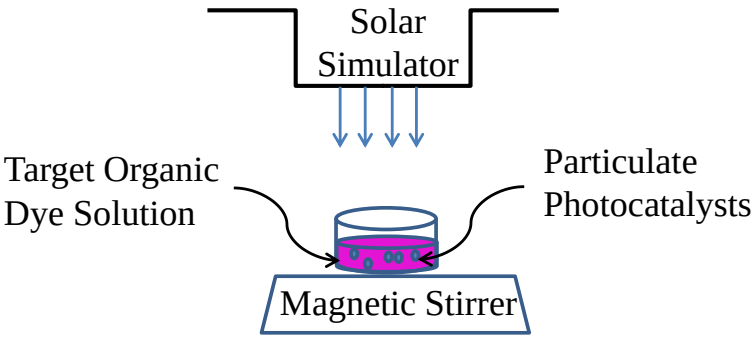

Figure 3.4 Schematic of experimental setting up of photodecolourisation of organic dye

In order to demonstrate the effect of centrifugation on the separation of photocatalysts particles and RhB molecules, the sedimentation coefficient S of $BaTiO_3$ and RhB were calculated.

$$S = \frac{2r^2(\rho_P - \rho_M)}{9\eta} \tag{3.1}$$

where r is the size of particles, ρ_P and ρ_M are the density of particles and liquid medium respectively, and η is the viscosity of the medium.

In this work, we calculate the sedimentation coefficient ratio S_{BTO}/S_{RhB} to clarify the feasibility of centrifugation on separation $BaTiO_3$ and RhB. The average size of $BaTiO_3$ particles is considered as 386 nm based on SEM analysis(detailed in Figure 5.2 and Table 5.1), and the size of RhB molecule is assumed to be 1.6 nm[151].The density of $BaTiO_3$, RhB molecule, and DI water are considered to be 6.08 g/ml, 1.31 g/ml[152] and 1 g/ml at room temperature respectively. Using equation (3.1), the sedimentation coefficient ratio can be calculated, $S_{BTO}/S_{RhB} \approx 953754$. Therefore, a much higher sedimentation coefficient of $BaTiO_3$ compared to RhB molecule indicated that $BaTiO_3$ particles are easily sedimented and separated with minor RhB molecule removed during a limited-time centrifugation.

Herein it should be mentioned that in addition to artificial solar light, the irradiations with different wavelength range were used in some experiments, including UV light only and visible light only. Under these conditions, UV-block filter (UQG Optics LTD, UV blocking, 50 mm*50 mm, 1.1 mm) and visible-block filter (UQG Optics LTD, Schott UG1, 50 mm*50 mm, 2 mm) were placed between irradiation source and dye. The flux of incident light was maintained when filters were used. The spectra of solar light, UV-block and visible-block were shown in Figure 3.5.

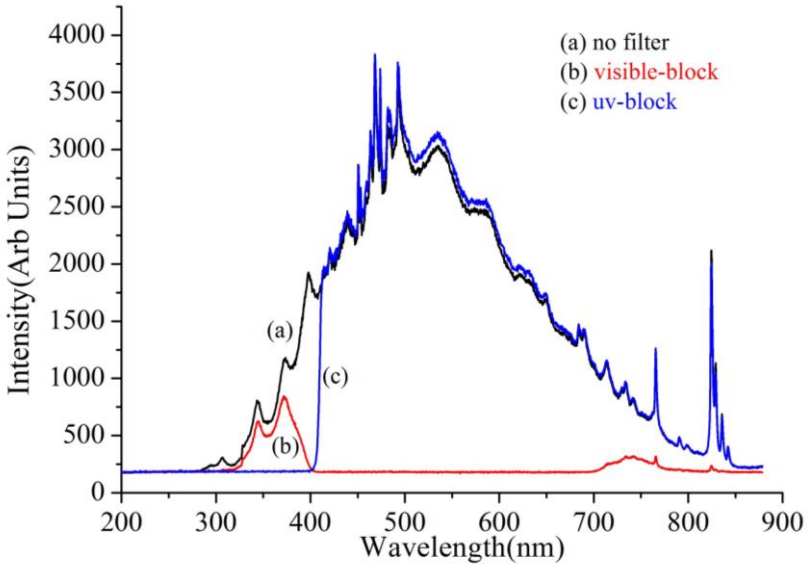

Figure 3.5 Irradiation spectra of artificial sunlight and that after blocking visible-light and UV

In the investigation of effect of pH on the photodecolourisation efficiency, 0.1M HCl or 0.1M NaOH was used to adjust the pH of the initial dye solution to around 2 and 11 respectively. Then the pH values of the obtained dye solutions and that without adjustment were measured using pH metres (Mettler Toledo). Then the photocatalysts were add in and followed the procedures described above to get the photodecolourisation profiles under different pH conditions. It should be mentioned that the pH of the dye solutions were not controlled during the photodecolourisation process.

In the detection of reactive species in the photodecolourisation process, ethanol was added into the dye solution to act the radical scavenger. Specifically 10 ml of ethanol (GP grade) was added into 40ml RhB (10ppm) solution, and then the obtained solution was mixed with photocatalysts and followed the decolourisation procedures. As the referential sample, 10 ml of deionized water instead of ethanol was added into 40ml RhB (10ppm) solution to keep the initial concentration of RhB identical to that of ethanol added. Then the same photodecolourisation was carried out.

3.3 Synthesis of heterogeneous $BaTiO_3$-anneal/α-Fe_2O_3

The heterostructured $BaTiO_3$-anneal/α-Fe_2O_3 powder catalysts were prepared using the method reported[153,154]. The required amount of $Fe(NO_3)_3$•$9H_2O$ were dissolved in 30ml ethanol to obtain a concentration (Fe^{3+}) of 0.001M, 0.01M,0.1M and 0.5M respectively. 1.5 g treated $BaTiO_3$-anneal was added into the ethanol solution, and vigorously stirred at room temperature for 30 minutes, followed by ultra-sonication for 30 minutes. Then the solutions were evaporated at 50 ℃. The obtained powder was annealed at 300 ℃ for 10minutes, followed by ethanol washing thoroughly. Finally the powder was annealed at 300 ℃ for 6 hours. The as-prepared powder was simply named as BTO-anneal-Fe_2O_3-0.001M, BTO-anneal-Fe_2O_3-0.01M, BTO-anneal-Fe_2O_3-0.1M and BTO-anneal-Fe_2O_3-0.5M respectively. For reference, pure α-Fe_2O_3 was also prepared using the same method without adding BTO-anneal.

3.3 Materials Characterisation

3.3.1 Scanning Electron Microscopy

The morphologies of the powders were studied using a scanning electron microscope (SEM, FEI Inspect F). The elementary compositions of the samples were analysed using attached energy-dispersive X-ray spectrometer (EDX). The conductive powders were dispersed and attached on top of the carbon tape. Excessive particles which were not

attached to the tape firmly were removed by air blow to avoid the contamination of the vacuum chamber.

3.3.2 Transmission Electron Microscopy

The microstructures of the powders were further investigated by using a transmission electron microscope (TEM, Jeol JEM 2010). The elementary composition of selected local area were analysed using EDX as well. Proper amount of powder samples (c.a. 0.01 g) were dispersed into ethanol, followed by ultrasonication for 10 minutes. Then the copper grid was dipped into the suspension and dried at room temperature.

3.3.3 X-ray Diffraction

The phase compositions of the powder photocatalysts were analysed by X-ray diffraction (XRD) using Panalytical Xpert Pro diffractometer with Cu-Kα radiation. The range of XRD scan was between 5 ° to 70 ° and in a continuous scan mode at a scan speed of 0.6 °/min with a collection width of 0.0167 °.

3.3.4 X-ray Photoelectron Spectoscopy

The surface compositions of the powders were analysed by Thermo Scientific K-Alpha X-ray photoelectron spectroscopy with an Al Kα source (1486eV). All the binding energies were referenced to C 1s peak at 284.9eV of the surface adventitious carbon. The XPS analysis was performed in Newcastle University, National EPSRC XPS Users Service (NEXUS).

3.3.5 Brunauer-Emmett-Teller (BET) Surface Area Analysis

The BET surface area of powder photocatalysts were analysed Micromeritics Gemini VII surface area analyser using N_2 as the adsorptive gas. Before the measurement, the samples were dehydrated at 100ºC for 4 hours under N_2 atmosphere.

3.3.6 UV-Vis Spectrophotometer

The concentration changes of dye solution during photodecolourisation process were monitored by UV-Vis spectrophotometer. The measurement of concentration of absorbing species using UV-Vis spectrophotometer is based on Beer-Lambert law (Equation 3.1).

$$\mathrm{A} = -\log\frac{I}{I_0} = \varepsilon * c * l \tag{3.1}$$

Where A represents the absorbance, I and I_0 represents the intensity of light after and before it passes through the samples respectively, ε is the extinction coefficient, c is the concentration of absorbing species, and l represents the path length of the light.

Based on Equation 3.1, it can be seen that there is a direct proportional relationship between the absorbance of the samples (A) and the concentration of the samples(c) when ε and l are fixed. Therefore, the value of absorbance obtained from UV-Vis spectrophotometer can be used as a criterion to assess the change of dye concentration. The measurement was performed on a Perkin Elmer Lambda 950 UV-Vis spectrophotometer.

For analysis, 1.5ml of dye solution sample was transferred to cuvettes (semi-micro, PMMA, optical path length 10mm, range of application 300nm~900 nm), and then inserted to the sample holder position. All samples were auto-calibrated using deionized water as reference.

The absorbance spectrum of powder samples were also obtained on Perkin Elmer Lambda 950 UV-Vis spectrophotometer with an integrated sphere attachment by converting the diffuse reflectance spectrum. 1g powder samples were placed into the special powder holder, and then screwed tightly. The powders were pressed into a thin disc during the

screwing process. A $BaSO_4$ pure white disc will be used as a reference sample during measurement.

3.3.7 Proton Nuclear Magnetic Resonance (^{1}H NMR)

During the photodegradation of organic dye (Rhodamine B), the degradation pathways and accordingly the possible changes of dye molecules were investigated by proton nuclear magnetic resonance. The proton NMR spectrum of the dye solution was obtained using a Bruker NMR spectrometer operating at 600 MHz at 300 K.

The samples for NMR analysis were prepared using the following methodology: 200 ml of 10 ppm RhB solution were mixed with 0.6 g catalysts, followed by dark-equilibrium for 1 hour, irradiation under solar light for a predetermined time, sampling, and centrifugation. The solvent of the obtained solution (30 ml) was evacuated under reduced pressure at 45°C using a rotary evaporator. The remaining residue was dissolved in 1ml D_2O and transferred into NMR tube ready for analysis.

3.3.8 Gas Chromatography Mass Spectrometry (GC-MS)

The intermediates during photodegradation of Rhodamine B were identified by GC-MS (Agilent GC-MS, a 6890 gas chromatography interfaced with 5973 Mass Selective Detector). To improve the signal to noise values from the GC-MS, the initial concentration of RhB was increased from 10 ppm to 50 ppm, all other experimental parameters remained the same. After the procedures of preparing a reaction solution at different irradiation times, the pH values of the solutions (30 ml) were adjusted by 1M HCl to around 3.0 and then the aqueous solutions were extracted by dichlromethane (DCM, Reagent Degrade) three times. The solutions were dehydrated by anhydrous sodium sulphate and the solvents were removed by rotary evaporation. After the residue was dissolved in 1ml DCM, 0.5 ml N,O-Bis(trimethylsilyl)trifluoroacetamide (BSTFA,

Sigma, ＞99 %) was added in and the resulting solution was kept at 50 °C for 30 mins to drive trimethylsilylation.

3.3.9 Zeta Potential Test

When particles are dispersed in solutions, due to the interactions between ions in the solutions and net surface charge of particles, an electric double layer will develop around the particles. The liquid layer surrounding the particles consists of an inner region (Stern layer), where the ions are tightly bounded, and an outer region (Diffuse layer) where the ions are less firmly associated. In the diffuse layer, there is a notional boundary. When a particle moves, e.g. due to gravity, the ions within the boundary will move with the particle while those beyond this boundary will not. The potential at this boundary is the Zeta Potential (Fig. 3.6).

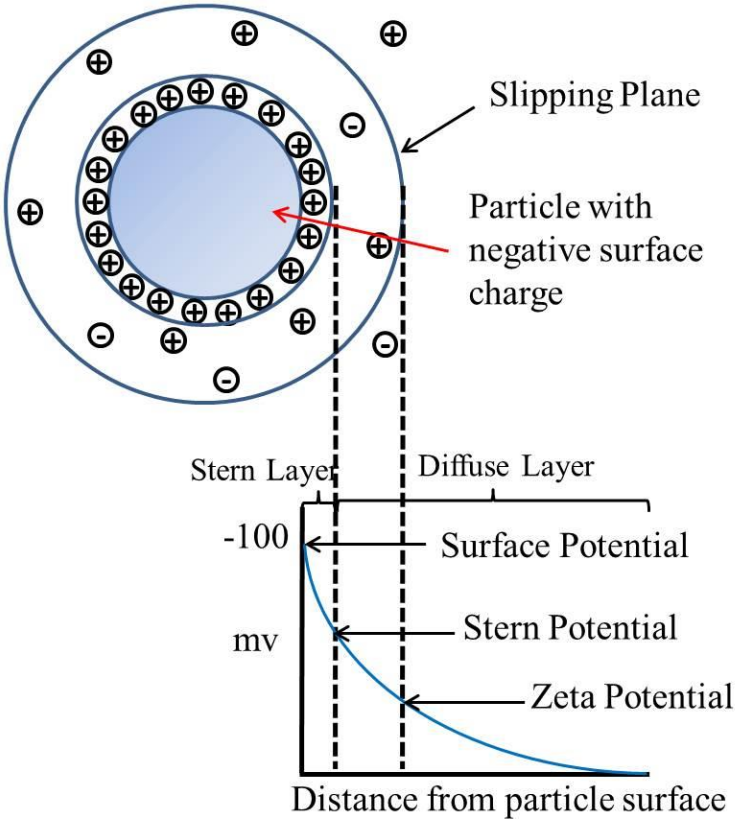

Figure 3.6 Schematic of zeta potential

The zeta potential of photocatalysts was determined using Zetasizer Nano (Malvern CO.U.K). 10 mg photocatalyst was dispersed in 10 ml DI water different pH adjusted by 0.1M NaOH or 0.1M HCl.

Chapter 4

Photocatalytic activity of Ag decorated $BaTiO_3$ in photodecolourisation of organic dye

Surface decoration with noble metal nanoparticles has been widely adopted as an effective strategy to improve the overall efficiency of photocatalysts through inhibiting the charge carriers recombination and/or enhancing visible light response by surface plasmon resonance (SPR) [105–110]. In this chapter, silver nanoparticles were deposited on the surface of as-received $BaTiO_3$ using a photodeposition method. The effect of different photodeposition time (irradiation time under UV lamp) and pH on the photocatalytic activity were studied. In addition, the reactive species which play an important role in photodecolourisation process were identified preliminarily.

4.1 Characterisation of photocatalysts

The morphologies of as-received BTO and Ag decorated BTO (Ag-BTO-30s, Ag-BTO-5min and Ag-BTO-10min) were analysed under SEM, as shown in Figure 4.1.

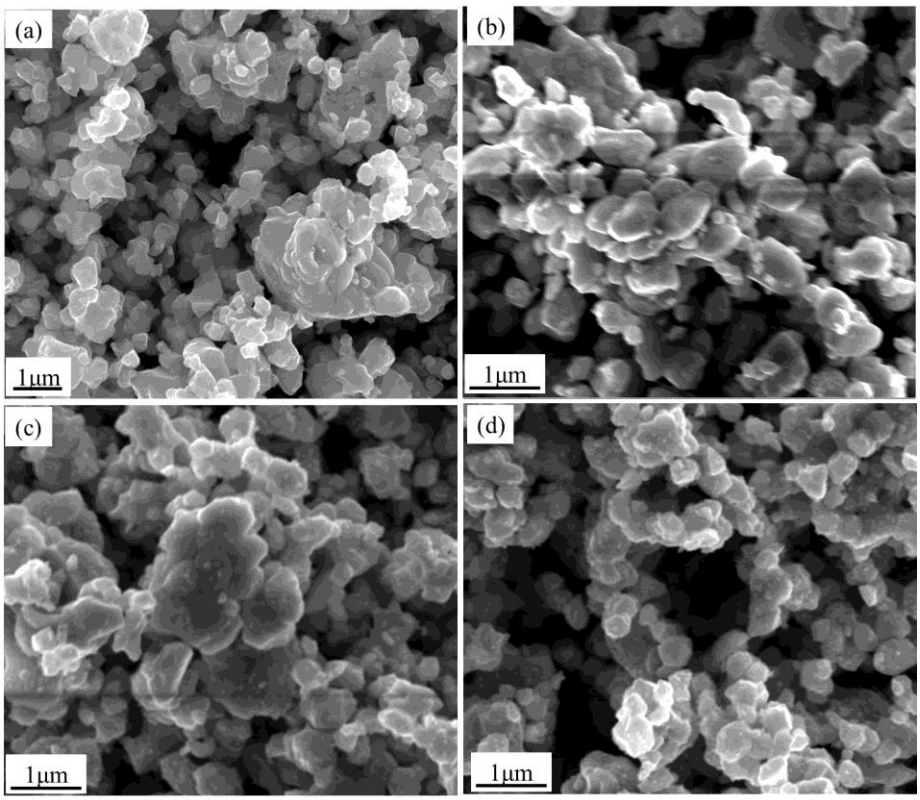

Figure 4.1 SEM micrographs of (a) BTO, (b) Ag-BTO-30s, (c) Ag-BTO-5min and (d) Ag-BTO-10min

The as-received BTO showed a large size-distribution, as indicated in Fig. 4.1(a). After photodeposition of Ag nanoparticles, there was no obvious morphology change. The chemical compositions of these samples were analysised by EDX. It was found that Ag signals were detected in Ag-BTO-5min and Ag-BTO-10min except Ag-BTO-30s. Figure 4.2 shows the obtained EDX spectrum of Ag-BTO-5min and a summary of weight percentage of Ag in different Ag-BTO samples was listed in Table 4.1. The absence of Ag signals in Ag-BTO-30s was related to the low amount of Ag, which was below the detection limitation of EDX.

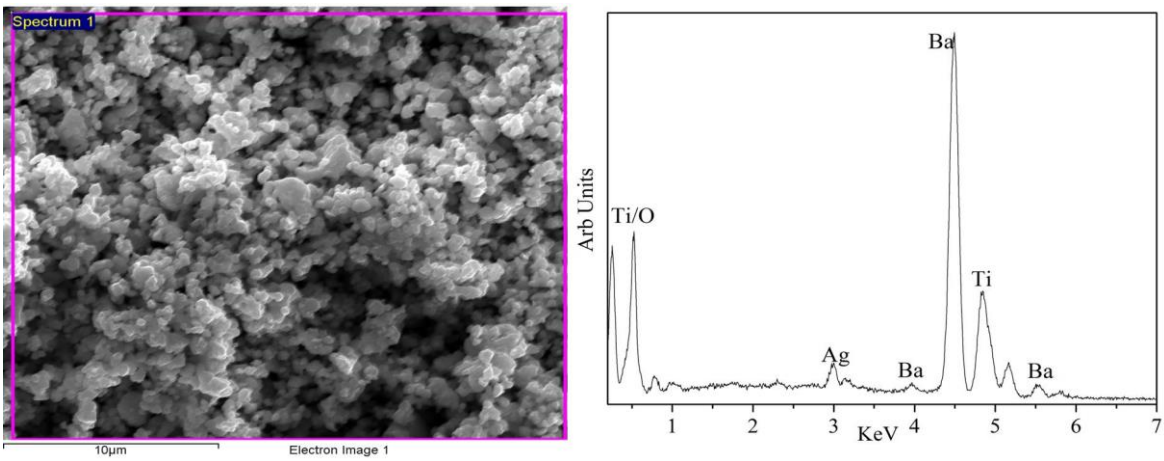

Figure 4.2 SEM micrographs of Ag-BTO-5min at low magnification and accordingly EDX spectrum of selected area, indicating the presence of Ag element.

Table 4.1 Chemical compositions of Ag decorated BTO

Sample	Ag-BTO-30s	Ag-BTO-5min	Ag-BTO-10min
Ag amount (weight%) based on EDX	Not detected	1.91±0.03	3.46±0.19

As shown in Table 4.1, the amount of Ag increased along with the increase of photodeposition time. A similar relationship between irradiation time and amount of photodeposited metallic particles was also reported[155,156]. Herrmann et al.[156] found that the mass of deposited Ag per unit mass of TiO_2 increased linearly with irradiation time. This is plausible considering the mechanism of photodeposition, i.e. Ag ions adsorbed on the suface of BTO were reduced by photoexcited electrons when BTO was exposed under irradiation. Increasing illumination time led to the agglomeration of Ag nanoparticles (supported by Fig. 4.3, TEM micrographs), which gave rise to the increased mass of Ag[155]. The detailed mechanism will be discussed further below with respect to TEM results.

The microstructures of these photocatalysts were further investigated using TEM. Figure 4.3 shows the TEM images of plain BTO and Ag-modified BTO with a range of deposition times. Compared to the smooth edge of bare BTO (Figure 4.3(a)), small

particles attached onto the surface of Ag decorated BTO were observed. This phenemeon became more obvious with respect to the samples with longer deposition time. EDX analysis of these particles confirmed the presence of Ag, which was in consistence with SEM/EDX results. Comparing between samples with different illumination time, the size of Ag nanoparticles increased with increase of photodeposition time, from about 5 nm in Ag-BTO-30s (Figure 4.3(b)) to over 15 nm in Ag-BTO-10min (Figure 4.3(d)). Here it should be mentioned that the distribution of Ag nanoparticles on the surface was not uniform, which was related to the varied surface enegy of the different sites on the surface. It has been reported that Ag nanoparticles with large diameters preferentially grew at grain boundaies and edges of commercial TiO_2, where higher photoreactivity resided[157].

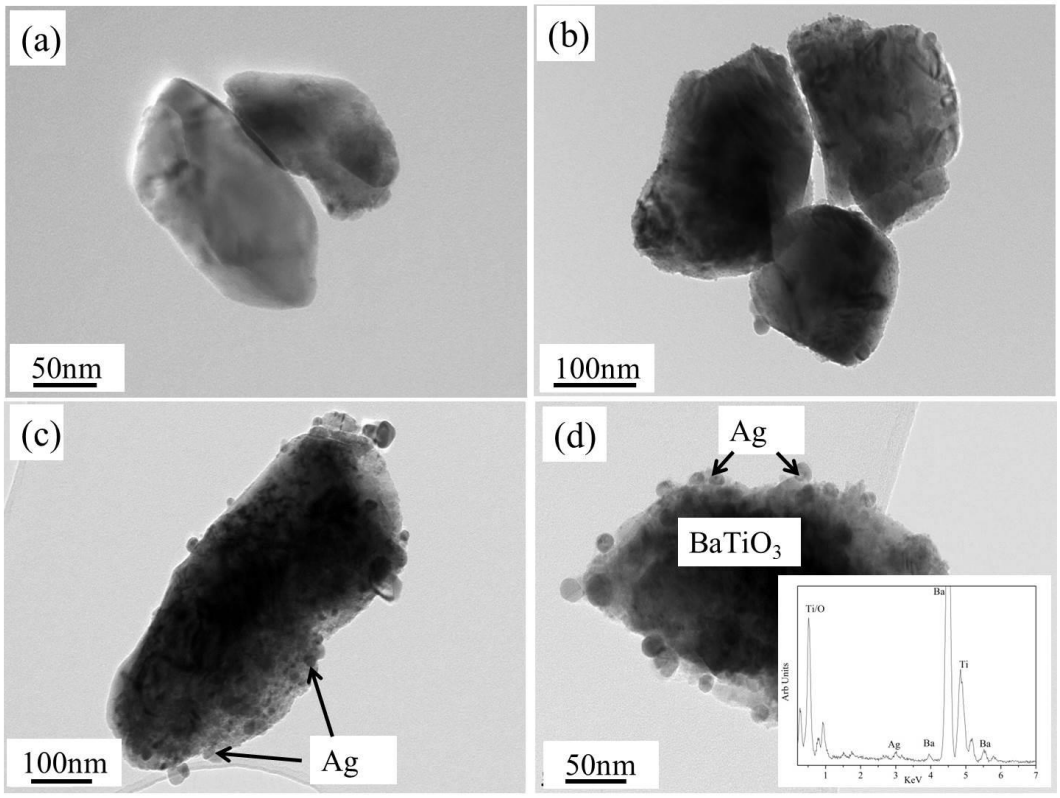

Figure 4.3 TEM micrographs of (a) BTO, (b) Ag-BTO-30s, (c) Ag-BTO-5min and (d) Ag-BTO-10min, EDX spectrum inset, showing Ag particle size increase with increasing of photo-irradiation time.

The photodeposition of Ag nanoparticles mainly involes the following steps[156]: generation of electron-hole pairs in photocatalysts Eq. (4.1), the reaction of holes with adsorbed oxygen species Eq. (4.2) or hydroxyl ions Eq. (4.3), and the reactions of electrons with adsorbed Ag ions Eq. (4.4) :

$$\text{Semiconductor Photocatalysts} + h\mu \rightarrow e^- + h^+ \quad (4.1)$$

$$O_x^- + h^+ \rightarrow \frac{x}{2}O_2, \text{ x=1 or 2} \quad (4.2)$$

$$OH^- + h^+ \rightarrow OH^0 \rightarrow \frac{1}{2}H_2O + \frac{1}{4}O_2 \quad (4.3)$$

$$Ag^+ + e^- \rightarrow Ag^0 \quad (4.4)$$

Here hμ represents the irradiation energy absorbed by the semicondutor photocatalysts, e^- and h^+ represent photoexcieted eletrons and holes respectively.

Formation of small Ag metallic nanoparticles can take place through agglomeration of these Ag atoms Eq. (4.5) :

$$\text{m}Ag^0 \rightarrow Ag_m \quad (4.5)$$

or successive reduction Eq. (4.6):

$$Ag^0 + Ag^+ \rightarrow (Ag)_2^+ \xrightarrow{e^-} Ag_2 + Ag^+ \rightarrow (Ag)_3^+ \xrightarrow{e^-} Ag_3 \rightarrow \cdots Ag_m \quad (4.6)$$

A similar trend of increasing in the size of photodeposited metallic nanoparticles with increase of illumination time has been reported due to aggregation of small particles[157,158]. Based on SEM/EDX and TEM analysis, it can be concluded that longer illumination time gave rise to increase in both Ag nanoparticles size and mass.

X-ray diffraction was employed to investigate the phase composition of these photocatalysts. The XRD patterns are presented in Figure 4.4. As shown, the majority of

the peaks were assigned to cubic BTO (JCPDS 31-0174). In addition, an extra peak at 2θ=38.1 ºwas observed in Figure 4.4 (c) and (d). This peak matched with the standard XRD peak (111) of metallic Ag (JCPDS 04-0783). Moreover, the extra peak at 2θ=64.4 º labelled in Figure 4.4 (d) was assinged to (220) of metallic Ag. The absence of Ag peak in Ag-BTO-30s was attributed to the lowest amount of Ag loading in the sample, which was consistent with the absence of Ag signals in SEM/EDX.

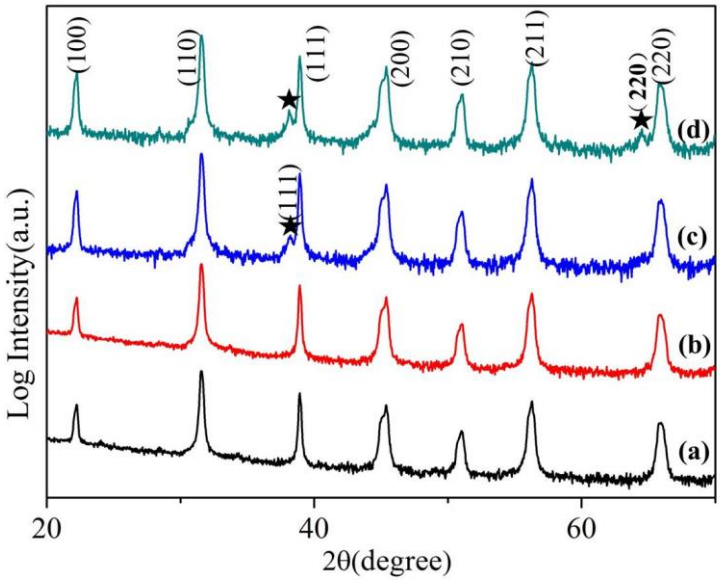

Figure 4.4 XRD patterns of (a) BTO, (b) Ag-BTO-30s, (c) Ag-BTO-5min and (d) Ag-BTO-10min. The characteristic peaks of BTO were labelled. The (111) and (220) peaks of Ag were labelled as well.

The surface composition and elemental chemical state of photocatalysts were analyzed by XPS. As indicated in Figure 4.5, the overall spectrum of BTO overlapped well with that of Ag-BTO-30s except some extra peaks existed in the spectrum of Ag decorated sample. These peaks and their binding-energy were Ag 3p1/2 at 603.68 eV, Ag 3p3/2 at 572.88 eV, Ag 3d3/2at 373.49 eV and Ag 3d5/2 at 367.49 eV. The peak positions were consistent with the reported value for metallic Ag[159] (NIST X-ray Photoelectron Spectroscopy Database). In addition, it was reported that the spin-orbit splitting of the 3d doublet for metallic Ag was 6.0 eV[120,160], and this was in agreement with the value obtained herein. Overall, combining the results of SEM/EDX, XRD, TEM/EDX and XPS,

it can be concluded that metallic Ag nanoaprticles were successfully loaded on the surface of BTO.

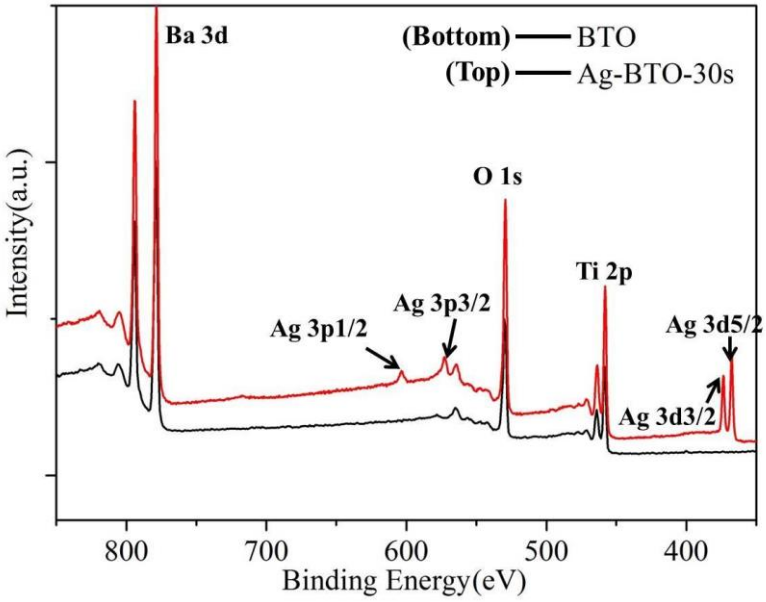

Figure 4.5 XPS spectra of BTO and Ag-BTO-30s. The additional characteristic peaks of metallic Ag confirmed the successfully Ag loading on the surface.

The optical peroperties of photocatalysts were studied and the UV-Vis diffuse reflectance spectra are shown in Figure 4.6. Along with Ag loading, the colour of the photocatalysts changed, from pure white of BTO to dark blue of Ag-BTO-10min. The dark blue colour of Ag-decorated BTO was in accordance with the strong broad absorption peak sitting between 500 nm to 600 nm in Figure 4.6. This phenomenon has been reported as the surface plasmon resonance (SPR) [108–110] induced by the noble metal nanoparticles. It has been claimed that the absorption peak arising from surface palsmon resonance depends on the size, shape of the metallic nanoparticle and their size distribution and surroundings[108,109]. A wide size distribution of Ag nanoparticles has been demonstrated to broaden the absorption peak[108,109]. The observed broad absorption peak was indicative of the wide size distribution of Ag nanoparticles in the samples, which consisted with what we observed using TEM.

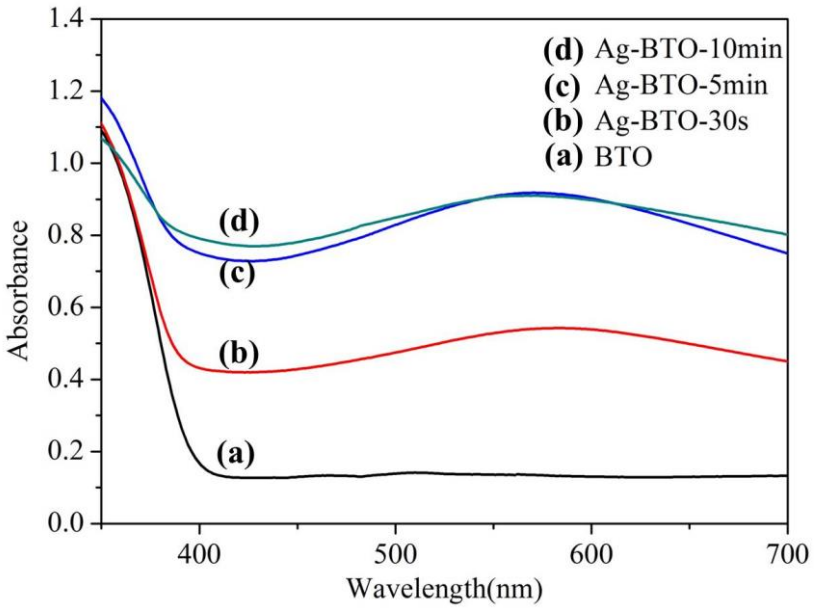

Figure 4.6 Diffuse reflectance spectra of photocatalysts. A broad absorption band in the visible-light range can be seen in the Ag decorated BTO.

In addition, the aborption peak position in this work was found to vary for different photodepositon times, 582 nm for Ag-BTO-30s, 571 nm for Ag-BTO-5min and 567 nm for Ag-BTO-10min. Thus a gradual red-shift was obtained.

It has been reported that the top of the SPR peak shifts to longer wavelength with the increase in the metal nanoparticle size[161,162]. However, the exceptional small shift of absorption peak due to SPR has been previously reported as well [163–165]. In addition, it has also been observed that in the photoreduction of noble metal nanoparticle, this wavelength shows a red-shift in the early stage of irradiation, and then blue-shift gradually later on[162]. The diverse and controversial results on the absorption peak position due to SPR are related to the different synthesis methods and the surroundings where noble metal nanoaprticles exist. The various methods will result in a different-level control on the size and shape of nobel metal nanoparticles, which will impact on the surface plasmon resonance. Overall the presence of Ag nanoparticles increased the visble-

light harvesting of the photocatalysts through surface plasmon resonance, and potentially contribute to the improvement of photocatalytic activity.

4.2 Effect of photodeposition time on photocatalytic activity

The photocatalytic activities of the different photocatalysts were assessed using the decolourisation of Rhodamine B under artificial solar light.

Prior to exposure under solar light, the dye solution with photocatalysts were stirred in dark for 30 mins to enable an equilibrium between adsorption of dye molecules on the surface of photocatalysts and desorption. It has been proposed that the photocatalytic reactions take place on the surface of the photocatalysts, therefore adsorption of reactants on photocatalysts is an important step during the overall photocatalytic process[166].

After comparing the concentration of dye solutions before and after mixing with powered photocatalysts, it was found that the concentration dropped, which is related to the adsorption, i.e. a portion of dye molecules in the solution diffuse into the surface region of the catalysts and are adsorbed onto the surface. The adsorption amount using different photocatalysts was compared. It should be noted that the adsorption quantity is related to the surface area. A large surface area provides more active sites, which normally give a higher adsorption amount. Therefore the adsorption quantity was scaled by surface area to compare the adsorption quantity in the same number of active sites.

For bare BTO, the adsorption percentage was found to be about 0.97% whereas for Ag-BTO-30s, it increased to about 1.64%. The adsorption on the other two Ag modified photocatalyst showed no significant change compared to Ag-BTO-30s. The adsorption quantity obtained above was taken as an average of three experiments. It can be seen that the presence of Ag nanoparticles increased the dye molecules adsorption. This phenomenon has been reported previously for Ag deposited on TiO_2 where the dye

molecule adsorbed more strongly on Ag-TiO_2 than TiO_2[106,107,160]. Pt has also been observed to assist the adsorption of RhB on to TiO_2[167]. The assist of noble metal in adsorption dye molecule was attributed to the possible electronic state change of substrate due to deposition of noble metal nanoparticles on the surface.

The UV-Vis absorption spectra of RhB dye solution after different irradiation time using Ag-BTO-30s is shown in Figure 4.7. The peak of maximum absorption for RhB was located at 554nm, and it can be seen that the light absorption intensity, which is proportional to the concentration of dye, dropped with the irradiation time. This indicated that the photodecolourisation process takes place under the solar light irradiation in the presence of photocatalysts. The sample of zero min represented the sample after adsorption-desorption equilibrium and the absorption intensity at 554 nm was taken as C_0. The absorption intensity of other samples with different irradiation time was C_i. The percentage of photodecolourisation *X* was calculated using Equation (4.7),

$$\mathrm{X}(\%) = \left(1 - \frac{C_i}{C_0}\right) * 100 \qquad (4.7)$$

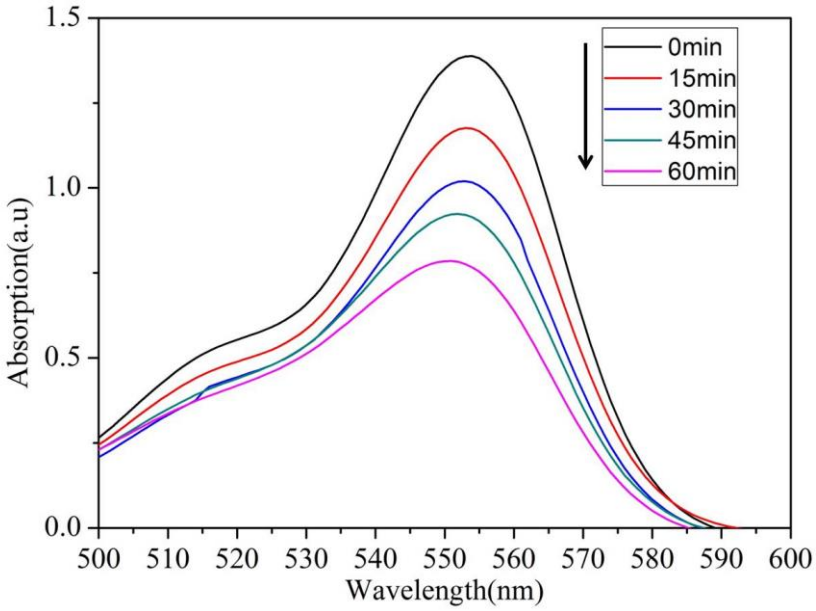

Figure 4.7 UV-Vis absorption spectra of RhB solution at different irradiation time with Ag-BTO-30s. The decrease in the maximum absorption intensity shows the decolourisation process.

The photodecolourisation profiles of Rhodamine B with BTO and Ag-modified BTO are shown in Figure 4.8. It can be found that during solar light irradiation Ag modified $BaTiO_3$ showed an enhancement in dye-decolourisation efficiency. All the data values adopted were calculated as an average of three experiments.

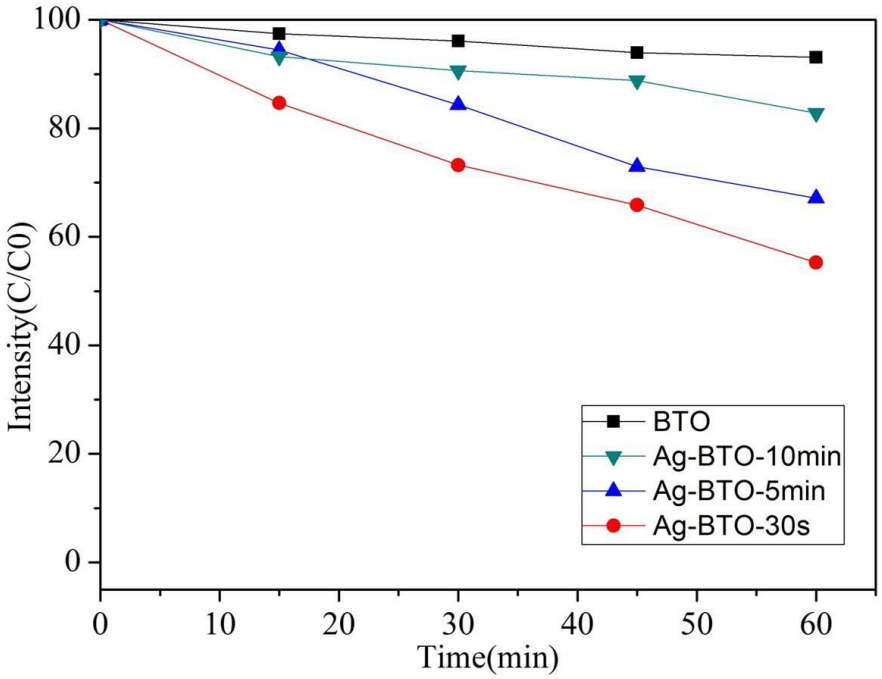

Figure 4.8 Photodecolouriation profiles of RhB with differerent photocatalysts. Ag modified BTO shows higher photocatalytic activity than bare BTO.

Generally, it has been assumed that the kinetics of photocatalytic decolourisation of most organic compounds follows the Langmuir–Hinshelwood model[3,8,168]:

$$r_i = -\frac{dC_i}{dt} = \frac{kKC_i}{1+kKC_i} \tag{4.8}$$

Where C_i is the molar concentration of the dye solution, k is the reaction rate constant and K is the adsorption coefficient of the dye to the catalyst. When C_i is small ($C_i < 10^{-3}$ M)[8], $kKC_i << 1$ and Equation (4.8) will be simplified to a pseudo first order equation:

$$r_i = -\frac{dC_i}{dt} = kKC_i \tag{4.9}$$

Integrating Eq. (4.9) gives the following relationship:

$$\ln(\frac{C_0}{C}) = k_{obs}t \tag{4.10}$$

Where C_0 is absorbance related to the initial concentration of the dye and $k_{obs} = kK$ is the observed pseudo first order reaction rate constant. Thus the reaction rate k_{obs} can be obtained from the slope of $\ln(C_0/C)$ vs. t, shown in Figure 4.9. The parameters of linear fitted plots are listed in Table 4.2.

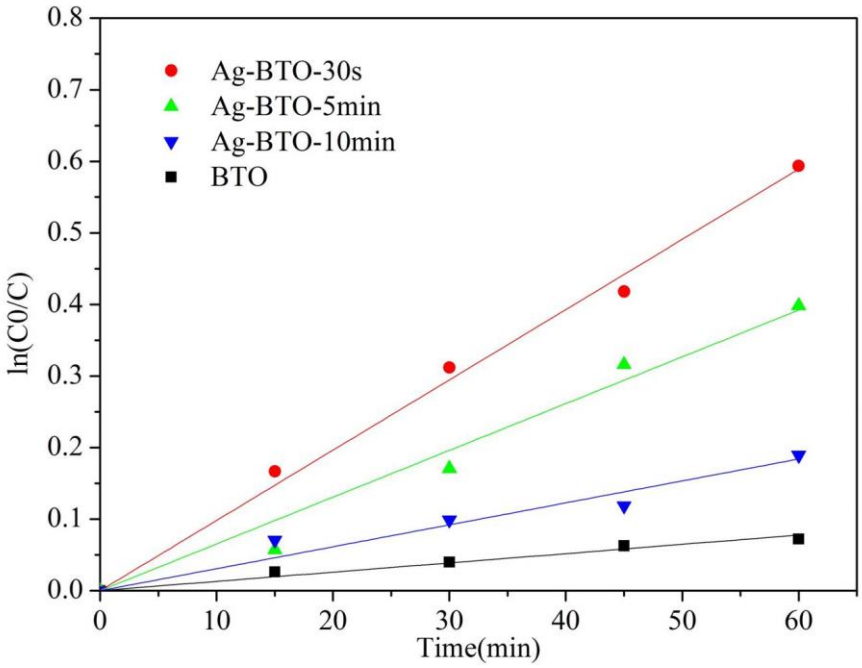

Figure 4.9 Determination of photodecolourisation kinetic rate. The decolourisation rate follows the order: BTO<Ag-BTO-10min<Ag-BTO-5min<Ag-BTO-30s

Table 4.2 The obtained k_{obs} from the fitted linear plot of $\ln(C/C_0)$ vs. t.

Photocatalysts	k_{obs} (min^{-1})	R^2
BTO	0.0013	0.97
Ag-BTO-30s	0.0098	0.99
Ag-BTO-5min	0.0065	0.98
Ag-BTO-10min	0.0031	0.94

Among all the four catalysts, Ag-BTO-30s showed the highest activity while bare BTO showed the slowest decolourisation rate. The reaction rate of Ag-BTO-30s was about 7.5

times that of plain BTO. The improvement of photocatalytic activity after Ag loading was consistent with the widely accepted photocatalytic activity enhancement function of noble metal loading[169]. Ag nanoparticles deposited on the surface can act as electron-traps due to a lower Fermi level of these noble metals. In this way, the electrons generated in BTO under solar irradiation can migrate to Ag nanoparticles on the surface, and then further transferred to the adsorbed O_2 to produce the active species $O_2^{\cdot-}$, involving in the further reactions. The facile transport of electrons from bulk to surface will relatively reduce the chance for electrons and holes to encounter and recombine. Therefore, the overall photocatalytic activity will be prompted. The related reactions can be shown below[106]:

$$e^- + Ag_n \rightarrow Ag_n^- \tag{4.11}$$

$$Ag_n^- + O_2 \rightarrow Ag_n + O_2^{\cdot-} \tag{4.12}$$

In terms of the effect of photodeposition time on the photocatalytic activity, the photocatalytic activity decreased with increase of photodeposition time, as shown in Figure 4.8 and Table 4.2. This is related to the different size and loading mass of Ag nanoparticles in Ag modified BTO with different irradiation time. It has been reported that as the size and mass of noble metal nanoparticles increases, they will act as recombination centres and some of the advantage of Ag deposition will be lost[106], as shown in Equation 4.13.

$$Ag_n^- + h^+ \rightarrow Ag_n \tag{4.13}$$

In addition, excessive Ag nanoparticles loaded on the surface can occupy the reactive sites and hinder the contact of dye molecules and catalysts[170], which will result in the decreasing of photocatalytic efficiency. Therefore, an efficient silver-decorated barium titante should possess a structure with optimum size and mass for silver nanoparticles to maintain the electron-trap role of silver nanoparticles and meanwhile avoid the

deterioration induced by excessive loading. In this study, photodeposition for 30 seconds was demonstrated to result in a most efficient silver-decorated barium titanate among all samples studied.

In order to test the photocatalytic activity of these photocatalysts in decolourisation of dye molecules with different nature, another organic azo dye, Acid Black 1(AB1) was chosen as the target dye. In contrast to Rhodamine B, which is a cationic dye, AB1 molecule will be relased as an anion in the solution. The opposite sign of charge between RhB and AB1 will have a potential impact on the reactions with photocataltysts.

The UV-Vis absorption spectra of Acid Black 1 solution with Ag-BTO-30s under different irradiation time and the comparison of photodecolourisation priofiles between these four photocatalysts are exhibited in Figure 4.10.

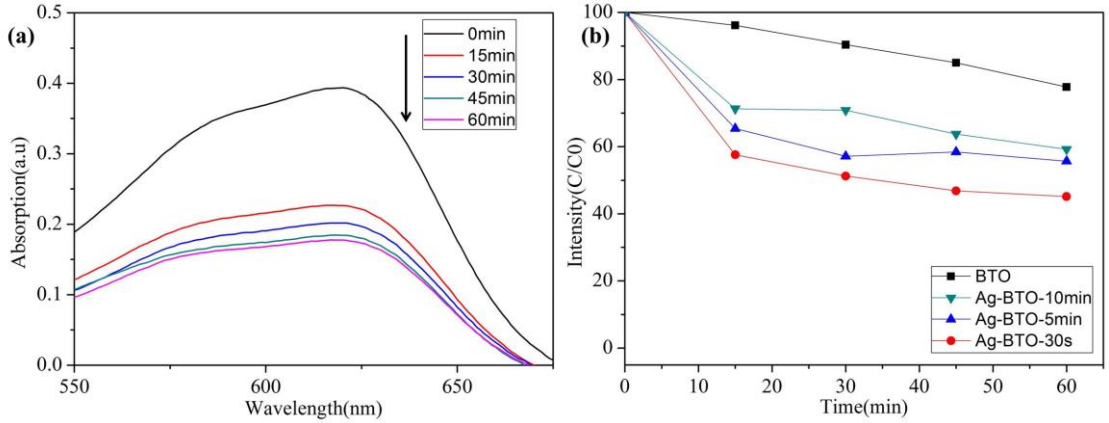

Figure 4.10 (a) UV-Vis absorption spectra of Acid Black 1 using Ag-BTO-30s as photocatalysts under different solar irradiation time, (b) photodecolourisation profiles of AB1 using different photocatalysts.

The charateristic absorption peak of AB1 was at 620 nm, as shown in Figure 4.10(a). A similar tendency was obtained in photodecolourisation of AB1. The photocatalytic activity decreased with the increase of photodepositon time and the best photocatalytic performance was observed in Ag-BTO-30s. Therefore, combining photodecolourisation of RhB and AB1, it can be concluded that Ag-BTO-30s showed the highest photocatalytic

activity in decolourisation organic dye, no matter anionic AB1 or cationic dye RhB. The optimum photodeposition time is 30 seconds and the best photocatalyst Ag-BTO-30s was chosen to intestigate the effect of pH on photocatalytic activity.

4.3 Effect of pH on photocatalytic activity

The effect of pH of the initial dye solution on photocalalytic acitivity was investigated. The pH of Rhodamine B solution was adjusted by 0.1M HCl or 0.1M NaOH to obtain different pH ranging from 2 to 11 and Ag-BTO-30s was used as the photocatalyst.

The first role of pH playing in impacting the photodecolourisation of organic dyes is affecting the dye adsorption through modificating the electric double layer of solid-liquid interface, altering the net surface charge of the photocatalysts and affecting the electrostatic interactions[3,90]. The adsorption amounts of RhB on the photocatalysts under different pH conditions are presented in Figure 4.11. The removal percentage of RhB after 30mins under dark conditions increased with increasing pH value of the initial dye solutions.

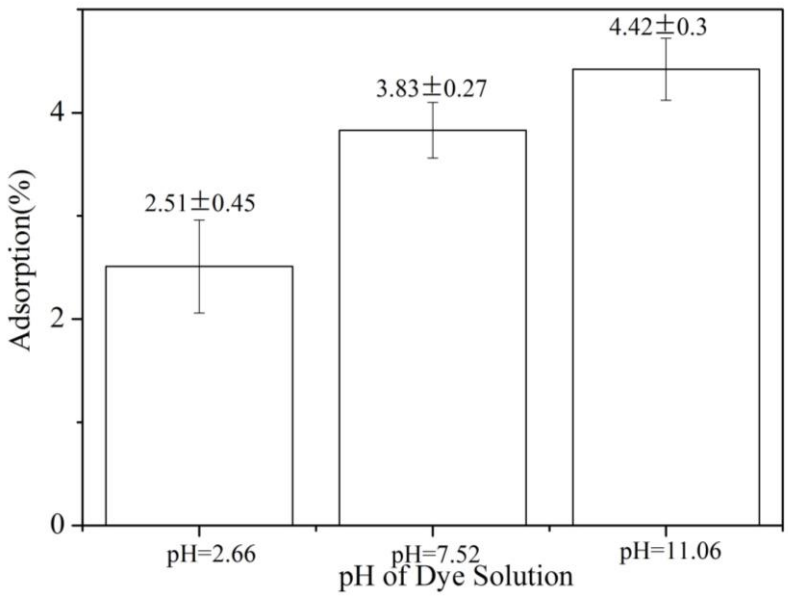

Figure 4.11 RhB adsorption under different pH conditions. Under the conditions of high pH, more RhB molecules were adsorbed on the photocatalyst (Ag-BTO-30s) than under low pH conditions.

This phenomenon can be explained from the view of electrostatic interactions between the photocatalysts and dye molecules. The zeta potential of Ag-BTO-30s was measured, as shown in Figure 4.12. As shown, the isoelectric point of Ag-BTO-30s was at pH=3.1. Therefore, it was considered that the photocatalysts possess a net positive surface charge under the acid conditions (here pH=2.66). The Coulombic repulsive force between the positively-charged photocatalyst and the positive RhB ion will result in a smaller amount of adsorption. When under the basic or neutral conditions, the photocatalysts will exhibit in a net negative charge, which is of opposite sign of cationic RhB molecules. Then the electrostatic attractions will lead to an increase in the dye adsorption compared with that of acid conditions. The similar experimental phenomenons of dye adsorption were reported by other researchers[171–173].

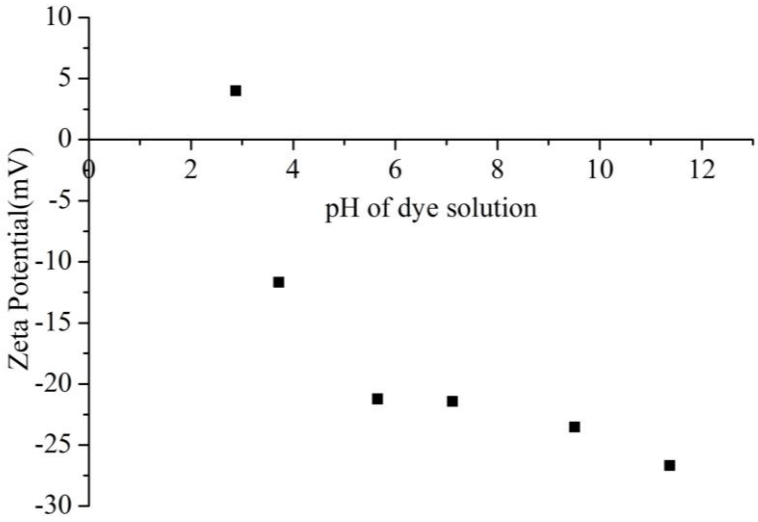

Figure 4.12 Zeta potential of Ag-BTO-30s. The isoelectric point was found to be at pH=3.1.

The comparison of photodecolourisation of RhB under different pH conditions are presented in Figure 4.13. As seen the photocatalyst showed a much higher activity in acid condition than the netural or basic conditions, and about 90% of the dye molecules were removed in 60 minutes. When the initial pH of the solution was high, i.e. alkaline conditions, the photocatalytic activity deteriorated and the decolourisation percentage was only 20% during the overall process.

Comparing the adsoption (Figure 4.11) and photodecolourisation profiles (Figure 4.13) under different pH conditions, it was found that the tendency of the photodecolourisation rate was opposite to the trend of adsorption under different pH conditions. The basic conditions gave the maxium adsorption of RhB but the slowest photodecolourisation rate while the acid conditions showed the best photocatalytic performance although the dye adsorption was minimum.

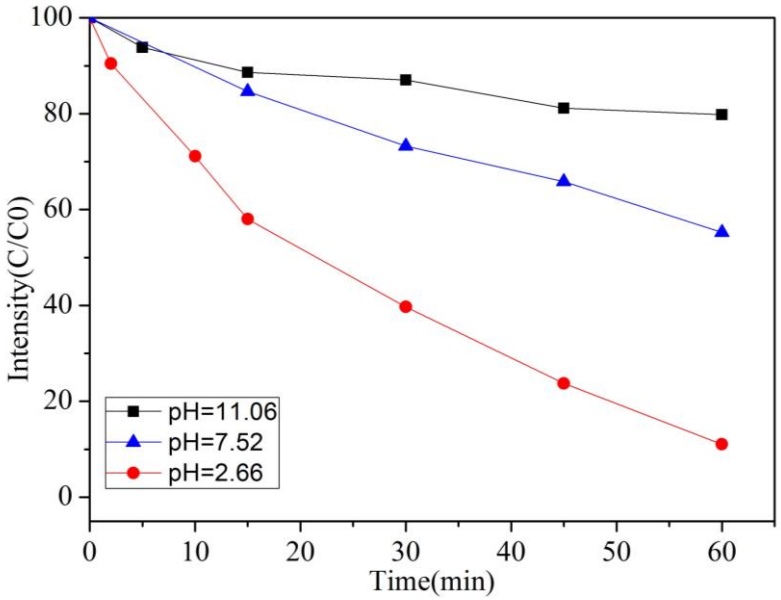

Figure 4.13 Photodecolourisation of RhB with Ag-BTO-30s under different pH conditions. The photocatalytic activity was highest under acid condition and lowest under basic condition.

The adsorption of reactants onto the photoexcited photocatalysts is an important step during photocatalytic reactions[8,174]. The photocatalytic reactions take place on the surface of photocatalysts, and therefore the adsorption of dye molecules have impact on the overall photocatalytic efficiency. However, adsorption is not the only factor influencing photodecolourisation , and some other factors affect the process as well, e.g. the generation of reactive species. The discrepancy between adsoption and overall photodecolourisation rate under different pH conditions indicated that adsorption was not the rate-determining factor in this experiment. The similar phenomenon has been reported that the maximum of photocatalytic efficiency did not occur in the condition of pH wherein the maximum adsorption occurs[175,176].

The effect of pH on the photocatalytic degradation activity has been studied in different photocatalytic systems and the interpration of its effect was controversial due to its multiple roles in addition to the adsorption effect discussed above[3,177]. Firstly, the generation of active oxidative radicals, hydroxyl radicals $OH^{\cdot}$, which is widely accepted as an active oxidative species in dye decolourisation, can be impacted under different pH

conditions. It was stated that $OH^{\cdot}$ can be formed easier in alkaline conditions due to more hydroxyl ions available to have reactions with photogenerated holes[178], as shown in Equation 4.14 and 4.15.

$$h_{VB}^{+} + OH^{-} \rightarrow OH^{\cdot} \quad (4.14)$$

$$\text{Dye} + OH^{\cdot} \rightarrow Degradation\ products \quad (4.15)$$

However, it should be noted that due to the negative surface charge of photocatalyts under high pH, the coulombic repulsive force between photocatalysts and hydroxyl anions will make the formation of $OH^{\cdot}$ difficult, and then decrease the photooxidation process.

In addition, it was proposed that during the photodegradation process, some produced negative species (e.g. intermediates species) can compete with hydroxyl ions for occupancy the active sites on the surface of photocatalysts. This will decrease the possibility of adsorption of OH^{-} and then formation of $OH^{\cdot}$[171,179].

The different roles of high pH will compete with each other. When the negative effect due to high pH overcomes the positive effect, the photocatalytic performance will be worse, which explains the lowest decolourisation rate obtained at high pH in this work.

Apart from the generation pathway through reactions between holes and OH^{-}, $OH^{\cdot}$ can be produced through other pathways, especially under acid conditions, as indicated in Equation 4.16-4.19[3,180].

$$e_{CB}^{-} + O_2 \rightarrow O_2^{-\cdot} \quad (4.16)$$

$$O_2^{-\cdot} + H^{+} \leftrightarrow HO_2^{\cdot} \quad (4.17)$$

$$2HO_2^{\cdot} \rightarrow H_2O_2 + O_2 \quad (4.18)$$

$$H_2O_2 + e_{CB}^- \rightarrow OH^- + OH^{\cdot} \quad (4.19)$$

These reactive species $O_2^{-\cdot}$, $HO_2^{\cdot}$ and $OH^{\cdot}$ also play important roles in the reactions with dye molecules. The various active species generated through Equation 4.16-4.19 in acid conditions gave rise to the observed high photodecolourisation rate when the pH of initial dye solution was low.

Overall, the effect of pH on the photocatalytic decolourisation efficiency varies between different systems and different nature of target pollutants. When it comes to the further industrial application, it is important to study the specific mechanisms, the nature of target pollutants to be degraded, and to find the proper pH to get the optimum photocatalytic efficiency.

4.4 Detection of reactive species during photodecolourisation process

In order to further understand the reaction mechanisms of photodecolourisation of Rhodamine B using Ag modified BTO under solar irradiation, a radical scavenger was added to detect the reactive species. Here we chose Ag-BTO-30s as the photocatalyst, which showed the best photocatalytic activity in decolourisation of RhB, and the pH of initial dye solution was not adjusted and controlled during the whole process.

Alcohols such as ethanol are regarded as hydroxyl radical scavengers and used widely in the photocatalytic research[181–183]. It was reported that the rate constant of reactions between hydroxyl radicals and ethanol was 1.9×10^9 $M^{-1}s^{-1}$, and this reaction will result in a quick quench of hydroxyl radicals[184]. Therefore, ethanol was chosen and added into the dye solution to investigate the role of hydroxyl radicals in the overall photodecolourisation process. The comparison of the obtained photodecolourisation profiles between without ethanol and with ethanol is shown in Figure 4.14.

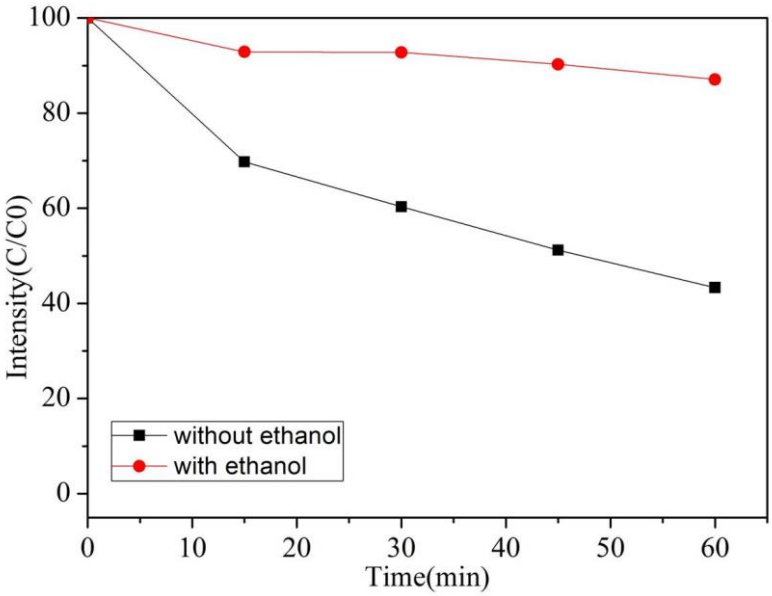

Figure 4.14 Comparison of photodecolourisation profiles between with and without ethanol using Ag-BTO-30s as photocatalyst. The addition of hydroxyl scavenger ethanol inhibited the photodecolourisation process to some extent.

It can be observed that in the presence of ethanol, the photodecolourisation rate decreased compared with that without ethanol. Only about 10% of RhB dye was photocatalytically removed in 60 mins when ethanol was added while it was nearly 6 times higher in the absence of ethanol.

Considering the role of hydroxyl radical scavenger of ethanol, it was believed that the inhibition of photocatalytic reactions was related to the quench of hydroxyl radical by ethanol. Then it can be speculated that hydroxyl radicals $OH^{\cdot}$ plays an important role in the photodecolourisation process under experimental conditions.

Furthermore, it should be noted that in the presence of large volumes of ethanol (20% volume percentage), the photodecolourisation was not completely prohibited and there was still 10% photodecolourisation of RhB. This indicated that there were some other reactive species to decolourise the dye in addition to hydroxyl radicals. These species could be the photoexcited electrons/holes and/or $O_2^{-\cdot}$ and/or $HO_2^{\cdot}$ (Equation 4.16-4.19).

4.5 Summary

In this chapter, Ag nanoparticles were photodeposited on the surface of as-received BTO successfully based on the results of XRD, SEM/EDX, TEM/EDX and XPS. The effect of photodeposition time on photocatalytic efficiency was investigated. It was found that the silver loading mass and size of Ag nanoparticles increased with the increase of photodeposition time. Among all the photodeposition times studied, photodeposition of 30 seconds gave the best photocatalytic activity in photodecolourisation of both cationic dye RhB and anionic AB 1. The enhancement of photocatalytic activity after Ag decoration was attributed to the electron-trapping role of noble Ag nanoparticles and the surface plasmon resonance. However, this improvement will deteriorate along with the increasing of Ag mass and nanoparticle size. This phenomenon was related to the role of large Ag nanoparticles as recombination centre of charge carriers and/or more active site of photocatalyst being blocked by Ag nanoparticles. Therefore, photodeposition for 30 seconds was chosen as the optimum time for further study.

The effect of pH of initial RhB dye solution on photodecolourisation efficiency using Ag-BTO-30s as photocatalyst was studied. More dye molecules were adsorbed under high pH condition due to the electrostatic attraction between the negatively surface-charged the photocatalyst and the positively charged cationic dye ions. However, the photocatalyst showed the highest photodecolourisation rate when the pH value was low, i.e. acid condition. The photocatalytic activity was worst in alkaline conditions. This phenomen was due to the multiple roles of pH, including modifying the surface charge properties of photocatalysts, generation of various reactive radicals. Furthermore, the active species during photodecolourisation of RhB using Ag-BTO-30s as photocatalyst under neutral conditons were preliminarily detected by addition of hydroxyl radical

scavenger –ethanol. The inhibition of photodecolourisation to some extent indicated that hydroxyl radicals were the main reactive species but not the only one.

Chapter 5

Effect of ferroelectricity on solar-light-driven photocatalytic activity of $BaTiO_3$

As reviewed in section 2.5, $BaTiO_3$ can exist in both nonferroelectric cubic phase and ferroelectric tetragonal phase at room temperature. In order to investigate the effect of ferroelectricity of $BaTiO_3$ on its photocatalytic activity under solar light, a simple thermal treatment was carried out on the as-received $BaTiO_3$ to modify its phase composition and alter its ferroelectricity, and the obtained BTO named as BTO-anneal. In this chapter, BTO and BTO-anneal was modified with Ag nanoparticles using the photodeposition method, and the photodeposition time was set as 30 seconds based on the optimum photodepositon time obtained in section 4.1. The Ag decorated BTO and BTO-anneal powder were named as Ag-BTO and Ag-BTO-anneal for simplify. A schematic showing the detailed process is presented in Figure 5.1.

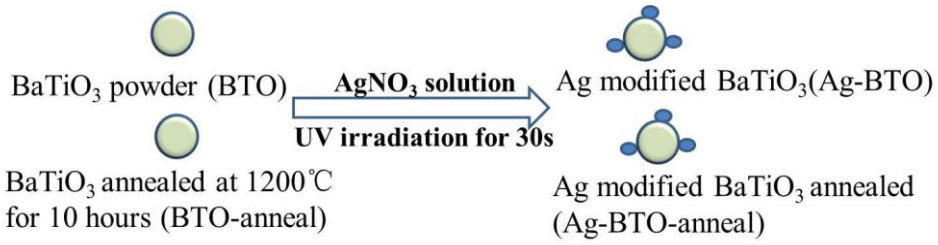

Figure 5.1 Schematic showing the preparing process of four different photocatalysts

Then the photocatalytic activity of these four photocatalysts, i.e. BTO, BTO-anneal, Ag-BTO and Ag-BTO-anneal were studied systematically through photodecolourisation of organic dyes under simulated solar light. The effect of ferroelectricity was discussed on the Stern layer formation and charge carriers separation.

5.1 Characterisation of $BaTiO_3$ powder and Ag-modified $BaTiO_3$

The SEM micrographs of the different catalysts are shown in Figure 5.2. The mean particle size obtained by taking an average of 100 particles from SEM images is shown

in Table 5.1, with the corresponding surface areas measured by BET. In the case of the annealed samples the particle size was given after post-anneal grinding. It can be seen that after annealing, the particle size increased and the surface area decreased accordingly. In addition, the powders before annealing showed a wider size distribution compared with that of post-annealing, as indicated in Figure 5.3. It is known that particle size and surface area of catalysts have a significant impact on the catalytic efficiency of a system[185]; when all other conditions are equal it is anticipated that a smaller particle size and higher surface area will lead to better catalytic performance.

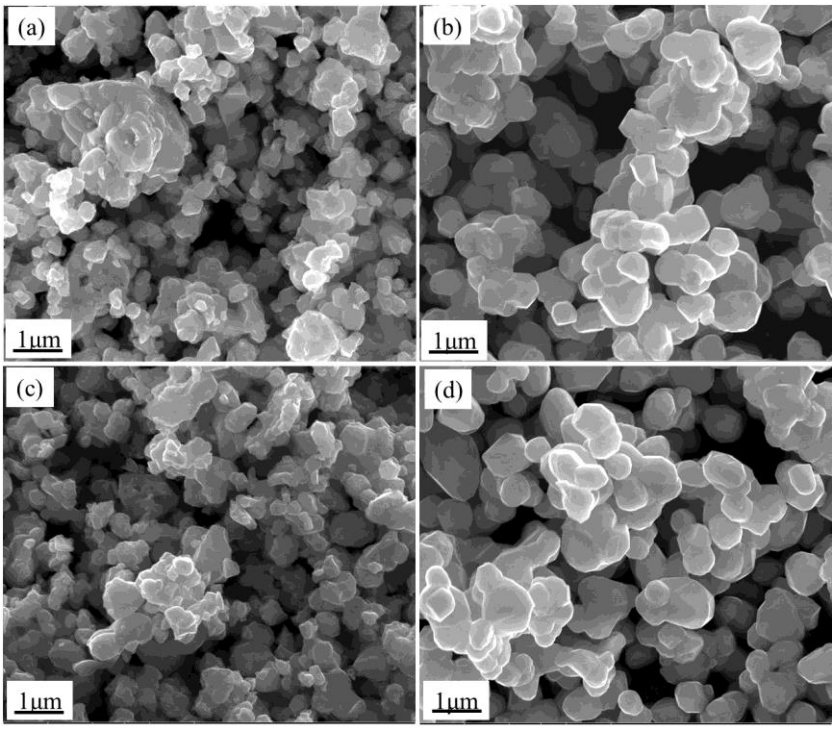

Figure 5.2 SEM micrographs of (a) BTO, (b) BTO-anneal, (c) Ag-BTO and (d) Ag-BTO-anneal, showing the particles grow bigger and agglomerate after annealing. Ag is not visible on the surface of the particles in (c) or (d).

Table 5.1 Particle size and surface area of $BaTiO_3$ and Ag modified $BaTiO_3$

Sample	Average Particle Size(nm, SEM)	BET Surface Area(m^2/g)
BTO	386.3	2.055
BTO-anneal	622.2	0.862
Ag-BTO	416.8	2.335
Ag-BTO-anneal	673.3	0.611

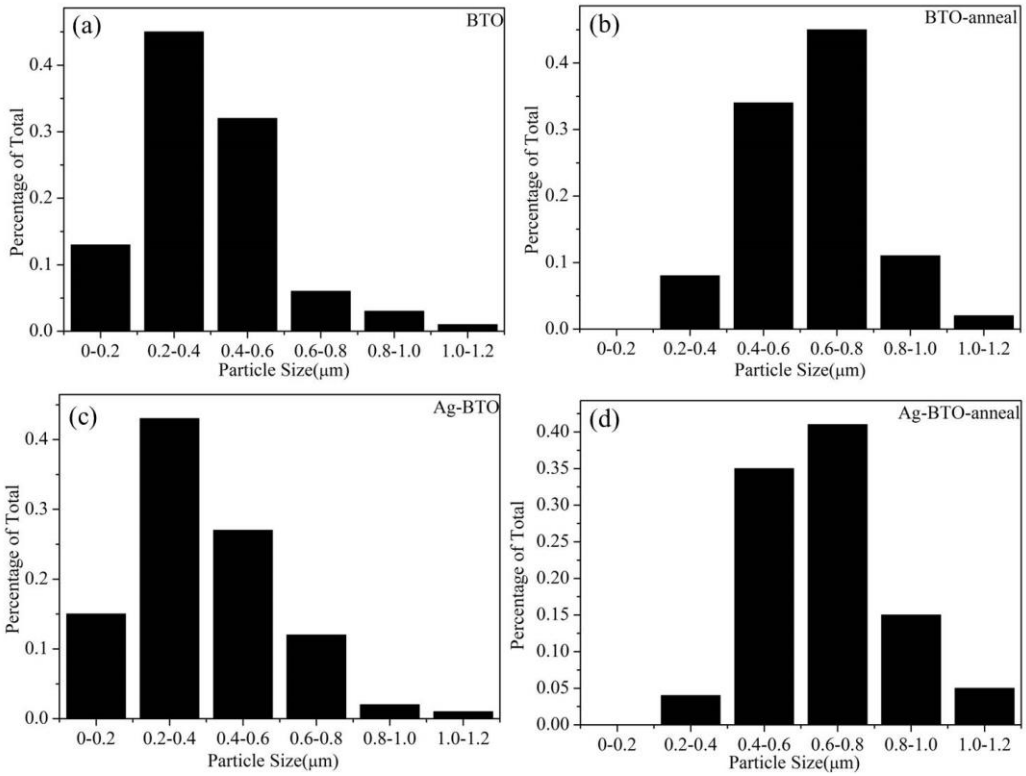

Figure 5.3 Size distribution of powders used, (a) BTO (b) BTO-anneal (c) Ag-BTO and (d) Ag-BTO-anneal. After annealing, powders show a narrower size distribution and larger mean particles size than before annealing, which is consistent with that observed in Figure 5.2.

The phase composition of the powders was analysed using XRD. Wide 5-70° 2θ patterns obtained for each of the samples are shown in Figure 5.4. There was no observable difference in the XRD patterns after silver deposition and no peaks assigned to Ag were detected in any of the XRD patterns. We believe this is due to the small amount of silver

that has been deposited on the surface of $BaTiO_3$, which is discussed further below with respect to the TEM results.

The XRD pattern of pure cubic $BaTiO_3$ (c-$BaTiO_3$) showed a single peak at $2\theta = 45°$ (JCPDS 31 0174) which was assigned to the (200) lattice plane. In the pattern for tetragonal $BaTiO_3$ (t-$BaTiO_3$) this peak was split into two at $2\theta = 44.8°$ for (002) and $2\theta = 45.4°$ for (200) (JCPDS 05 0626). The patterns for BTO and Ag-BTO (Figure 5.4 (a) and (b)) seemed to have a single peak around $2\theta = 45°$ with a slight shoulder indicating there may be some splitting. The splitting can be more clearly seen for BTO-anneal and Ag-BTO-anneal (Figure 5.4(c) and (d)), implying a higher tetragonal content for these samples.

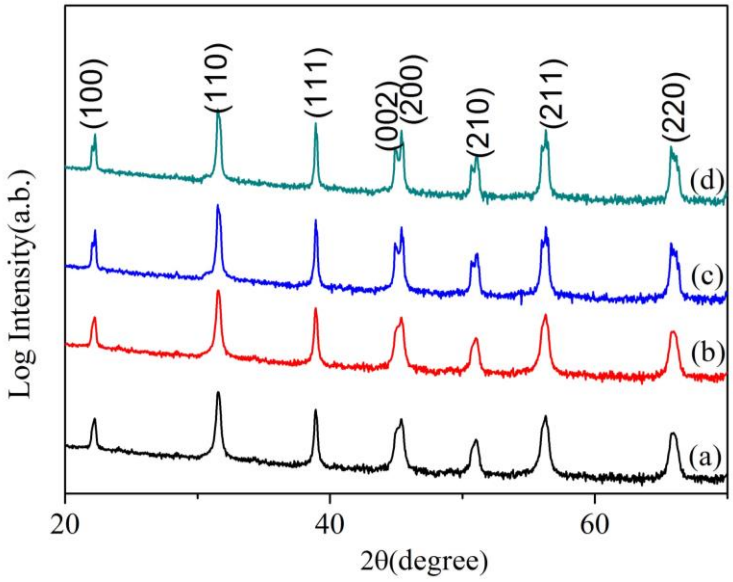

Figure 5.4 XRD pattern of (a) BTO, (b) Ag-BTO, (c) BTO-anneal, (d) Ag-BTO-anneal. No silver peak was detected in these samples. After annealing, the peak around 45 °shows splitting more distinctly, illustrating more tetragonal phases produced.

In order to investigate the phase of these materials, high-resolution XRD analysis of the region around $2\theta = 45°$ was performed. Peaks were fitted to these data using the reference spectra for cubic and tetragonal $BaTiO_3$. Contributions from both Cu Kα1 ($\lambda = 1.5405$ Å)

and Kα2 (λ = 1.5443 Å) radiation were included, as they could be resolved in these scans, which give two reflections per lattice plane.

X-ray diffraction angles were calculated from Bragg's law using the wavelength of the incident Cu Kα1 and Kα2 radiation (λ = 1.5405 Å and 1.5443 Å respectively) and the known lattice spacings of the cubic (200) plane and tetragonal (002) and (200) planes, giving six peaks in total. Basic broadening was accounted for by using Gaussian-type peaks. The fit was optimized by minimizing the difference between the data and the sum of the peaks by varying the peak width and height, while keeping the relative intensities of the tetragonal (002) and (200) peaks and the Cu Kα1 and Kα2 peaks constant based on the powder pattern and relative emission intensities respectively. Proportions of cubic and tetragonal phase were calculated based on the ratio of peak area compared to the relative intensities in the reference spectra. Hence six peaks are included in total from the tetragonal and cubic planes, as shown in Figure 5.5. The cubic peaks were much broader than the tetragonal, indicating a small crystallite size for the cubic material: the Scherrer formula gives a lower limit of 25-50 nm for the cubic crystallites in both samples. This indicates that the grains seen in Figure 5.2 may be agglomerations of smaller crystallites, and supports the evidence from the literature that the cubic phase occurs at room temperature in $BaTiO_3$ in small (<100-200 nm) crystals[42].

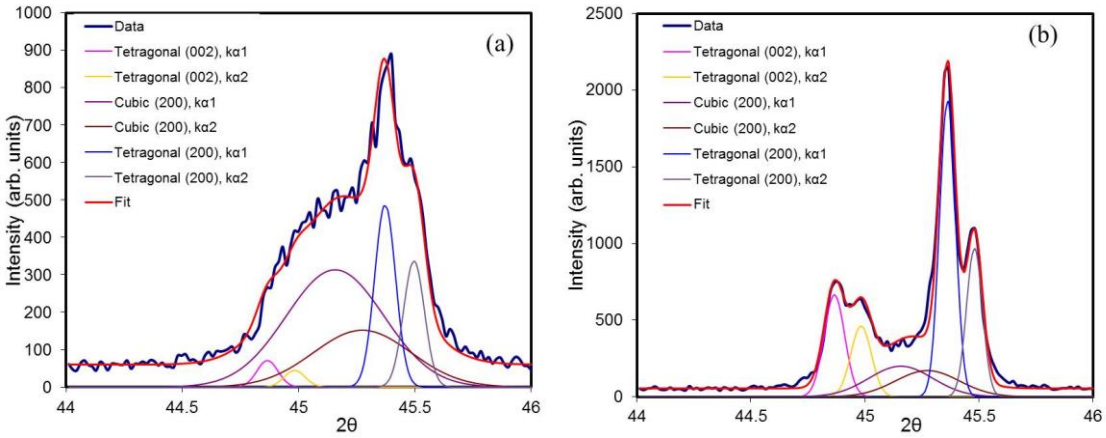

Figure 5.5 XRD fitting curves for (a) BTO and (b) BTO-anneal. The peak splitting into two was distinct in BTO-anneal. Based on the fitting results, proportions of cubic and tetragonal phase were calculated according to the ratio of peak area compared to the relative intensities in the reference spectra. BTO-anneal presents a peak pattern contributed from more tetragonal phases than BTO.

Comparison of the areas of the peaks relative to the intensities of the reference spectra in Figure 5.5 showed that BTO contained 92 % cubic material, which was reduced to 67 % in BTO-anneal, indicating that using a simple thermal anneal is successful in converting a large portion of $BaTiO_3$ from cubic to tetragonal. During the annealing process for 10 hours, the particles grow and agglomerate through atomic diffusion while grain boundaries decrease (See Figure 5.2). Accordingly, the room-temperature stabilisation of the cubic structure due to small particle size is reduced, and thus a larger portion of the catalyst is tetragonal at room temperature after sintering. As $BaTiO_3$ is ferroelectric when tetragonal, but not when cubic[146,186], this indicates that BTO-anneal will have a higher ferroelectric content, where BTO is almost entirely cubic and therefore non-ferroelectric. Thus by comparing the behaviour of these two samples the influence of ferroelectricity on the catalytic properties can be investigated. Although BTO-anneal still has a high proportion of cubic content, further annealing would lead to significant reduction in the surface area through sintering which would prevent comparison with the unannealed catalysts.

The microstructures of $BaTiO_3$ and Ag-modified $BaTiO_3$ were investigated by TEM (Figure 5.6). The TEM showed that the samples that have undergone thermal treatment consist of large agglomerated grains of material (Figure 5.6(b) and (d)). For samples that have been illuminated in $AgNO_3$ solution there were a series of small particles attached to the edges of the larger supporting $BaTiO_3$ particles which were smaller than 5 nm for Ag-BTO, and 5-10 nm for Ag-BTO-anneal (Figure 5.6(c) and (d)). These nanoparticles have been identified as Ag by EDX analysis (Figure 5.6(d) inset). The small size and low density of coverage of the Ag nanoparticles indicated why they were not detected with standard SEM or XRD analysis as they are too small to be resolved by the SEM, and there was insufficient mass of material to be detected by XRD.

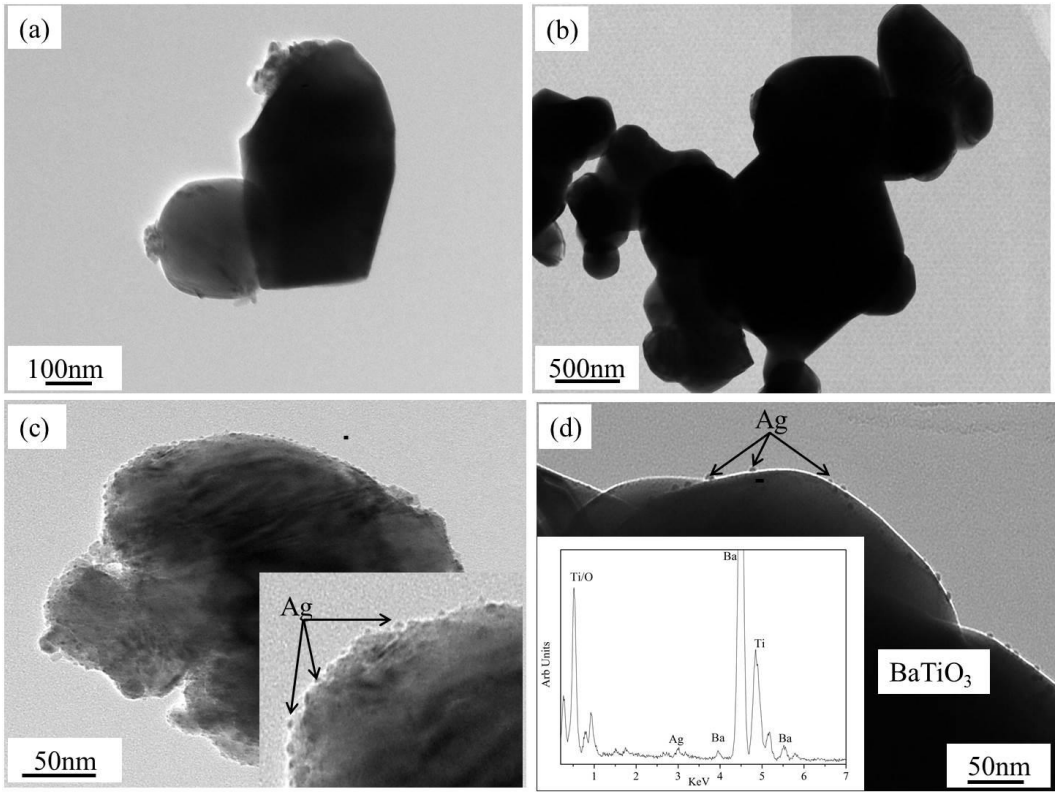

Figure 5.6 TEM micrographs of (a) BTO, (b) BTO-anneal, (c) Ag-BTO and (d) Ag-BTO-anneal, with the corresponding EDX spectrum of (d) inset. Dark dots on the edge of particles in combination with EDX analysis show the success in photodeposition of Ag.

It has been demonstrated that photochemical reactions on the surface of $BaTiO_3$ will be

driven by the ferroelectric domains underlying in the ferroelectrics, leading to spatial separation[61,62], while there is no such domain driven reactivity in non-ferroelectrics,(e.g. TiO_2[107]). There does appear to be some differences between the Ag deposition on annealed $BaTiO_3$ compared to unannealed, with the Ag particles smaller and more evenly distributed on the latter (Figure 5.6). However, it cannot be confirmed that this is linked to selective deposition on ferroelectric domains as we were unable to measure the domain patterns on individual $BaTiO_3$ particles.

XPS was used to confirm the presence and chemical state of any photo-deposited Ag on the surface of the $BaTiO_3$ catalyst support. In the case of the Ag-BTO-anneal (see Figure 5.7) we showed that the spectrum of Ag 3d was made up of two characteristic peaks, Ag 3d3/2 at 373.49 eV and Ag 3d5/2 at 367.49 eV. The spin-orbit splitting of the 3d doublet is 6.0 eV[120,160]. This spectrum was entirely consistent with the XPS spectrum obtained for metallic Ag. This confirmed that silver was present on the surface as detected by EDX analysis, and confirmed that it was in the metallic form.

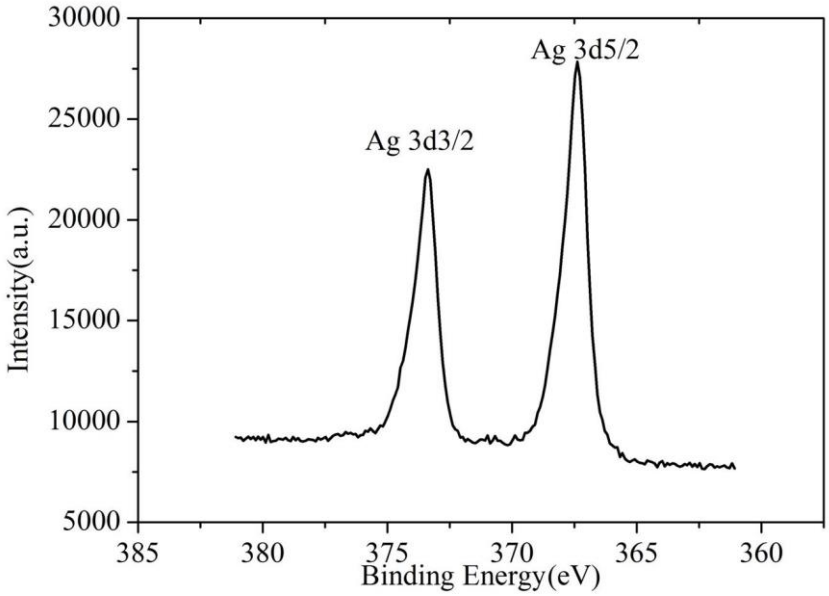

Figure 5.7 XPS spectrum of Ag-BTO-anneal. The characteristic spectrum of Ag3d confirms the existence of metallic Ag.

5.2 Adsorption of Rhodamine B molecules on the catalysts

Adsorption of a dye molecule onto the surface of a catalyst is an important step in the decolourisation process[168]. Prior to exposure under the solar simulator, the dye solutions with catalysts were stirred in the dark for 30 minutes to enable a stable equilibrium situation to develop. The amount of dye adsorbed by the catalyst in the dark was determined using the UV/Vis absorption of the dye solution. The adsorption results, shown in Figure 5.8, highlighted two trends. The first was the enhancement in adsorption of RhB after the $BaTiO_3$ has been annealed. A direct comparison of the dye removal for BTO and BTO-anneal showed that there was an increase from 0.97% (removal) per unit area for BTO to 4.81% (removal) per unit area for BTO-anneal. This indicated that there was a strong influence on the Stern layer generation due to the ferroelectric nature of the BTO-anneal sample[35,37]. In this model the polar RhB cations is likely to produce a tightly bound layer on the polar surfaces of the ferroelectric material that results in a greater degree of dye molecules being bound to the catalyst surface.

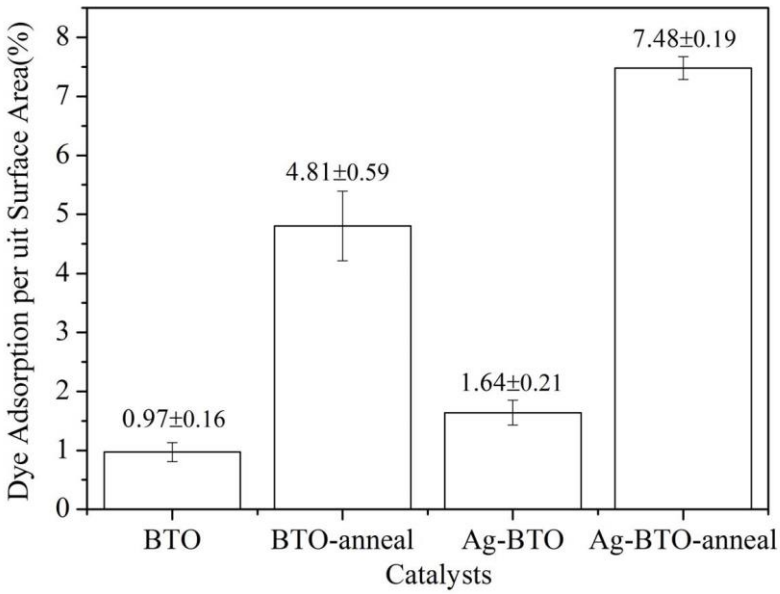

Figure 5.8 Adsorption of RhB by $BaTiO_3$ and Ag-modified $BaTiO_3$ under dark conditions for 30 minutes. Dye removal is scaled for surface area. The adsorption increase dramatically after annealing.

The difference between ferroelectrics and non-ferroelectrics in adsorption of molecules is related to the spontaneous polarisation which can be screened externally by the adsorption of charges species, such as dye molecules. It has been reported by Zhao *et al.*[69] that polarised $BaTiO_3$ adsorbed more ethanol on C+ and C- surfaces than the unpoled surface. The stronger adsorption of dye molecules in ferroelectrics has also been observed in $LiNbO_3$[133], where TiO_2 powder adsorbed 1.27% per unit area while ferroelectric $LiNbO_3$ adsorbed 7.79% per unit area. This demonstrates that the polar nature of ferroelectrics can support a higher loading of dye molecules. This accounts for the higher dye-loading on the BTO-anneal sample, which was shown to have a higher tetragonal, and therefore ferroelectric, phase content by XRD analysis (Figure 5.4 and Figure 5.5).

The second trend is that the adsorption was enhanced by Ag nanoparticle coating on the surface of the catalyst supported by a factor of approximately 1.5 for both BTO and BTO-anneal. This is in consistence with the observation in Chapter 4. The similar phenomenon has been reported previously for Ag deposited on TiO_2 where the dye molecule adsorbed more strongly on Ag-TiO_2 than TiO_2[106,107,160]. The noble metal Pt has also been observed to assist the adsorption of RhB on to TiO_2[167]. The assistance of noble metals in adsorption dye molecule may be attributed to the possible electronic state change of substrate due to deposition of noble metal nanoparticles on the surface.

5.3 Photocatalytic decolourisation of organic dye molecules

The photocatalytic activities of the four $BaTiO_3$ samples were assessed through decolourisation of RhB, shown in Figure 5.9. All the data points were taken as an average of three parallel experiments. The photodecolourisation rate increased in the following order: BTO (slowest) <BTO-anneal<Ag-BTO< Ag-BTO-anneal (fastest).

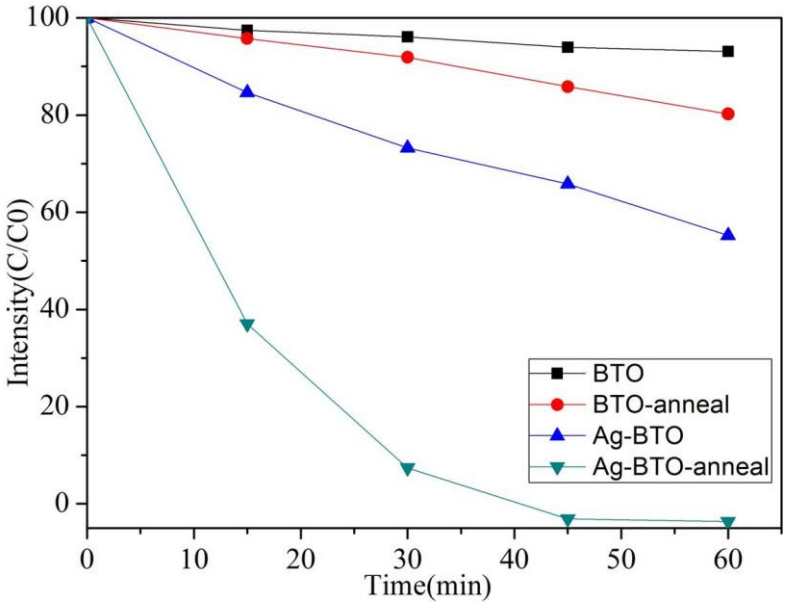

Figure 5.9 Photodecolourisation profiles of RhB with different catalysts under solar simulator. The catalysts consisting of higher t-$BaTiO_3$ after annealing show higher activity, especially when modified by Ag

The reaction rate can be obtained from the slope of $ln(C_0/C)$ vs. t (Equation 4.3), and the linear relationship between $ln(C_0/C)$ and t is shown in Figure 5.10.

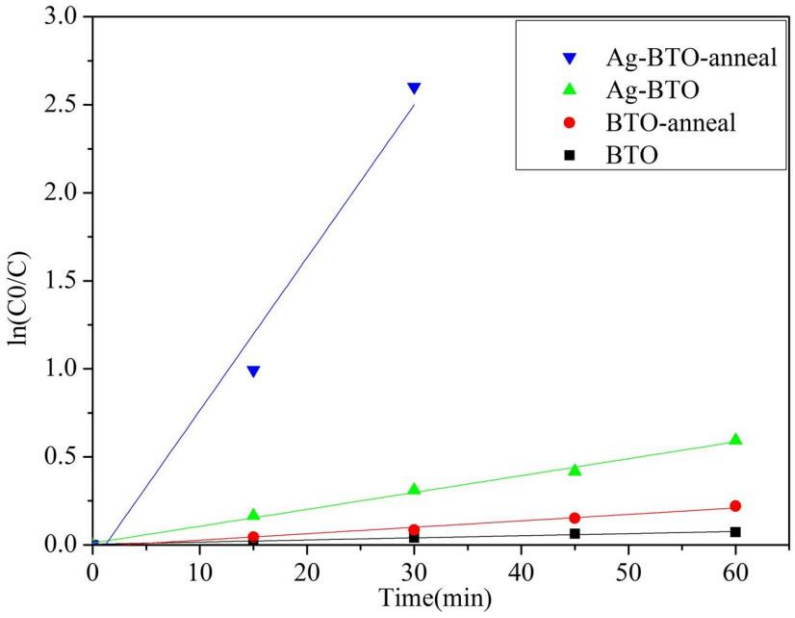

Figure 5.10 Determination of the pseudo-first-order kinetic rate, . For Ag-BTO-anneal, only the first three points are taken for linear fitting due to zero values in absorption at 45mins and 65mins.

The calculated results are shown in Table 5.2. Here the concentration of the dye solution was determined according to the absorption measurement at λ_{max} using spectrophotometer based on the Lambert-Beer law, where the absorbance is proportional to the concentration.

Table 5.2 The obtained k_{obs} from the fitted linear plot of ln(C/C0) vs. t.

Dye solution concentration and volume	Catalyst	k_{obs} (min^{-1})	R^2
10 mg/l, 50 ml	BTO, 0.15 g	0.0012	0.97
10 mg/l, 50 ml	BTO-anneal, 0.15 g	0.0036	0.98
10 mg/l, 50 ml	Ag-BTO, 0.15g	0.0096	0.99
10 mg/l, 50 ml	Ag-BTO-anneal, 0.15 g	0.087	0.96

There were two main effects that can be observed by comparing the rate constants for the four catalysts. The first was that the annealed samples showed higher catalytic activity than the equivalent non-annealed samples despite the annealed samples having a smaller surface area (Table 5.1). This suggested that the increased ferroelectric nature of the annealed samples enhanced catalytic performance. As discussed above a ferroelectric material can effectively separates holes and electrons due to the internal electric field associated with the asymmetry in crystal lattice. This electric field generates a space charge layer similar to that found in a typical p-n junction and acts to separate photogenerated carriers. In addition, as discussed in section 5.2, the annealed catalysts demonstrate much higher levels of dye adsorption, which can also be ascribed to their ferroelectric nature. As indicated by Equation 4.2, and demonstrated previously[168,187,188], higher levels of dye adsorption of the catalyst will enhance the rate of degradation.

In the work presented here the X-ray, TEM and SEM studies give no indication that there are any significant changes to the surface of the $BaTiO_3$ before and after annealing. This is further supported by XPS analysis of the $BaTiO_3$ before and after annealing, as indicated in Figure 5.11. It can be seen that the spectra of these three constitute elements between BTO and BTO-anneal overlap very well, The hydroxyl oxygen (OH) arising from the normal atmosphere and oxide species (O^{2-}) both contribute to the O 1s peak in BTO-anneal (d)[189]. Overall, the XPS spectra of samples post-anneal was pretty similar with that of pre-anneal, showing no significant surface chemical state change. This indicated there should be no changes in the surface chemistry.

It should also be considered that the annealed samples contain a mixture of phases, and polymorphic phase boundaries in catalysts such as TiO_2[190] and Ga_2O_3[191] have been shown to increase photocatalytic activity. However, band offsets exist between phases in these two materials, which is not the case for $BaTiO_3$; it has been found that the phase transition between cubic and tetragonal does not change significantly either the band gap or the band position with respect to the Fermi level[192]. Thus this effect is not expected to influence the activity of the phase-mixed $BaTiO_3$ reported herein. Therefore, it can be concluded that the differences in reaction rate seen in the BTO and BTO-anneal stem from the interaction of the ferroelectric nature with both photoexcited carriers and the dye molecules in solution.

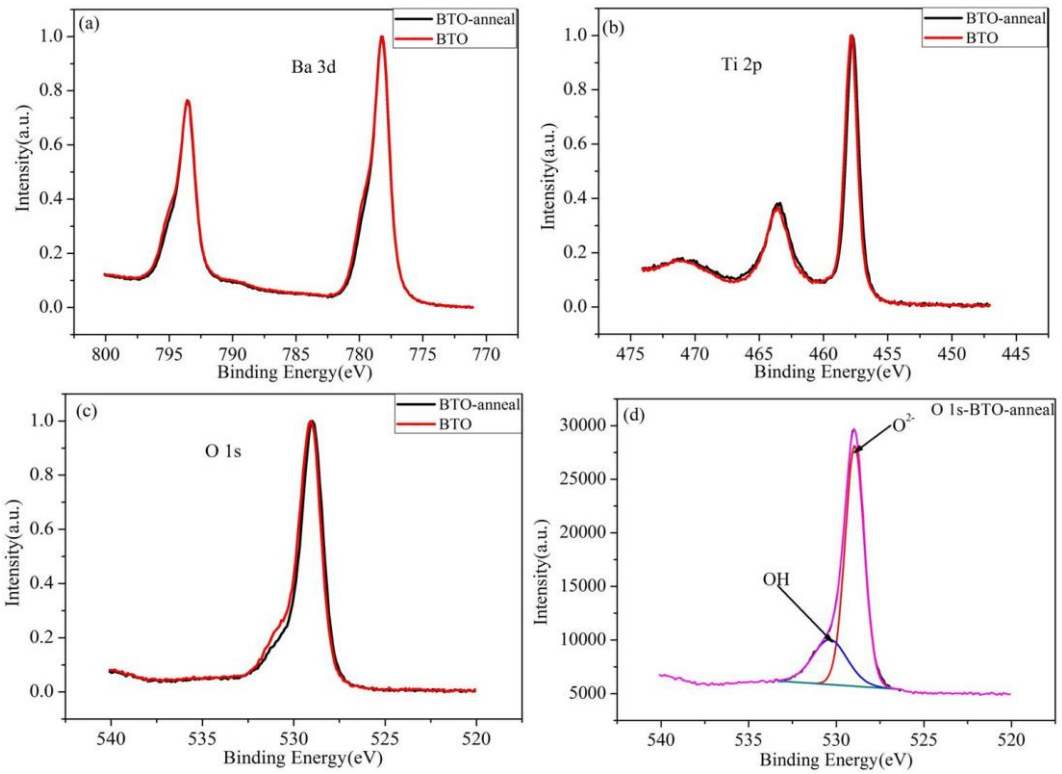

Figure 5.11 XPS spectra for BTO and BTO-anneal after normalization. It can be seen that the spectra of these three constitute elements between BTO and BTO-anneal overlap very well, The hydroxyl oxygen (OH) arising from the normal atmosphere and oxide species (O^{2-}) both contribute to the O 1s peak in BTO-anneal (d). Overall, the XPS spectra of samples post anneal is pretty similar with that of pre-anneal, showing no significant surface chemical state change.

The second effect to observe by comparing the rate constants (Table 5.2) is that Ag-coating of the $BaTiO_3$ catalysts enhances the reaction rate for both unannealed and annealed samples. The enhancement of photocatalytic activity by Ag nanoparticle decoration has been discussed in Chaper 4, due to the role of electron traps, leading to improvement of the separation of electrons and holes, and consequently enhanced photocatalytic activity[193]. The observed improvement in photocatalytic decolourisation efficiency in as-received BTO was obtained in BTO-anneal as well. Additionally, it has been mentioned that noble metal nanoparticles such as Ag and Au enhance the absorption of visible light over a wider wavelength through surface plasmon resonance (SPR)[108].

It is likely that one or both of these effects are producing the enhancement in catalytic activity for the Ag decorated $BaTiO_3$ catalysts that were observed here. To determine whether absorption due to SPR is contributing to the enhanced reaction rate after Ag-coating of the catalysts the diffuse reflectance spectra were recorded (Figure 5.12).

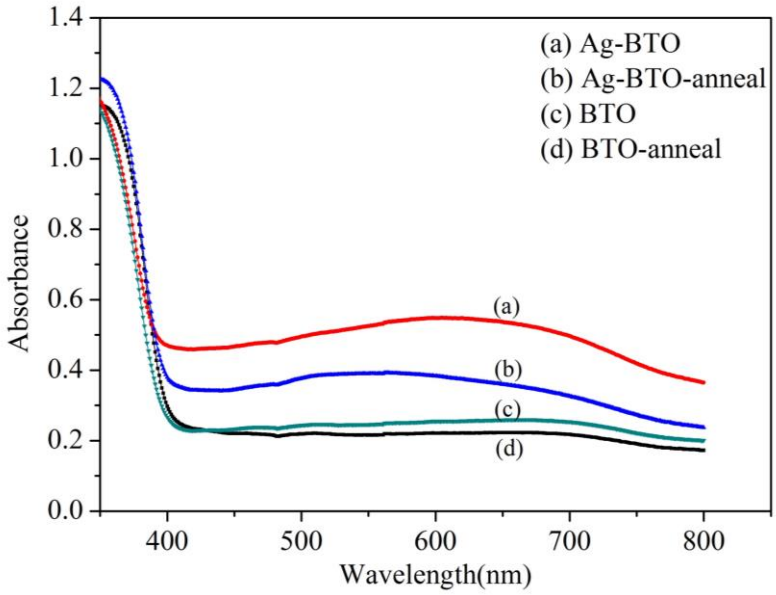

Figure 5.12 Diffuse reflectance spectrum of the four photocatalysts used in the study. Broad absorption bands can be seen for Ag decorated catalysts which are linked to the surface plasmon resonance as in previous studies.

Figure 5.12 showed that after Ag-decoration both Ag-BTO and Ag-BTO-anneal showed enhanced absorption in the visible region, which is attributed to the SPR. In previous studies it has been shown that visible absorption due to SPR can contribute to catalytic activity for Ag-deposited TiO_2[107,160].

To clarify whether SPR or visible irradiation contribute to the best photodecolourisation performance of Ag-BTO-anneal, the photodecolourisation of RhB using Ag-BTO-anneal under different irradiation conditions was carried out. The UV range light and visible light were selectively blocked by applying the optical filters. The obtained photodecolourisation profiles are shown in Figure 5.13.

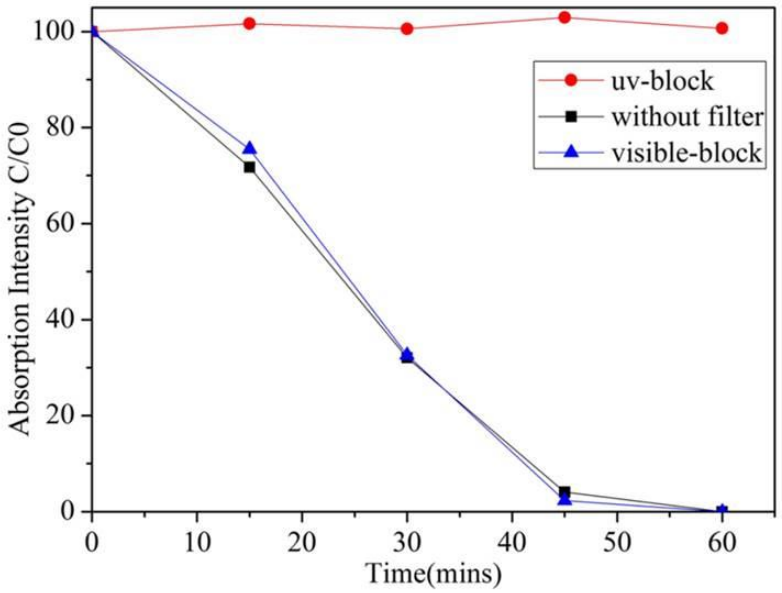

Figure 5.13 Photocatalytic decolourisation of RhB using UV and visible-light-blocking filters using Ag-BTO-anneal. No catalytic activity is observed when the UV illumination is blocked.

According to Figure 5.13, no difference was found between UV-only (visible-blocking) and full spectrum illumination. This indicated that despite the observable visible absorption due to SPR, photoexcited electrons generated through this process did not contribute to the photocatalytic activity. Therefore in the case of Ag-BTO-anneal the enhancement of reaction rate by Ag-coating is attributed to improved charge separation at the surface.

Furthermore, when considering the contribution of Ag decoration to BTO and BTO-anneal, it was found that the enhancement achieved by Ag decoration on the $BaTiO_3$ samples was not equal; the rate constant for Ag-BTO-anneal was a factor of twenty-four greater than BTO-anneal, where Ag-BTO was only eight times more active than BTO. This indicated that the higher ferroelectric content in BTO-anneal enhanced the effect of Ag decoration as well as directly increasing the catalytic activity. It is known that the Ag will deposit on the C+ regions of $BaTiO_3$[18,19], which are the same regions where there will be an excess of photoexcited electrons during the photodecolourisation process.

Therefore, there will be more available electrons in ferroelectric (BTO-anneal) surface decorated by Ag nanoparticles. This will result in an enhancement in the reaction rate. In contrast, in non-ferroelectric BTO where Ag nanoparticles will deposit randomly, the enhancement due to Ag loading will not be significant as annealed ferroelectric BTO. A schematic showing this Ag preferential location and enhanced charge carrier separation was presented in Figure 5.14. Overall we show that the Ag-BTO-anneal catalyst has the highest photocatalytic activity, indicating the combined benefit of ferroelectricity and noble metal decoration to photocatalytic activity.

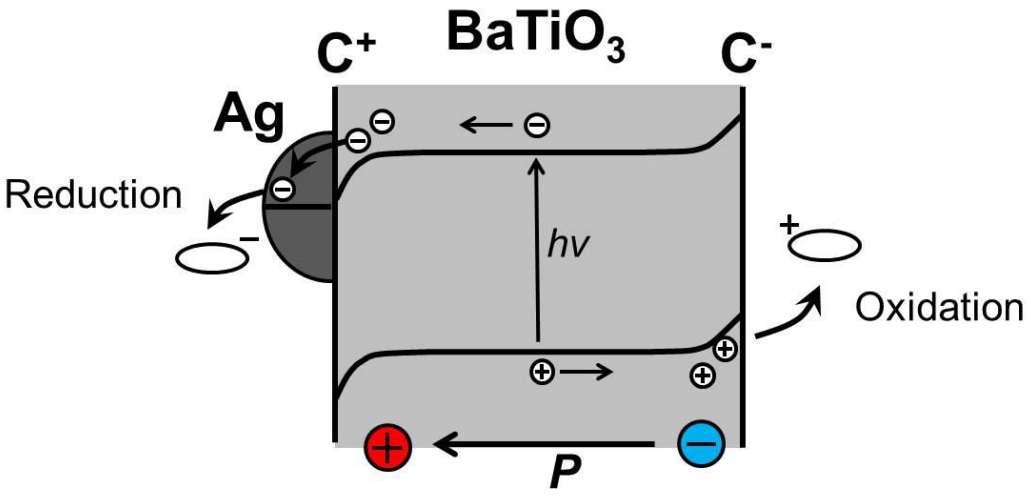

Figure 5.14 Schematic of selective Ag nanoparticle deposition on C+ surface due to downward band bending leading to reduction of silver cations at this location. This further enhances the spatial selectivity of oxidation and reduction on the opposite ferroelectrics.

5.4 Summary

In this chapter, the effect of ferroelectricity of $BaTiO_3$ on its photocatalytic activity in photodecolourisation organic dyes under solar light was investigated. The non-ferroelectric cubic to ferroelectric tetragonal phase transition of $BaTiO_3$ provides a simple way to compare the non-ferroelectric and ferroelectric phases directly. A facile thermal treatment was utilised to modify the ferroelectric phase composition, and then the

photodeposition of Ag nanoparticles on both BTO and BTO-anneal was used to improve the photocatalytic activity.

X-ray analysis and SEM/TEM analysis were employed to measure the change in phase for microstructured $BaTiO_3$ powder. It was demonstrated that it is possible to produce a sample with a higher tetragonal content and therefore increased ferroelectric nature by thermal treatment of as-received, predominantly cubic $BaTiO_3$.

Using photodecolourisation of a target dye molecule Rhodamine B, the variation in rate of decolourisation for non-ferroelectric $BaTiO_3$ compared to ferroelectric $BaTiO_3$ was probed. It was shown that there was a significant enhancement of decolourisation rate when a ferroelectric material was used. This enhanced rate was attributed to the fact that the ferroelectric materials develop a strong Stern layer as evidenced from the enhanced dye adsorption on the ferroelectric catalyst. This demonstrated effective electron-hole and redox chemistry separation at the interface of the catalyst and target dye.

It was also demonstrated that the enhancement of photocatalytic performance through the development of a nanostructured metallic Ag nanoparticles on the surface occurred on both BTO and BTO-anneal. However this effect was more significant for the ferroelectric material (BTO-anneal). This discrepancy was associated with the preferential distribution of Ag on C+ in ferroelectric materials, where the electron accumulated and transferred to Ag easily. Then the contribution of Ag nanoparticles as electron-traps was enlarged in BTO-anneal.

Overall, these results provide evidence that ferroelectric materials show advantage in photocatalytic reactions when compared with the non-ferroelectric materials, and they can act as promising photocatalysts in dye decolourisation.

Chapter 6

Pathways and mechanism of photodegradation of Rhodamine B over Ag modified ferroelectric $BaTiO_3$ under simulated solar light

In the last chapter, the influence of ferroelectricity of $BaTiO_3$ on its photocatalytic activity in decolourisation of RhB was studied. The internal field of ferroelectric $BaTiO_3$ drives spatial separation of electron-hole pairs and then redox reactions, enhancing the photocatalytic efficiency. Then one interesting question will be put forward – does the spatial separation of photoinduced carriers influence the reaction pathway as well? Therefore a further investigation of pathways and mechanism of photodegradation of RhB over the optimum photocatalyst Ag-BTO-anneal-30s (tetragonal ferroelectric phase dominated, simplified as Ag-BTO-anneal thereafter unless otherwise stated) under simulated solar light was carried out to address this question.

A number of studies on traditional semiconductor systems provided an insight into the reaction pathway when oxidation and reduction are not separated at the interface. The photocatalytic reactions can be broadly divided into two mechanisms depending on the process of charge carrier generation and are termed photocatalytic degradation and photoassisted degradation[2,3], as indicated in Figure 6.1.

Photocatalytic degradation can occur when the semiconductor is exposed to super-band gap irradiation. Electrons and holes are formed directly in the conduction and valence band on interaction with incident photons. Photoassisted degradation occurs when sub-band gap light is used. In this instance the organic dye is excited resulting in the injection of carriers (normally an electron) into the semiconductor. This occurs when the conduction band potential of the semiconductor is below the LUMO of the dye molecule,

or chemisorbed molecules such as oxygen molecules followed by the formation of oxidative radicals.

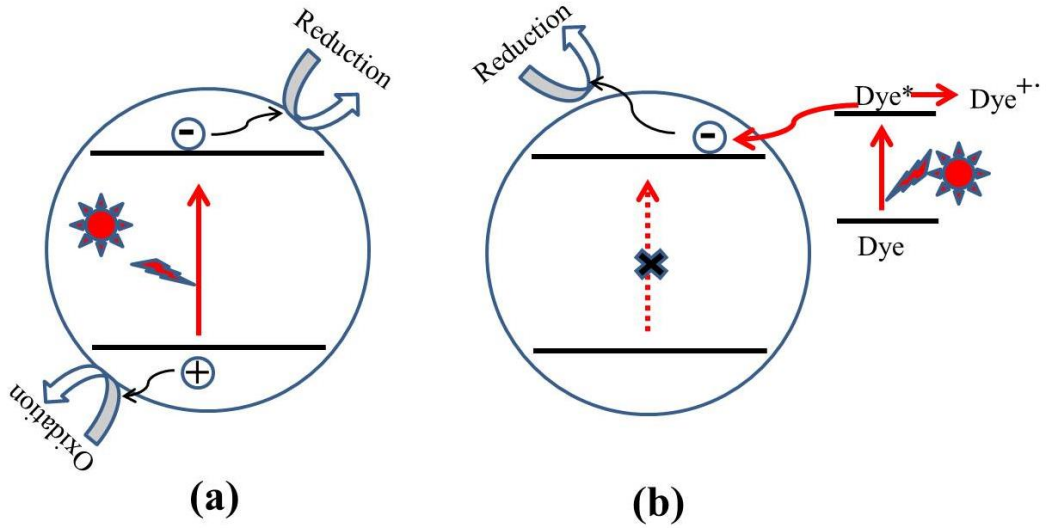

Figure 6.1 Schematic showing the mechanisms of (a) photocatalytic degradation and (b) photoassisted degradation

Various reaction intermediates associated with different reaction pathways for the chemical degradation of Rhodamine B have been reported in different photocatalytic systems[194–203]. Among these reports, a range of catalysts such as $NaBiO_3$[194], Bi_2WO_6[195–197], Y_2GaSbO_7[198], in addition to TiO_2 based catalysts[199–203] have been investigated and showed different degradation pathways and chemical intermediates.

In addition to the range of catalysts generating different reaction intermediates, changes in the surface state, crystalline structure and morphologies of the photocatalysts[204] have also been demonstrated to influence the degradation process[203,205]. However, to date there has been no contribution regarding the degradation pathway for a target dye molecule when a ferroelectric catalyst is used.

It should also be noted that the presence of nanostructured silver on the surface of the $BaTiO_3$-anneal may also influence the reaction pathway through the interaction with a surface plasmon resonance. Our focus is on the reaction with RhB under simulated solar

light over our ferroelectric catalyst. The products of the reaction were evaluated using UV-Vis spectroscopy, ^{1}H nuclear magnetic resonance (^{1}H NMR) and gas chromatography mass spectrometry (GC-MS). To verify our methodology, we employ the widely used photocatalyst TiO_2 (P25) as a reference following the same experimental methods we have used for $BaTiO_3$ to verify our procedures and demonstrate context to the existing literature.

6.1 Photodegradation of RhB under different irradiation conditions

In order to understand the impact of ferroelectric dipoles on reaction pathways, the interaction between photocatalytic degradation and photoassisted degradation must be determined. In order to achieve this, photocatalytic properties of Ag-BTO-anneal were assessed through degradation of RhB under full spectrum solar light, visible light and UV. The latter two irradiation conditions were obtained by passing the solar light through optical filters. The degradation profiles for Ag-BTO-anneal under the different illumination sources have been presented in Figure 5.13.

In the case of our Ag-BTO-anneal system the results do not support the hypothesis that both sub and super-band gap illuminations are driving the reaction. As shown in Figure 5.13, after the UV component of the full solar spectrum was blocked, there was negligible degradation of the dye throughout the course of the experiment period while the photodegradation profiles of full spectrum solar illumination and visible-light filter block almost overlapped. This illustrated that in the Ag-BTO-anneal system, visible light had limited contribution to the degradation and only UV excited charge carriers were participating in the degradation reaction. The photoassisted degradation process was hindered with respect to the direct photocatalysis.

In comparison, for a standard TiO_2 system, both visible-light-driven photoassisted oxidation and UV-driven photocatalytic oxidation have been shown to coexist during the degradation process, shown in Figure 6.2, which was consistent with previously reported results[206].

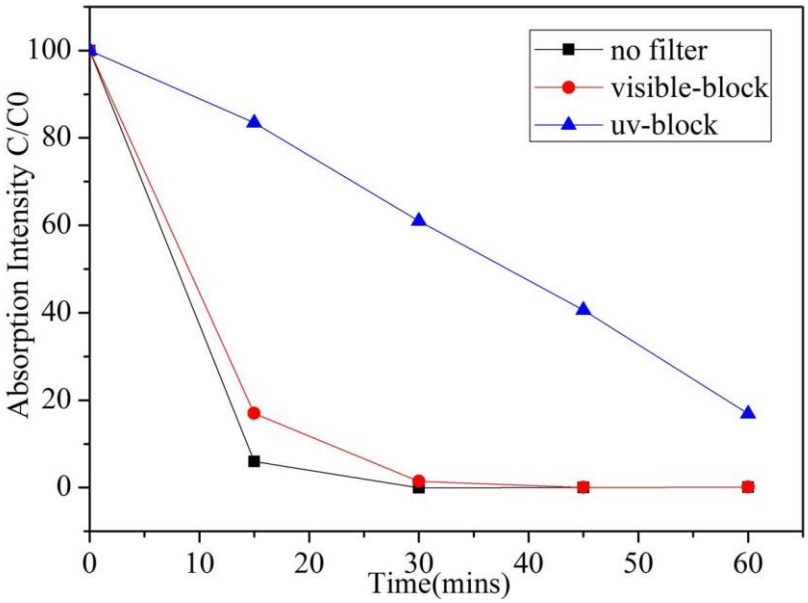

Figure 6.2 Photodegradation of RhB using TiO_2 (P25) under solar light, visible light and UV light. In TiO_2 system, both visible light and UV contribute to the degradation.

It is known that the conduction band gap position of the semiconductor is required to be lower than the lowest unoccupied molecular orbital (LUMO) of the dye to make electron transfer successful for photoassisted degradation. The structure of RhB is accepted to give the LUMO and HOMO positions at 1.1 eV and -1 eV versus NHE[207]. In terms of the band structures of a semiconductor the specific band position of the semiconductor at the point of zero charge can be calculated according to the empirical equation[208,209]:

$$E_{CB} = X - E^e - 0.5E_g \tag{6.1}$$

Where E_{CB} is the conduction band edge, X is the electronegativity of the semiconductor, E^e is the energy of free electrons on the hydrogen scale (about 4.5 eV), and E_g is the

band gap energy of the semiconductor. The electronegativity of the semiconductor can be calculated from the geometric mean of the electronegativity of the constitute atoms. We have measured the direct band gap of Ag-BTO-anneal to be around 3.14 eV by extrapolating the linear portion of $(\alpha h\mu)^2$ vs $h\mu$ [210] using a Tauc plot that is shown in Figure 6.3. Our measured value for the system in use here is consistent with other publications, where the band gap of $BaTiO_3$-anneal powder was reported to be direct at 3.18 eV[211].

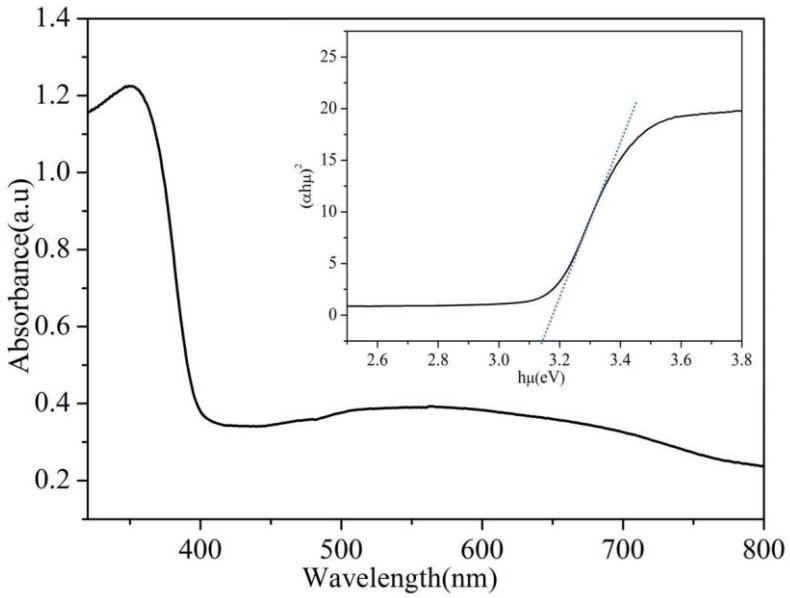

Figure 6.3 Tauc plot for Ag-BTO-anneal using the relationship between the square of αhμ versus photon energy for a direct semiconductor system. By extrapolating of the linear portion we determine the band gap to be 3.14 eV.

Table 6.1 shows the adopted and calculated values for the band edge positions using Equation 6.1. We do not believe that the presence of the nanostructured silver on the surface will significantly influence the band positions of the $BaTiO_3$-anneal considering the low amount and small size of silver nanoparticles.

Table 6.1 Absolute electronegativity, band gap, conduction and valence band edge of Ag-BTO-anneal at the point of zero charge

Material	Absolute Electro -negativity*	E_g (eV)	E_c Edge (eV)	E_v Edge (eV)
Ag-$BaTiO_3$-anneal	5.13	3.14	-0.94	2.2

***The absolute electronegativity of constitute atoms are adapted from Pearson's work[212].**

The energy level diagrams of the Ag-BTO-anneal catalytic systems from Table 6.1 are shown schematically in Figure 6.4 (a), which also shows the proposed reaction mechanisms. When Ag-BTO-anneal was dispersed in the cationic dye RhB solution, the dye molecules will be attracted to the negative domains (c-) on the surface of the ferroelectric powder. The c+ surfaces will hold a net positive charge and so will not attract and absorb the cationic dye. As Ag is a conductor it will screen the charge in the ferroelectric but the whole c+ surface will have a net positive charge. The c- face is where holes accumulate leading to upward band bending, as shown in Figure 6.4 (a). Due to the proximity of the conduction band edge (-0.97 eV) and LUMO of RhB (-1 eV) and upward band bending of the ferroelectric c- domain, we propose that this is enough of a barrier to prevent electron injection from the excited dye to the conduction band of BTO-anneal. This reduced injection of electrons will be manifested by a reduction in the rate of dye degradation. Once the electron transport cannot overcome the barrier formed at the catalyst surface and solution the photoassisted process will be suppressed. Accordingly visible light cannot contribute to the degradation process, which was in agreement with the phenomenon observed in Figure 5.13.

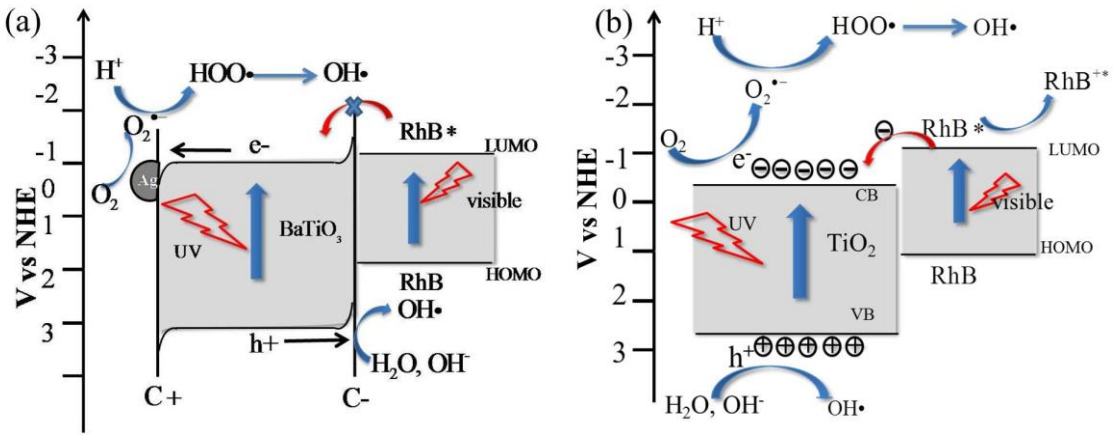

Figure 6.4 The calculated energy level diagram and the degradation reactions in (a) Ag-BTO-anneal system and (b) TiO_2 system under simulated solar light. Photoassisted degradation was hindered due to the barriers arising from band bending in ferroelectric Ag-BTO-anneal system while both photoassisted and photocatalytic degradation coexisted in TiO_2 system.

The mechanisms of ferroelectric Ag-BTO-anneal system was different from the TiO_2 system, where the photocatalytic and photoassisted reactions can coexist (see Figure 6.4 (b)). The band gap position of TiO_2 shown was calculated using the same methods as $BaTiO_3$-anneal. The band gap of TiO_2 was assumed to be 3.2 eV, and the conduction band and valence band edge were calculated to be locate at -0.29 eV and 2.91 eV respectively. The band position values obtained were consistent with those reported[213]. As indicated, photoassisted degradation induced by the electron injection from excited RhB molecules to the conduction band of TiO_2 contributed to the overall photodegradation, which explained the phenomenon observed in Figure 6.2.

Overall, it can be concluded that due to the existence of barriers arising from band bending in the ferroelectric Ag-BTO-anneal system, photoassisted degradation was hindered and only photocatalytic degradation contributed. This is in contrast with non-ferroelectric TiO_2 system.

6.2 UV-Vis absorption spectra

Figure 6.5 shows the UV-Vis absorption spectra of RhB dye solution at different stages of decolourisation represented by the percentage of absorption at a fixed wavelength (554 nm) in Ag-BTO-anneal system. The spectra show a previously observed shift of absorption wavelength during degradation of RhB[194,196,202,203]. The change of maximum absorption wavelength as a function of decolourisation for the dye is shown in Figure 6.6. There were two clear stages to the trend for the shift of wavelength. Up to 80% decolourisation there was only a slight shift in the wavelength of absorption (to a maximum of 2 nm) while in the second stage of reaction the maximum wavelength of absorption exhibited by the dye shifted significantly by 55 nm.

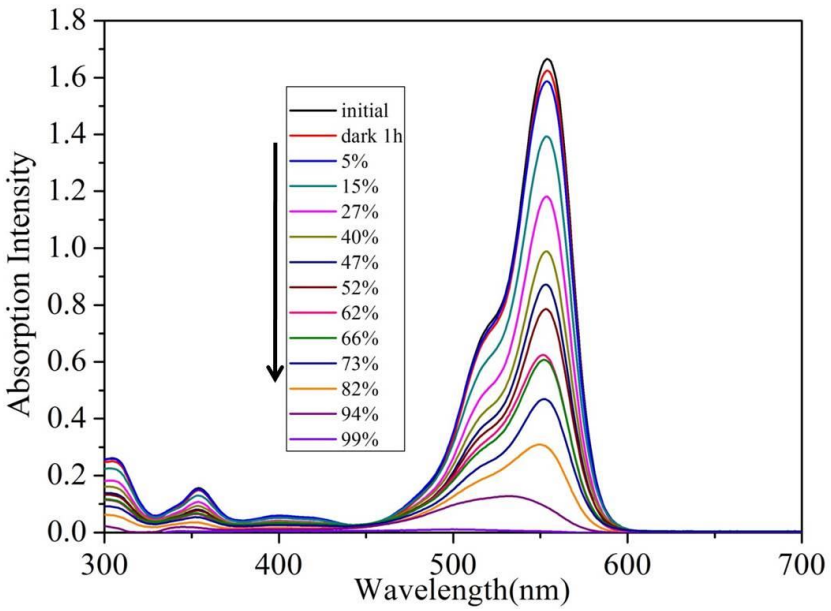

Figure 6.5 UV-Vis absorption spectra of RhB dye solutions with different degradation percentage in Ag-BTO-anneal system

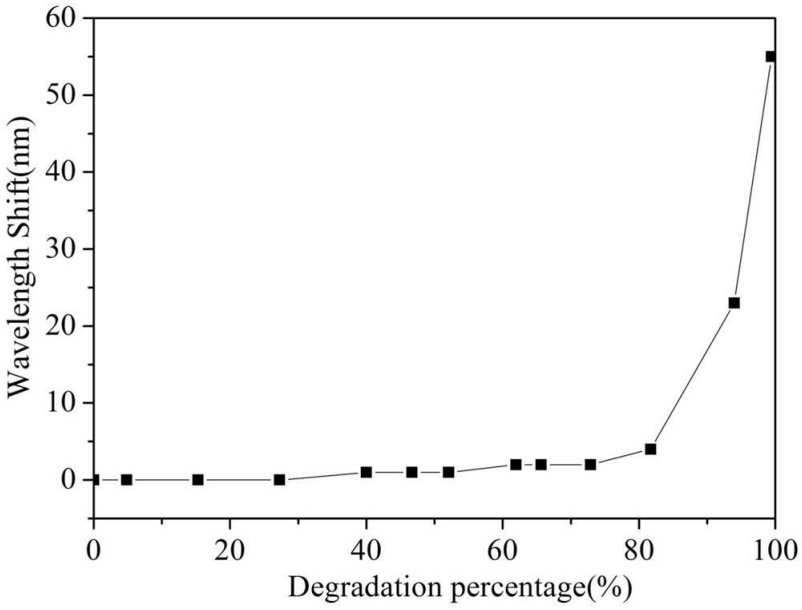

Figure 6.6 The maximum absorption wavelength shift of RhB as a function of degradation percentage in Ag-BTO-anneal system

The shift in absorption maximum wavelength has been associated with the deethylation process. The four ethyl group in RhB are removed one by one and a series of N-de-ethylated intermediates are formed[202]. This deethylation process accompanies and competes with cleavage of the conjugated chromophore structure during the overall degradation process. Our Ag-BTO-anneal system showed a slight hypsochromic wavelength shift during the initial stage of degradation, indicating that cleavage of chromophore structure predominated.

In the Ag-BTO-anneal system, as described above, only UV induced photocatalytic degradation contributes to the whole process, and the oxidative radicals are generated from the reactions between charge carriers from the catalysts and other species (O_2, OH^-, etc.). This is typical for systems undergoing such a photocatalysed reaction where the production of OH^- and other active species is the initial step in photochemical reaction[194]. In contrast, in the photoassisted degradation, the reactive species are produced near the adsorption site of the RhB molecules, where the excited dye molecules inject electrons

into the semiconductor. Therefore, it is easier for the reactive species to selectively attack the adsorbed group compared with photocatalytic degradation.

The zeta potential of Ag-BTO-anneal was determined and pH_{pzc} was demonstrated to be 3.4 as presented in Figure 6.7 (a). Therefore it will be negatively charged under experimental conditions. RhB dye molecules will be preferentially adsorbed on the surface of photocatalyst through positively-charged alkylamine group (-NEt2 group) due to the Coulomb attraction between the photocatalysts and alkylamine group[194,200,203], as shown in Figure 6.7 (b).

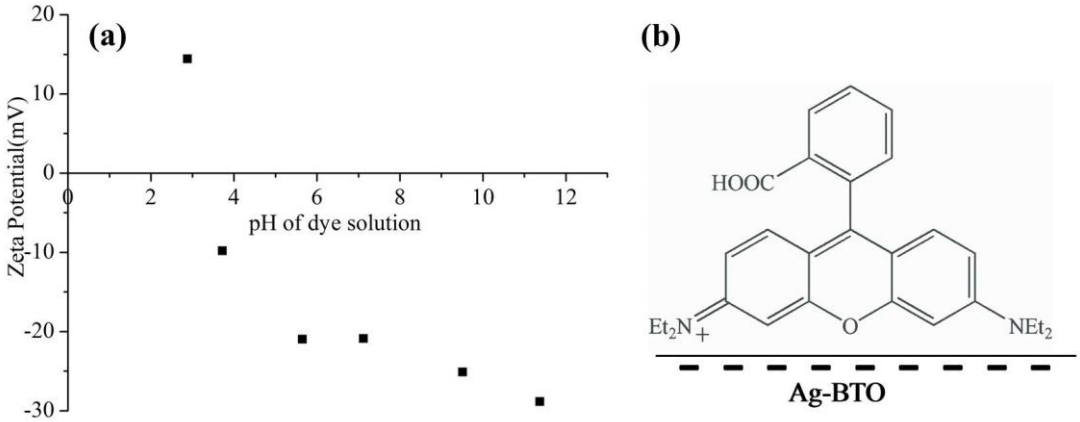

Figure 6.7 (a) Zeta potential as a function of pH for Ag-BTO-anneal. pHpzc (Ag-BTO-anneal) = 3.4 . Under the experimental condition, where the pH value of initial dye solution was around 7.52, the catalysts will be negatively charged. (b) the proposed adsorption mode between negative charged photocatalysts and positive charged alkylamine group.

Therefore, in Ag-BTO-anneal system, where only UV-induced photocatalytic oxidation exists, it is less likely that reactive radicals selectively attack adsorbed alkylamine group in Ag-BTO-anneal. This will lead to non-obvious deethlylation and a slight wavelength shift. This argument is consistent with the observations from previous work, where under UV irradiation the deethylation process was not so obvious as when under visible irradiation[199].

To provide a reference and demonstrate the robustness of our test regimes, TiO_2 was used as a model photocatalyst and used to compare products of the dye at the same decolourisation stage, shown in Figure 6.8. Overall we find that TiO_2 system presents a similar degradation process, that is the cleavage of chromophore structure predominated over deethlylation. This observation is in accordance with the other reported results[200,203,214], where degradation of RhB with TiO_2 under visible light was regarded to be mainly destruction of chromophore structure. Our findings indicated that the presence of the metal nanostructures and the ferroelectric nature of the catalyst have not significantly influenced the process of cleavage of the chromophore and indicates that our experimental procedure is robust.

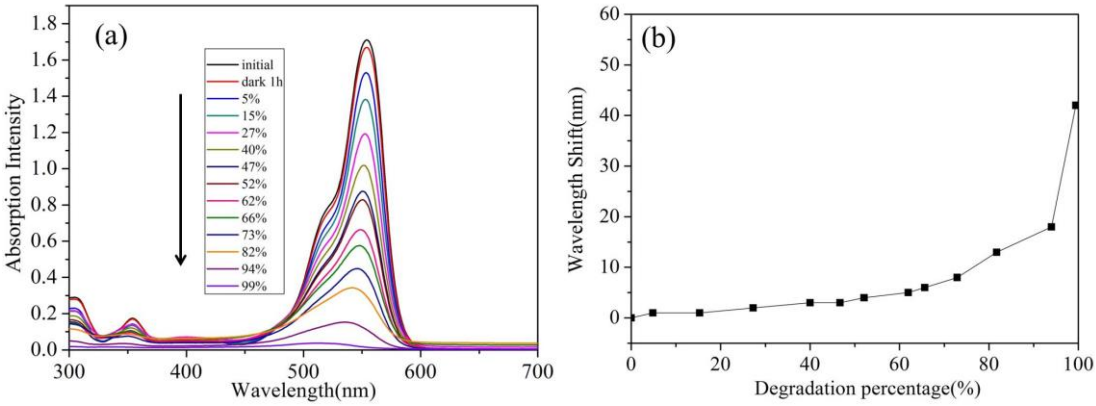

Figure 6.8 (a) UV-Vis absorption spectra of RhB at different degradation percentage in TiO_2 system (b) The comparison of maximum absorption wavelength shift of RhB as a function of degradation percentage in TiO_2 system.

6.3 ^{1}H NMR spectroscopy

To observe the structural changes of RhB during the degradation processes proton NMR analysis was performed. Six samples at the same percentage decolourisation, were evaluated using ^{1}H NMR. Figure 6.9 shows the NMR spectra for the degradation of RhB using Ag-BTO-anneal catalyst. The NMR signals from different protons in the RhB structure have been assigned peaks **d**, **e**, **f**, **g**, **h**, **i** and **j** represent aromatic hydrogen atoms

H_d, H_e, H_f, H_g, H_h, H_i and H_j (Figure 6.10). The hydrogen atoms in the ethyl group of RhB structure contributed to the NMR peaks at δ 1.15-1.25 ppm and δ 3.6 - 3.6 ppm. In addition, there were a series of small peaks between peak **a** and peak **b** in the initial RhB sample. After careful examination of the NMR spectra of pure RhB and after catalyst loading, these peaks have been assigned to an impurity from RhB and/or the NMR sample preparation process.

As the photodegradation progresses the intensity of the characteristic peaks associated with aromatic hydrogen atoms (peaks **d-j**) and ethyl group (peaks **a** and **b**) decrease while new peaks appear at δ 3.0-3.1ppm and around peak **a** (δ1.15-1.25ppm) as highlighted in Figure 6.9. The disappearance of characteristic peaks indicated the breakdown of chromophore structures and simultaneous removal of ethyl groups during the degradation process. The new peaks in the spectrum were associated with the intermediate products formed during degradation. In addition to the intensity decreasing for the characteristic peaks, a peak shift can be observed. As highlighted in Figure 6.9, peaks **d**, **e** and **f** moved to a higher chemical shift while peaks **g**, **h**, **i** and **j** remain in place. If we consider the hydrogen atoms which these peaks represent in the RhB structure, this chemical shift could be associated with either the deethylation process or break down of the xanthene ring.

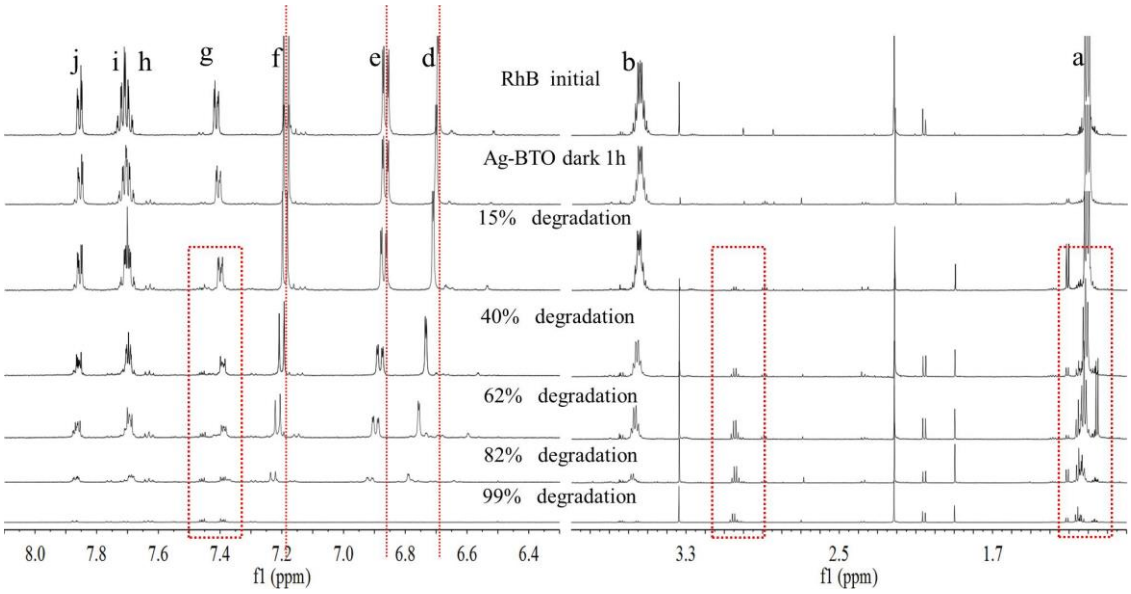

Figure 6.9 ^{1}H NMR spectra of samples with different degradation percentage with Ag-BTO-anneal

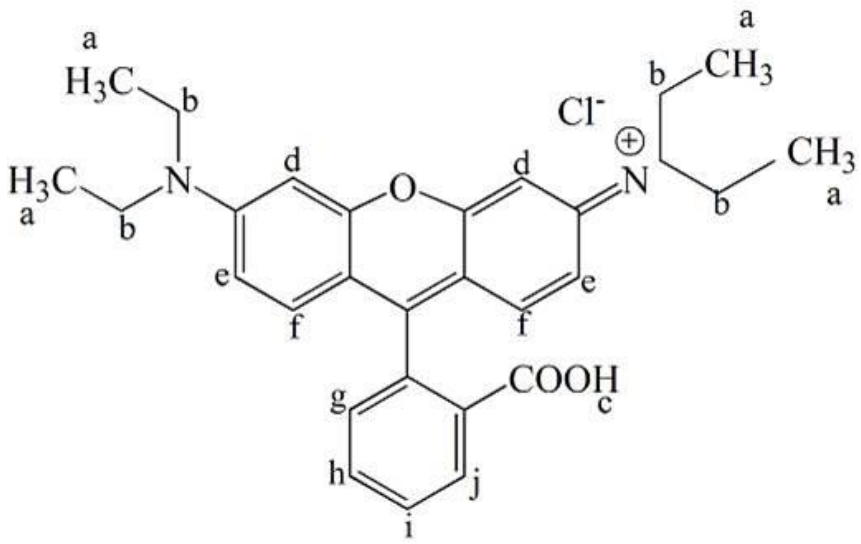

Figure 6.10 The chemical structure of Rhodamine B

Figure 6.11 shows the NMR spectra for the degradation of RhB for the TiO_2 system. Being the same as Ag-BTO-anneal system, the characteristic peaks for aromatic hydrogen atoms and ethyl group disappeared. Meanwhile, new peaks appeared at δ 3.0-3.1 ppm and at δ 1.15-1.25 ppm were observed. The latter peaks were considered to be signals from –

CH_3 and analogous group. These features were consistent with the other RhB degradation works using TiO_2 as catalysts[202,204].

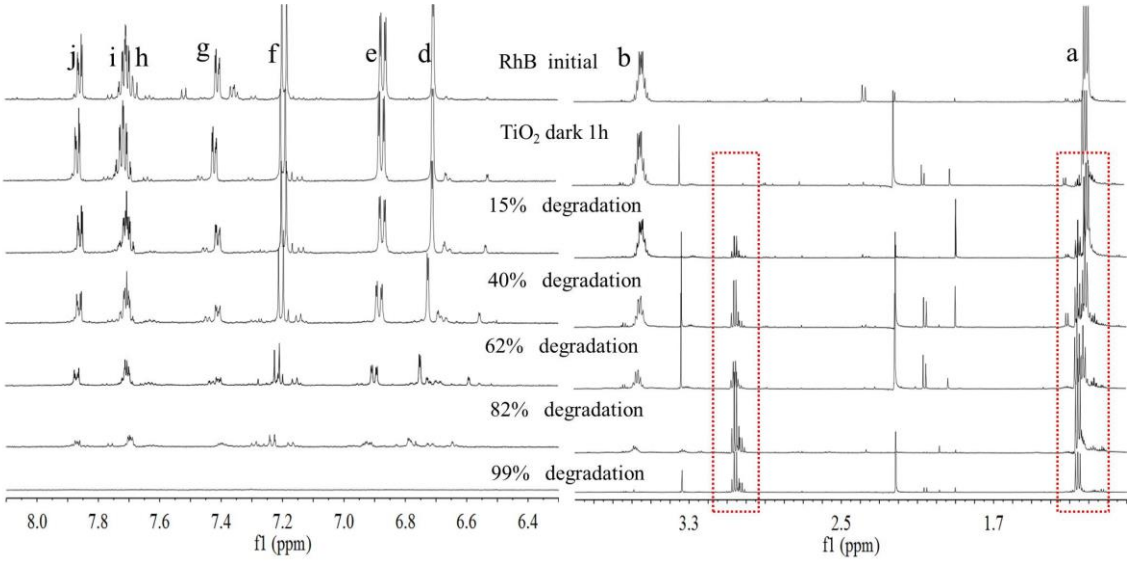

Figure 6.11 ^{1}H NMR spectra of samples with different degradation percentage with TiO_2

6.4 Identification of intermediates by GC-MS

Figure 6.12 shows the gas chromatography of samples with irradiation for 10 and 90 minutes in Ag-BTO-anneal system. After discounting peaks associated with the impurities in the system, new peaks (marked by ☆) were observed for the Ag-BTO-anneal system. These have been associated with intermediate products produced during the degradation process. The peaks at the retention time 5.82 minutes (Figure 6.12 (a)) and the peak with a retention time of 5.928 minutes (Figure 6.122 (b)) have been assigned to benzoic acid according to the mass fragmentation pattern. The small differences in retention time arise from individually sample injections.

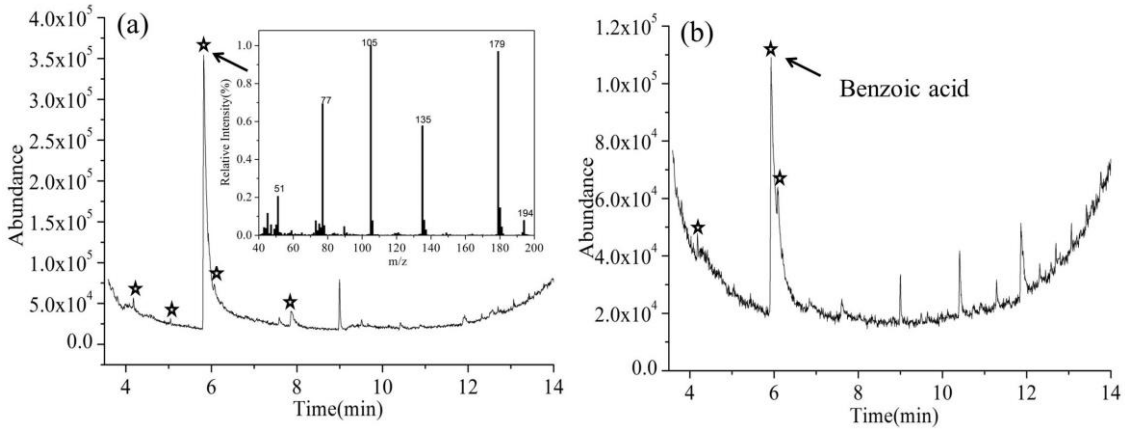

Figure 6.12 Gas chromatorgraphy of RhB with Ag-BTO-anneal after irradiation for (a) 10mins and (b) 90mins under solar simulator, with mass spectrum of the peak at 5.82 min(a), indicating the presence of benzoic acid. The peak at 5.928 min in (b) presents the same mass spectrum and can be assigned to benzoic acid as well.

In addition to the benzoic acid peak, there were new peaks at 4.172 minutes, 5.044 minutes, 6.068 minutes, 7.862 minutes in Figure 6.122 (a) and 4.179 minute, 6.087 minute in Figure 6.122 (b). However, we have not been able to assign a chemical structure to these peaks according to the mass fragmentation pattern. As they do not exist in the blank experiments and are not impurities so it is reasonable to assume that they are intermediate products in the degradation.

Comparing between Figure 6.122 (a) and (b), with the irradiation time increasing to 90 minutes, some new peaks observed in Figure 6.122 (a) have diminished while the intensity of benzoic acid peak dropped. The change in the pattern of the GC-MS relates the species that are in solution during the degradation of the RhB. The results shown here indicated that as the photochemical process proceeds the reaction intermediates are reacting to form a new mixture during degradation of the RhB.

The distribution of intermediates and degradation pathways for Rhodamine B using different catalysts have been investigated[194–203]. These previous works described a number of discrepancies in the intermediates found during the degradation of RhB.

However, phthalic acid and benzoic acid have been widely observed and have become the accepted, or the most probable, intermediates during the degradation of RhB.

In order to test this and support our observation, we performed experiments where we ran phthalic acid and benzoic acid as the target molecule through the GC-MS. From this we were able to determine the expected output for the two molecules using our GC-MS system. The retention time of phthalic acid and benzoic acid were found to be 8.644 minutes and 5.864 minutes (Figure 6.13). After examining the GC-MS results for the degradation of RhB over Ag-BTO-anneal, no peaks could be found that matched the peak position and mass fragmentation pattern of phthalic acid. This excluded the possibility of phthalic acid being produced as an intermediate when RhB is degraded over Ag-BTO-anneal. The peaks which have been assigned to benzoic acid in Figure 6.12 are in consistent with standard benzoic acid in terms of retention time and mass spectra. This further demonstrates the existence of benzoic acid as intermediate. Overall, the intermediates observed in Ag-BTO-anneal system are summarized in Table 6.2.

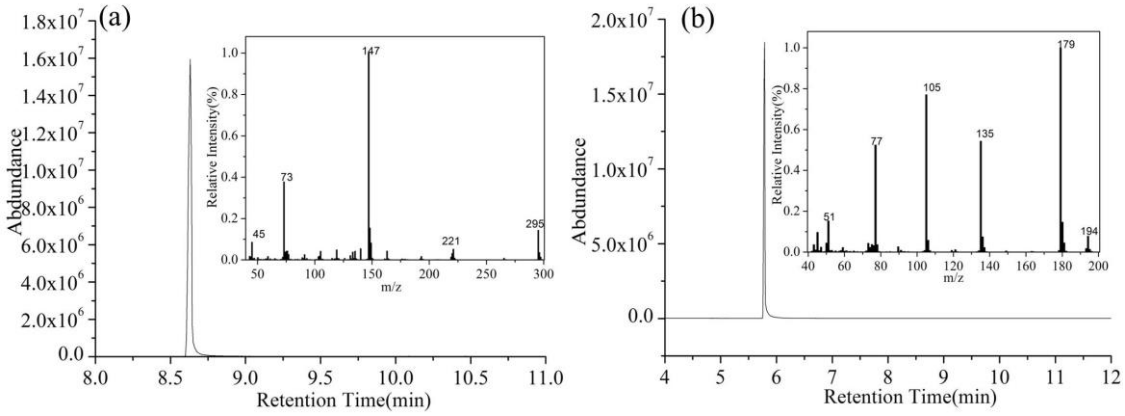

Figure 6.13 (a) Gas Chromatography of standard phthalic acid with corresponding mass spectrum inset (b) Gas Chromatography of standard benzoic acid with corresponding mass spectrum inset

Table 6.2 Gas chromatography peaks detected in Ag-BTO-anneal system

Catalytic system Ag-BTO	Retention time of Peaks obtained
T=10 min	4.172 minutes, 5.044 minutes, 5.82 minute s (benzoic acid), 6.068 minutes, 7.862 minutes
T=90 min	4.179 minutes, 5.928 minutes (benzoic acid), 6.087 minutes

The intermediates in TiO_2 system were also analysed following the same methodology, and its gas chromatorgraphy was shown in Figure 6.14. Ethylene glycol (at retention time 3.771 minutes) and benzoic acid (at retention time 5.8 minutes) have been identified as part of the intermediates in addition to a few other peaks unassigned in the sample at irradiation time 10 minutes. Here it should be mentioned there was no obvious peak in Figure 6.14 (a) which was assigned to benzoic acid. However, the mass spectra of the region at retention time 5.8 min contained the fragment patterns of standard benzoic acid, as indicated in Figure 6.15. The confirmed species have been observed and reported as intermediates during degradation of RhB in TiO_2[204,215] and other catalytic systems[194,196], supporting the feasibility of the experimental process.

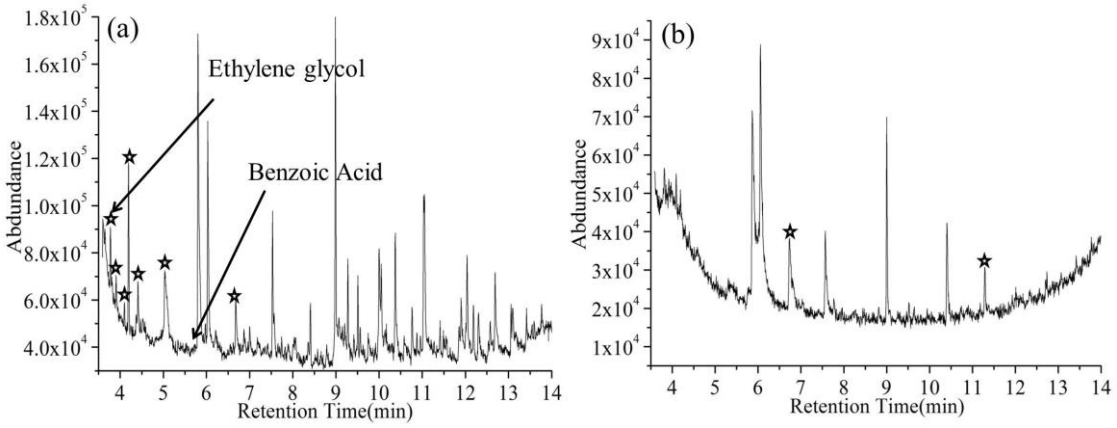

Figure 6.14 Gas Chromatorgraphy of RhB with TiO_2 after irradiation for (a) 10mins and (b) 90min under solar simulator. In (a), the peaks assigned ethylene glycol and benzoic acid were shown. Herein, the confirmation of benzoic acid was referenced to Figure 6.15.

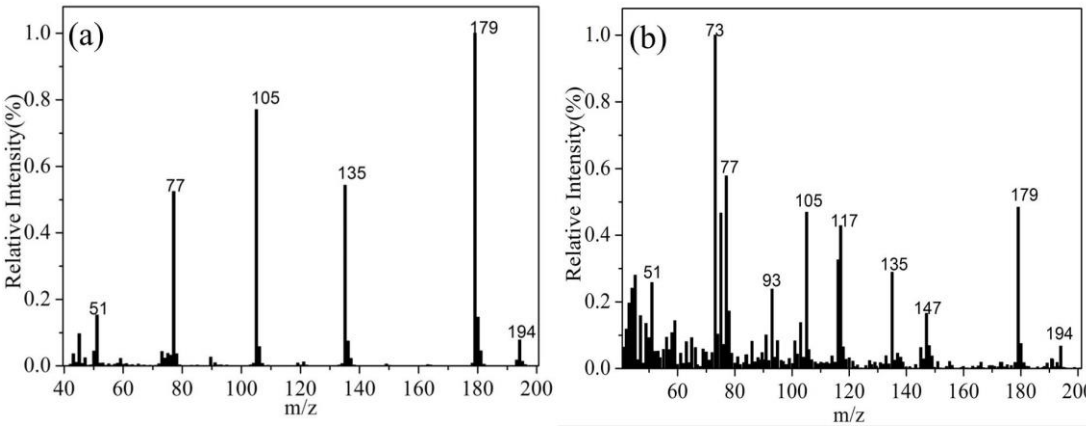

Figure 6.15 The comparison between (a) the mass spectrum of standard benzoic acid and (b) the one obtained from our gas chromatography at a retention time around 5.8min in Figure 6.14(a). The right mass spectrum contains all the fragments of benzoic acid, showing the existence of benzoic acid.

Based on the UV-Vis sprectroscopy, NMR and GC-MS analysis discussed above, it can be concluded that there is no significant difference in the intermediates distribution and degradation pathway in ferroelectric Ag-BTO-anneal system with respect to the nonpolar TiO_2 system.

As reviewed in section 2.2, ferroelectric materials have been demonstrated to show some intriguing polarisation-dependent surface properties. Therefore, it was expected that there will be some intriguing phenomenon on the ferroelectric surface when interacting with dye molecules, and that would lead to a varied degradation pathway. However, according to our results, it seems there is no significant change in the intermediates distribution and degradation pathway with respect to the nonpolar TiO_2 system. There could be a number of reasons to account for this.

First, our ferroelectric system is ferroelectric powder, of which the polarisation orientation is not systematically controlled. Thus the potential effect of polarisation will not be evident as poled thin film or single crystal which is widely used in the investigation of polarisation effect.

In addition, it was proposed that the geometry of transition metals on ferroelectric substrate plays an important role in enlarging or inhibiting the polarisation effect[80]. When the metal clusters are too thick for their surface to be affect by the underlying polarisation, it will behave similarly to the other nonpolar systems. But in our system, the size of Ag nanoparticles is only 5-10 nm, which is not likely to block the effect from polarisation, although the exact critical thickness is not known. Thus the first reason is more likely.

Nevertheless, our initial attempt to probe into the degradation mechanism, intermediates and pathways in degradation of RhB dye molecules using ferroelectric $BaTiO_3$ provides a deeper understanding in ferroelectric catalytic system and add directions to the development of a new efficient photocatalyst.

6.5 Summary

In this chapter, UV-Vis spectroscopy, NMR and GC-MS were employed to investigate the degradation process of Rhodamine B under simulated solar light with silver modified $BaTiO_3$ as a photocatalyst. Our results indicated that the polarisation of the dipole associated with the ferroelectric forms band bending and this hinders the photoassisted degradation process between adsorbed dye and the catalyst, such that we see no evidence of direct electron injection from the dye into the Ag-BTO-anneal. Only photocatalytic degradation contributed to the overall photodecolourisation process.

A slight hypsochromic wavelength shift of the maximum absorption peak shown during the initial stage of degradation by UV-Vis demonstrated that the cleavage of the chromophore structure was the primary initial process of molecule breakdown. This shift in absorption did not occur until later stages of molecule fragmentation. The use of NMR analysis further supported the hypothesis that during degradation there was cleavage of the chromophore structure followed by deethylation of the dye molecule.

Analysis of the breakdown products showed that we have been able to identify benzoic acid as the main intermediate based on GC-MS analysis. The lack of other fragments identified during the breakdown of the dye is associated with retention of fragments on the catalyst and a full mineralisation of the dye molecules to liberate CO_2.

Chapter 7

Influence of ferroelectric dipole on the photocatalytic activity of $BaTiO_3$-anneal-Fe_2O_3

According to the results obtained in previous chapters, the advantage of ferroelectric $BaTiO_3$ in semiconductor photocatalysis has been demonstrated. Then this raises the question of whether the ferroelectric photocatalysis system can be combined such that the ferroelectric dipoles in ferroelectric materials affect the adjacent non-ferroelectric material in a heterojunction. It has been reported that the water decomposition rate on the thin layer of TiO_2 deposited on ferroelectric $LiNbO_3$ was polarisation-dependent[138]. This was attributed to the charge carrier behaviours of TiO_2 being affected by the underlying ferroelectric dipole. In addition, it has been found that the redox reactions taking place on a thin layer of non-ferroelectric TiO_2 was spatially separated due to influence from the ferroelectric $BaTiO_3$ substrate[61,62]. The reason was considered to be that the spatially separated charge carries generated in the substrate were able to tunnel through TiO_2 layer and take part in the photochemical reactions. All of these reports suggest the promise of combining ferroelectric materials with non-ferroelectric materials, especially when the anomalous band positions[216] and extended carrier lifetime of a non-centrosymmetric material are considered[217].

In this chapter, hematite (α-Fe_2O_3) was chosen as the non-ferroelectric material, which has been widely applied in photocatalysis[218] but with the disadvantages of a very short hole diffusion length (2-4 nm) and charge carrier lifetime(<10 ps)[219]. $BaTiO_3$-anneal (annealed, ferroelectric) and α-Fe_2O_3 were combined to form heterostructured photocatalysts and the influence of the ferroelectric dipole was investigated.

7.1 Charaterisation of heterostructured $BaTiO_3$-anneal-Fe_2O_3

The morphologies of different photocatalysts were studied using SEM and the micrographs are shown Figure 7.1. The morphologies of BTO-anneal-Fe_2O_3-0.001M particles (Fig. 7.1 (a)) were almost the same with bare $BaTiO_3$-anneal (Fig. 7.2 (a)). As the amount of loaded α-Fe_2O_3 increases, some extra features can be observed on the surface of $BaTiO_3$-anneal. The surface of particles was not smooth as bare $BaTiO_3$-anneal, and instead certain second phase distributed on the surface, especially obvious in Fig. 7.1 (c) and (d). According to the EDX analysis of the surface composition (inset of Fig. 7.1 (b)), the existence of Fe element demonstrated that certain iron species were deposited on the surface. The morphologies of pure BTO-anneal and α-Fe_2O_3 are also shown in Figure 7.2 and a much smaller particle size was obtained for pure Fe_2O_3.

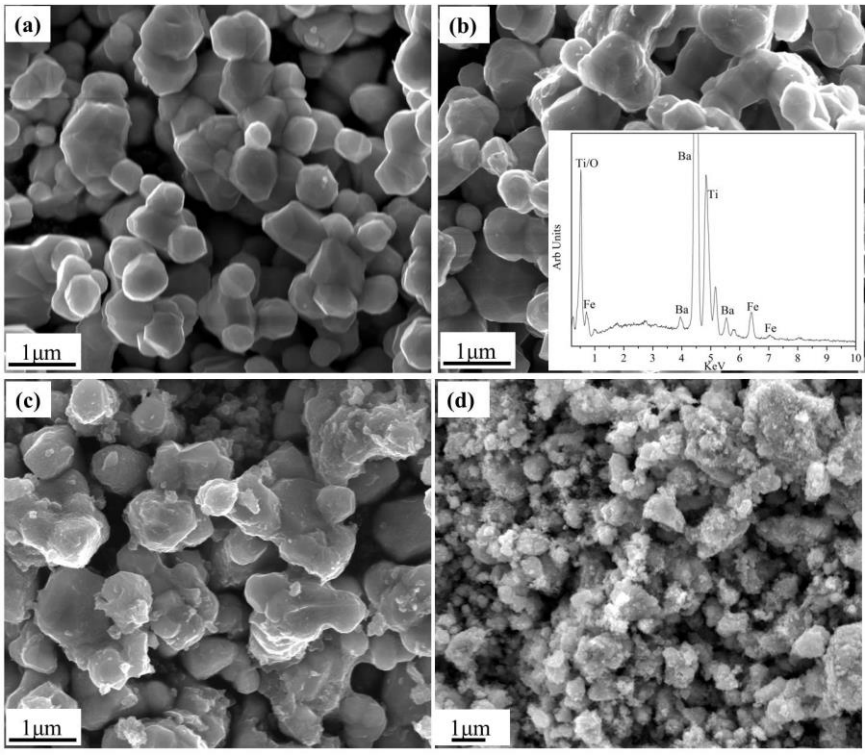

Figure 7.1 SEM micrographs of micrographs of (a) BTO-anneal-Fe_2O_3-0.001M, (b) BTO-anneal-Fe_2O_3-0.01M with the corresponding EDX spectrum of (b), (c) BTO-anneal -Fe_2O_3-0.1M and (d) BTO-anneal -Fe_2O_3-0.5M. With increasing of Fe_2O_3 mass ratio, the morphologies of photocatalysts changed and EDX analysis showed the existence of Fe species on the surface.

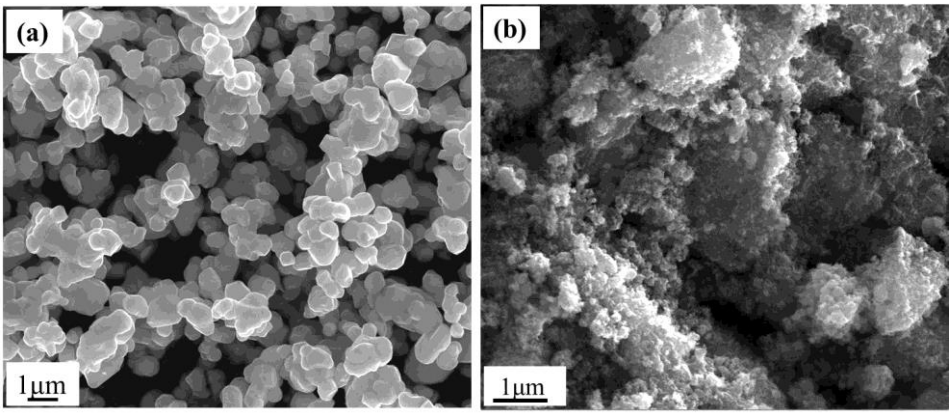

Figure 7.2 SEM micrographs of (a) bare BTO-anneal and (b) α-Fe_2O_3

The phase compositions of the prepared powder catalysts were analysed using X-Ray diffraction and the XRD patterns are shown in Figure 7.3. As exhibited in Fig. 7.3 (a), the diffraction peaks of synthesised Fe_2O_3 can be indexed by hematite α-Fe_2O_3 (JCPDS33-0664). This indicated that the methodologies adopted can successfully produce α-Fe_2O_3. In the XRD patterns of heterostrutured BTO-anneal-Fe_2O_3, the characteristic patterns of α-Fe_2O_3 was absent for BTO-anneal-Fe_2O_3-0.001M, 0.01M and 0.1M , and only the peaks assigned to tetragonal $BaTiO_3$ (JCPDS 05-0626) were observed in Fig. 7.3 (e) to (c). With further increasing the loading amount of Fe_2O_3, the characteristic peaks of both α-Fe_2O_3 and tetragonal $BaTiO_3$ arise in BTO-anneal-Fe_2O_3-0.5M (see Fig. 7.3 (b)). Therefore, it can be considered that the absence of characteristic peaks of α-Fe_2O_3 was related to the small amount of α-Fe_2O_3 on the surface. In addition, a high-dispersion of small-size Fe_2O_3 (smaller than 10 nm determined by TEM, and will be discussed later) on the surface of large-size $BaTiO_3$-anneal (around 600 nm on average based on SEM) can also account for this absence of α-Fe_2O_3 signal. The similar phenomenon and statement were reported in the work on α-Fe_2O_3/TiO_2 nanocomposites[220]. Based on the phase composition investigation by XRD, it can be concluded that the iron species observed in SEM/EDX was α-Fe_2O_3, which can be further supported by XPS and TEM discussed below.

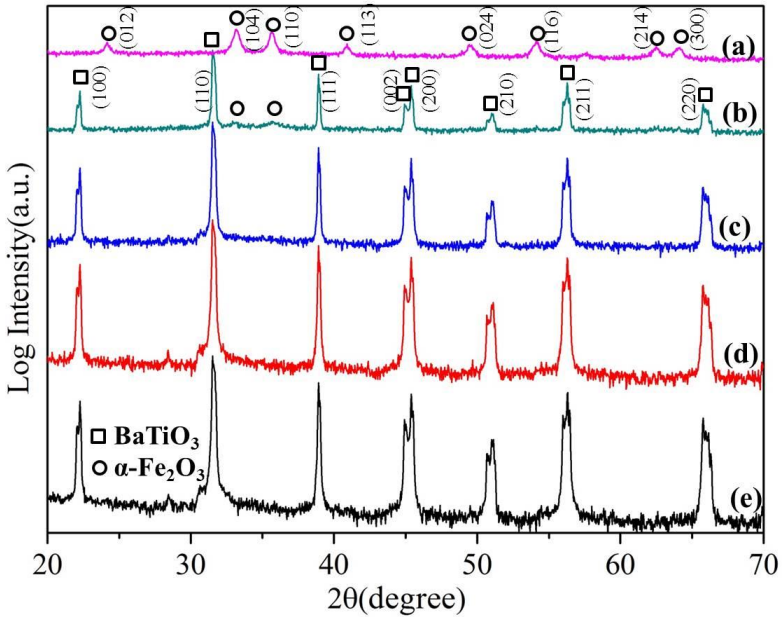

Figure 7.3 XRD patterns of BTO-anneal-Fe_2O_3 and pure α-Fe_2O_3 (a). (b) to (e) represent BTO-anneal-Fe_2O_3-0.5M, BTO-anneal-Fe_2O_3-0.1M, BTO-anneal-Fe_2O_3-0.01M and BTO-anneal-Fe_2O_3-0.001M respectively. The characteristic peaks of tetragonal BTO and α-Fe_2O_3 overlapped in the synthesised heterostructured BTO-anneal-Fe_2O_3-0.5M.

The surface composition and chemical states of elements were analysed by XPS. The comparison of XPS spectra between bare BTO-anneal and BTO-anneal-Fe_2O_3-0.001M is presented in Figure 7.4. The XPS peaks of elements Ba, Ti and O of these two samples overlapped well except extra signals contributed from Fe element in BTO-anneal-Fe_2O_3-0.001M. The spectrum of Fe 2p was made up of two characteristic peaks, Fe $2p_{1/2}$ at 724.2eV and $2p_{3/2}$ at 710.7 eV. These peak positions were consistent with the reported XPS peak locations of α-Fe_2O_3 within the common variations, between 724.4 and 724.7 eV for Fe $2p_{2/1,}$ between 710.6 eV to 711.2 eV for Fe $2p_{3/2}$[219,221,222]. In addition, there was a satellite peak sitting between the two main peaks, which was considered as another feature of XPS signals from Fe^{3+} in α-Fe_2O_3[219,221,222]. Therefore the existence of characteristic peaks of α-Fe_2O_3 in XPS spectrum was in accordance with XRD results, and further supported the successfully synthesis of heterostructured $BaTiO_3$-anneal/Fe_2O_3.

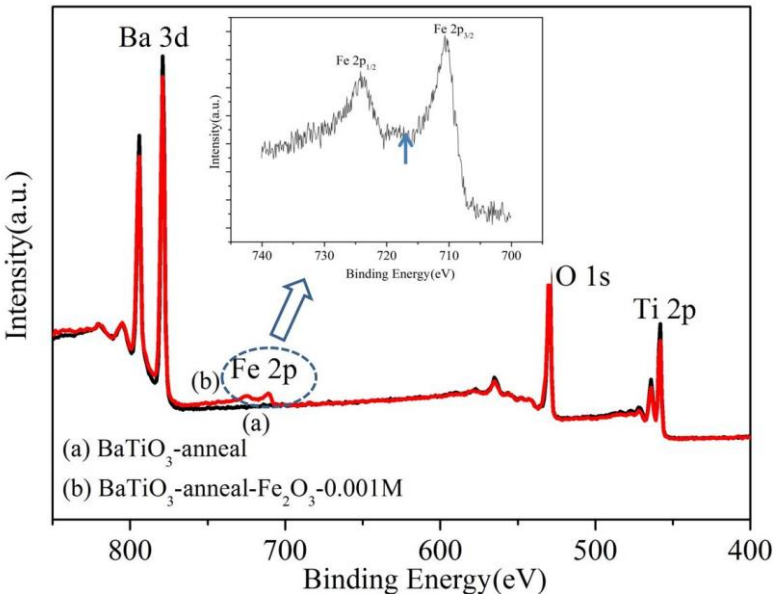

Figure 7.4 XPS spectra of BTO and BTO-anneal-Fe_2O_3-0.001M. Additional characteristic XPS spectrum of α-Fe_2O_3 in BTO-anneal-Fe_2O_3-0.001M confirmed existence of α-Fe_2O_3 on the surface.

The microstructures of heterostructured BTO-anneal-Fe_2O_3 were further investigated by TEM (Figure 7.5). In contrast to the smooth edge of plain $BaTiO_3$-anneal (see Fig. 7.5(a)), some second-phase nanoparticles with an average size below 10 nm formed on the surface of $BaTiO_3$ particles in BTO-anneal-Fe_2O_3-0.001M, as seen Fig. 7.5(b). With the increasing of $Fe(NO_3)_3$ concentration used in synthesis, the loading amount of corresponding synthesised iron species increased. Then these nanoparticles agglomerated and gave rise to a thin layer with thickness vary between 10 nm-25 nm, as seen in BTO-anneal-Fe_2O_3-0.01M (Fig. 7.5(c)). The thickness continues growing for BTO-anneal-Fe_2O_3-0.1M and BTO-anneal-Fe_2O_3-0.5M, and the thickness were measured to be around 45 nm and 84 nm (Fig. 7.5(d) and (e)). Here it should be mentioned that the thickness of the second phase was not uniform and varied, especially for the samples with high loading amount. The thickness was measured choosing different area and particles, and then averaged.

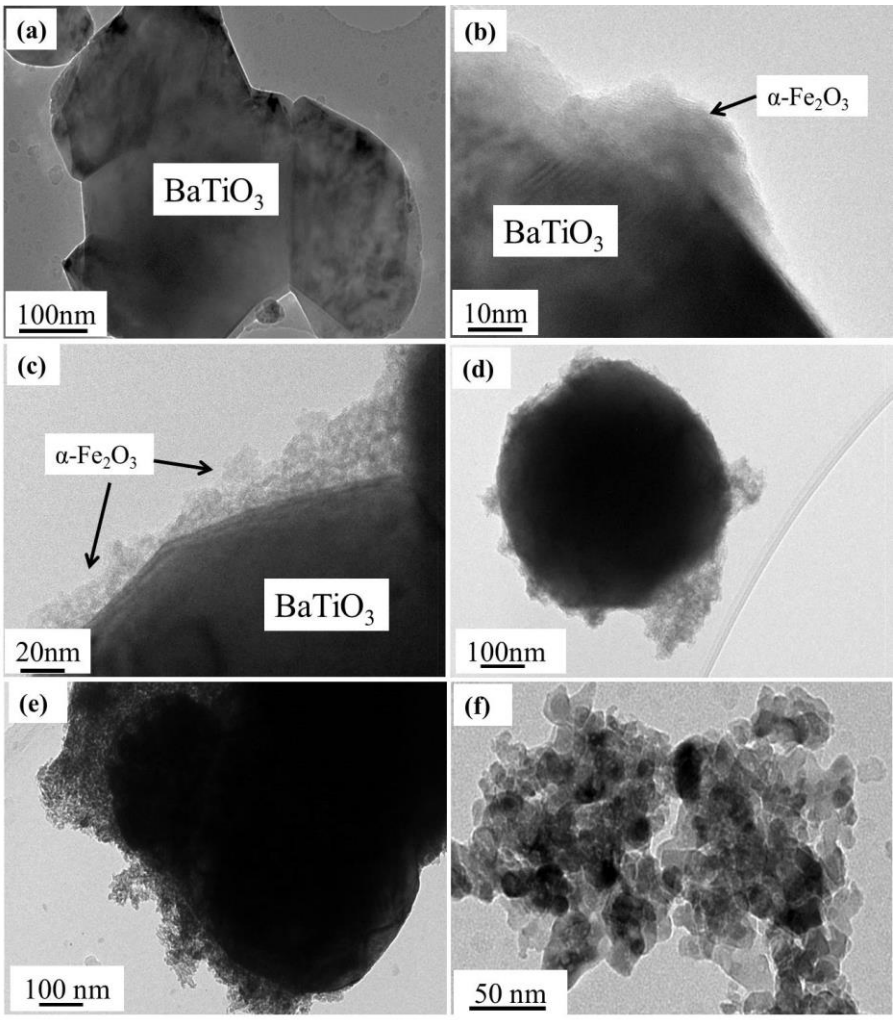

Figure 7.5 TEM micrographs of (a) bare BTO-anneal, (b) BTO-anneal-Fe_2O_3-0.001M, (c) BTO-anneal-Fe_2O_3-0.01M, (d) BTO-anneal-Fe_2O_3-0.1M, (e) BTO-anneal-Fe_2O_3-0.5M and (f) pure Fe_2O_3. The conjunction between BTO-anneal and Fe_2O_3 was observed.

The chemical composition of this layer was analysed by the attached EDX, and the obtained chemical elements mapping is shown in Figure 7.6. It can be observed that Fe element was distributed surrounding the core, where Ba and Ti were detected as expected. Considering the obtained XRD, XPS and SEM/EDX results, the iron signal in EDX was regarded to be arising from α-Fe_2O_3. Based on the TEM micrographs, the intimate conjunction between $BaTiO_3$-anneal and α-Fe_2O_3 was formed using the methods adopted.

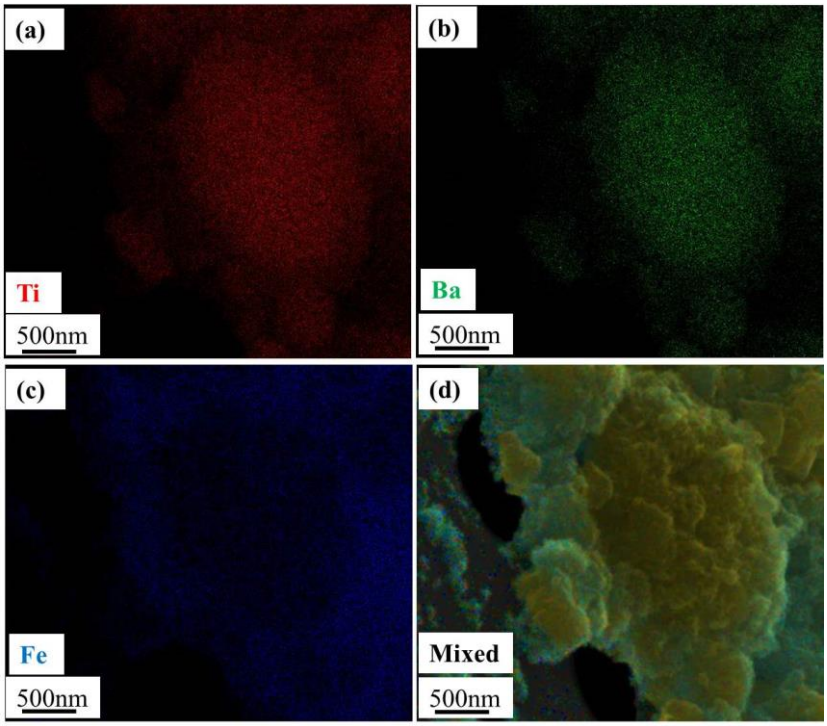

Figure 7.6 EDX mapping of BTO-anneal-Fe_2O_3-0.5M. Fe element was distributed homogeneously around Ti and Ba, showing the heterogeneous structure of BTO-anneal-Fe_2O_3.

The optical properties of synthesised photocatalysts were investigated and the UV-Vis diffuse reflectance absorption spectra are shown in Figure 7.7. As expected, the absorption intensity of heterostructured BTO-anneal-Fe_2O_3 in the visible-light range increased compared with bare BTO due to the surface loading of Fe_2O_3, which has a narrow band gap and can absorb most of the visible light[154]. And this tendency became more apparent along with increase of Fe_2O_3 quantity. The visible-light-harvesting enhancement in BTO-anneal-Fe_2O_3 heterostructured photocatalysts will potentially contribute to modify the overall photocatalytic activity, which will be discussed below in detail. Moreover, a gradual shape change of the absorption spectra can be seen. An absorption onset around 400 nm which was related to the absorption by the core BTO-anneal can be observed in the samples with low mass ratio of Fe_2O_3 (BTO-anneal-Fe_2O_3-0.001M and 0.01M). In contrast, it disappeared in the other two heterostructured samples, and only the absorption spectra which were similar to pure Fe_2O_3 were obtained. This

indicated that the main photon-absorption species changed from core BTO-anneal to shell Fe_2O_3 with increasing quantity of surface loaded Fe_2O_3. This change can potentially affect the overall photocatalytic efficiency, which will be illustrated further below.

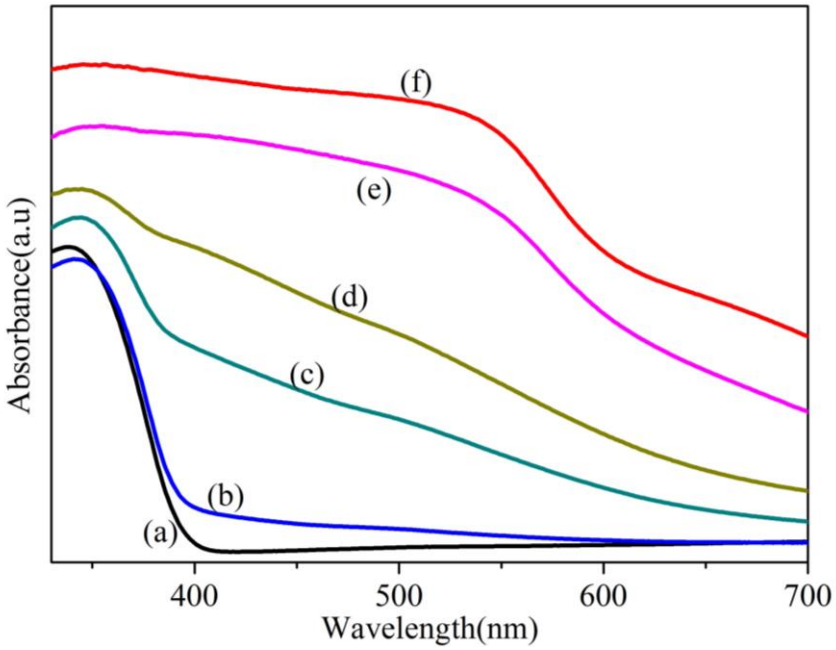

Figure 7.7 Diffuse reflectance spectra of heterostrcutured BTO-anneal-Fe_2O_3, BTO-anneal (a) and Fe_2O_3(f). (b) to (e) represent BTO-anneal-Fe_2O_3-0.001M, BTO-anneal-Fe_2O_3-0.01M, BTO-anneal-Fe_2O_3-0.1M and BTO-anneal-Fe_2O_3-0.5M respectively. With the increasing loading of Fe_2O_3, an enhancement in visible-light range was observed.

7.2 Photocatalytic activity assessment

The photocatalytic activities of these photocatalysts were assessed through photodecolourisation of a target dye molecule – Rhodamine B under solar light. Figure 7.8 shows the degradation profiles of these photocatalysts, and it can be observed that BTO-anneal-Fe_2O_3-0.001M shows the highest decolourisation efficiency. All the data points adopted were averaged from three parallel experiments.

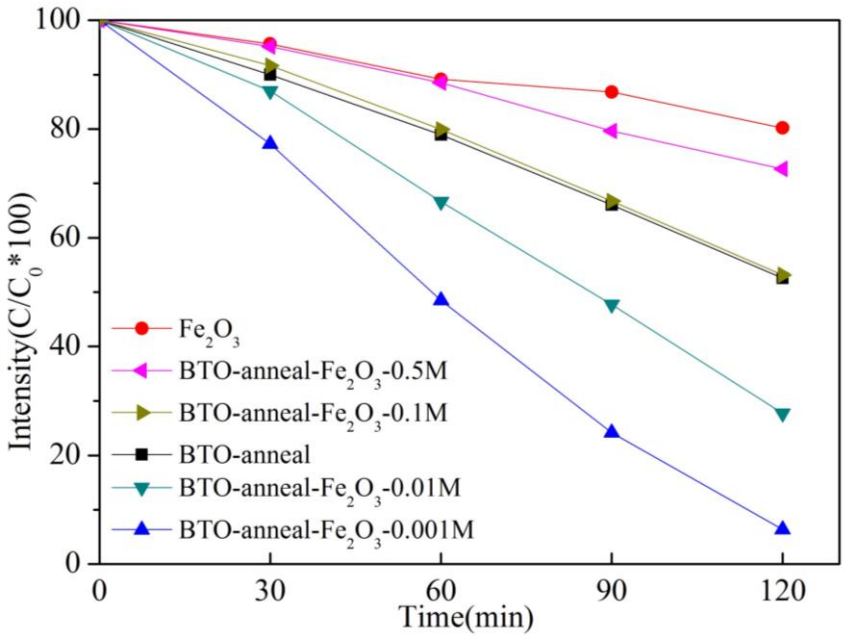

Figure 7.8 Photodecolourisation profiles of RhB with different photocatalysts under solar simulator. Heterostructured BTO-anneal-Fe_2O_3-0.001M showed the best photocatalytic activity.

As seen in Figure 7.8, the kinetics of photodecolourisation of RhB using the synthesised photocatalysts follows the zero-order rate law[223,224], which can be expressed as follows:

$$C_0 - C_t = kt \tag{7.1}$$

The reaction rate k can be obtained from the slop of $C_0 - C_t$ vs. t. The linear fitted results were presented in Figure 7.9, and the obtained reaction rate was shown in Figure 7.10.

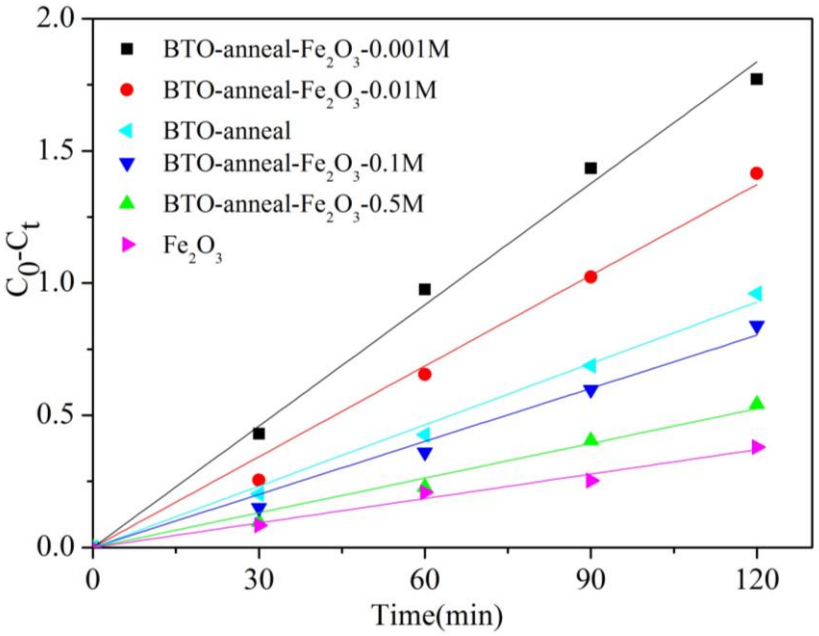

Figure 7.9 Linear fitted function relationship of C_0-C_t versus t

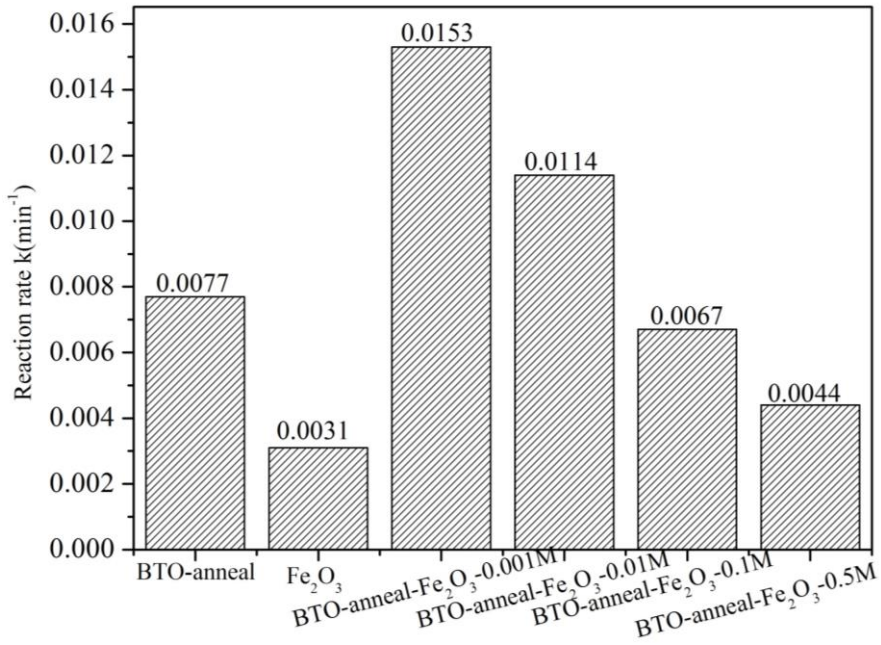

Figure 7.10 The calculated reaction rates of different photocataltsts. BTO-anneal-Fe_2O_3-0.001M showed a faster reaction rate than its single components. However, this enhancement deteriorated along with increasing of Fe_2O_3 loading.

There were two main effects that can be observed by comparing the reaction rate for the different catalysts. The first effect was that after the combination of $BaTiO_3$-anneal with

Fe_2O_3, the heterostructured photocatalysts (BTO-anneal-Fe_2O_3-0.001M and BTO-anneal-Fe_2O_3-0.01M) showed improved photocatalytic activity when compared to their single components. The maximum reaction rate was obtained in BTO-anneal-Fe_2O_3-0.001M, and it was about two-fold and five-fold higher than bare $BaTiO_3$-anneal and Fe_2O_3 respectively. The other effect observed was that the enhancement in photocatalytic activity arising from heterostructure deteroriated along with the increase of Fe_2O_3 amount. As for BTO-anneal-Fe_2O_3-0.5M wherein the mass percentage of Fe_2O_3 is about 44%, the photodecolourisation rate was close to the pure Fe_2O_3. The mechanisms associated with these phenomena will be discussed.

With respect to the reason accounting for the improved photocatalytic performance of heterostructured BTO-anneal-Fe_2O_3, there were three possible factors which will be discussed next one by one. The first is the morphology changes of photocatalysts. Due to the surface modification with Fe_2O_3 nanoparticles, the morphologies of these particulate photocatalysts changed, and accordingly the surface area changed as well (Table 7.1), which normally has a positive correlation with photocatalytic efficiency[223]. With the increasing of loading amount of Fe_2O_3, the BET surface areas of these particulates became larger as well, increasing from below $1 m^2/g$ for BTO-anneal-Fe_2O_3-0.001M to over 23 m^2/g for BTO-anneal-Fe_2O_3-0.1M. Large surface areas can provide more active reaction sites on the surface, and assist the overall photocatalytic reactions.

In order to exclude the effect of surface area on the degradation reaction, the reaction rates of different photocatalysts obtained in Fig. 7.10 were divided by their individual surface areas to get the reaction rate under equal active sites (Figure 7.11). It can be seen that after excluding the potential influence of surface area, the fastest reaction rate obtained in BTO-anneal-Fe_2O_3-0.001M was 2.5 times and over 530 times faster than bare BTO-anneal and Fe_2O_3 respectively. The optimum photocatalytic activity was obtained

in the sample BTO-anneal-Fe_2O_3-0.001M, whose surface area was the smallest among all the four BTO-anneal-Fe_2O_3 photocatalysts and similar to bare BTO-anneal. The opposite trend of photocatalytic rate and BET surface area indicated that surface area was not the main role contributing to the higher photoreaction rate.

Table 7.1 Surface areas of different photocatalysts

Catalysts	BTO-anneal	Fe_2O_3	BTO-anneal-Fe_2O_3-0.001M	BTO-anneal-Fe_2O_3-0.01M	BTO-anneal-Fe_2O_3-0.1M	BTO-anneal-Fe_2O_3-0.5M
Surface area(m^2/g)	0.862	72.1731	0.6622	2.8524	23.371	48.1755

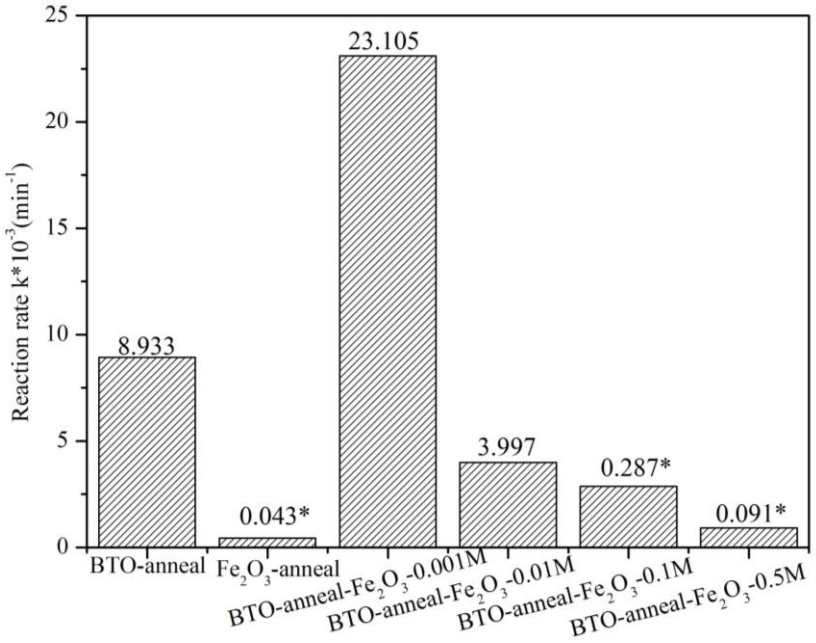

Figure 7.11 The calculated reaction rates of different photocatalysts (scaled by surface area of each sample). * It should be mentioned that the bars which represented Fe_2O_3, BTO-anneal-Fe_2O_3-0.1M and 0.5M were amplified by 10 times.

The second possible factor is the improved visible-light harvesting after coupling with narrow-band-gap Fe_2O_3 (Figure 7.7). In order to confirm whether the enhanced visible-light absorption influences the overall photocatalytic performance, photodecolourisation

of RhB with the best photocatalyst, BTO-anneal-Fe_2O_3-0.001M and bare BTO-anneal under visible light were carried out (See Figure 7.12). No significant discrepancies were observed between these two photocatalysts, and minor dye decolourisation was obtained when only visible light was employed (UV was blocked). This phenomenon was somewhat surprising as the photocatalysts did show an enhanced absorption in visible-light range after coupling with Fe_2O_3 according to the UV-Vis spectra. However, it was reckoned reasonable considering the low mass ratio of Fe_2O_3 in the heterostructured photocatalyst (0.16% for BTO-anneal-Fe_2O_3-0.001M). Therefore, it can be concluded that increasing visible-light absorption was not the main reason for the optimum photocatalytic performance of BTO-anneal-Fe_2O_3 under solar light irradiation. It was the charge carriers generated in BTO-anneal that mainly involve in photodegradation.

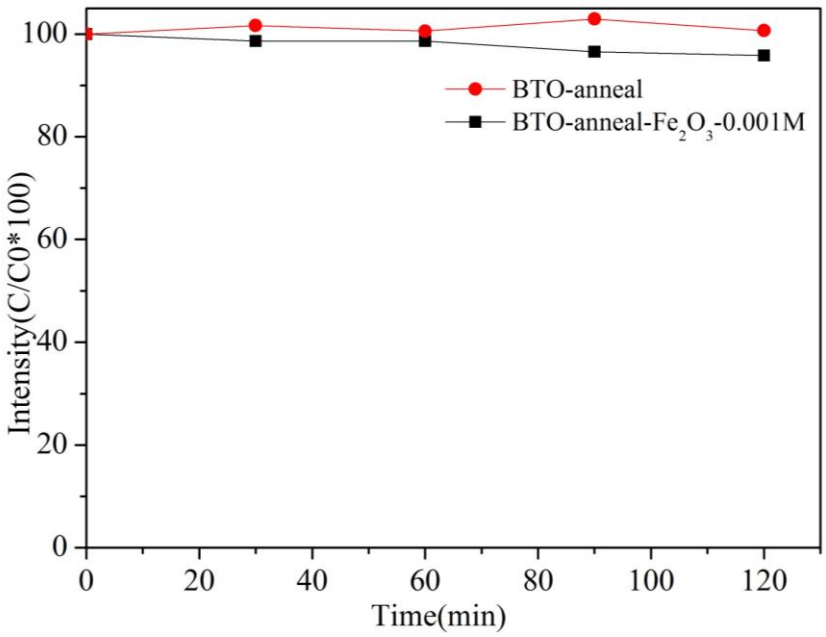

Figure 7.12 Photodecolourisation profiles of RhB with BTO-anneal and BTO-anneal--Fe_2O_3-0.001M under visible light. No significant discrepancy was observed.

The third possible reason is the band-gap configuration in the composited photocatalysts. The band position of $BaTiO_3$-anneal and Fe_2O_3 at the point of zero charge and their Fermi level were shown in Figure 7.13 (a). Here the specific conduction band positions of

$BaTiO_3$-anneal and α-Fe_2O_3 were determined based on the empirical formula[208,209], which has been presented in Chapter 6, Equation 6.1. $E_{CB} = X - E^e - 0.5E_g$, X is the electronegativity of the semiconductor, E^e is the energy of free electrons on the hydrogen scale (about 4.5 eV), and E_g is the band gap energy of the semiconductor. The band positions of $BaTiO_3$-anneal were adopted the values obtained in Chapter 5. The band gap of Fe_2O_3 was assumed to be 2.2 eV[145,219]. Then the conduction band edge of Fe_2O_3 was calculated to be at 0.29 eV versus NHE. Accordingly the valence band positions were at 2.49 eV. As for the Fermi level position of n-type $BaTiO_3$, it was assumed to be 0.1 eV lower than the conduction band edge[143,145]. A work function of α-Fe_2O_3 as 5.4 eV[225] was used to situate its Fermi level relative to the vacuum level, i.e. 0.61 eV below its conduction band edge.

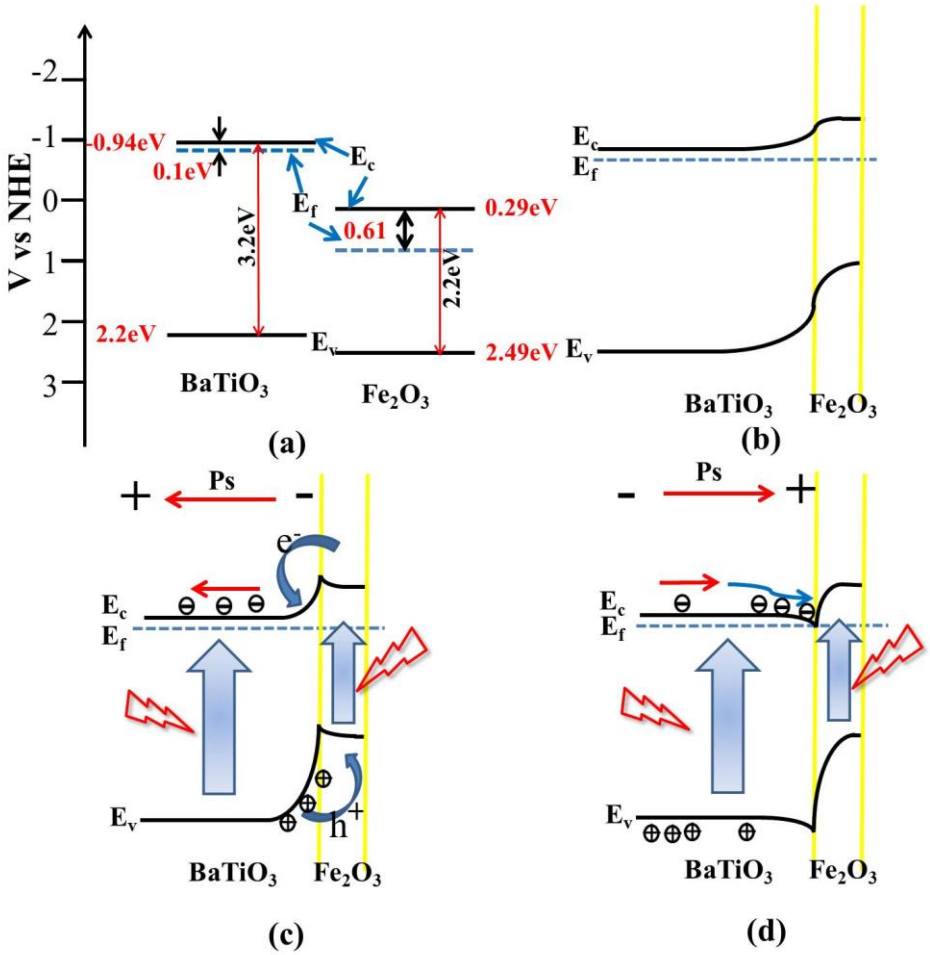

Figure 7.13 (a) Band positions and Fermi level of independent $BaTiO_3$-anneal and Fe_2O_3, (b) (c) and(d) Schematic of band configuration after BTO-anneal and Fe_2O_3 coupled together with (b) no polarisation,(c) negative polarisation and (d) positive polarisation respectively.

When two semiconductors contacted with each other, electrons will flow from the material with a higher Fermi level to that with a lower Fermi level to achieve Fermi level alignment[226]. This will result in the formation of space charge region and band bending near the interface. In our case, electrons will flow from $BaTiO_3$-anneal to Fe_2O_3, and band bend upward in $BaTiO_3$-anneal side and downwards in the other side, as indicated in Figure 7.13(b). It should be mentioned that in addition to the band bending arising from heterojunction, the ferroelectricity of $BaTiO_3$-anneal can also influence band bending[91], and Figure 7.13(b) presents the band structure without polarisation.

According to the models of ferroelectric/semiconductor heterostruture proposed by Watanabe[227,228], the band bending contributed from polarisation of ferroelectric $BaTiO_3$ will counteract or superimpose the band bending due to heterojunction, depending on the polarisation directions. Take negative polarisation as an example (Figure 7.13(c)), the negative charge will cause holes accumulation near the interface. The holes accumulation will increase the band bending upwards in $BaTiO_3$-anneal. With respective to Fe_2O_3, the hole accumulation will decrease the initial downwards band bending or even result in upwards bending (Figure 7.13(c)) if the band bending contributed from polarisation exceeds that from heterojunction. As for positive polarisation (Figure 7.13(d)), the opposite situation can be applied.

Based on the energy band diagram proposed (Figure 7.13(c) and (d)), the photocatalytic performance of heterostructured BTO-anneal-Fe_2O_3 will be discussed. In the case of negative polarisation (Figure 7.13(c)), when under solar light irradiation, the internal field in BTO-anneal will drive separation of charge carriers and holes will accumulate in the interface. Due to the discrepancies in the position of conduction and valence band between BTO-anneal and Fe_2O_3, the charge carriers can be easily separated and transferred between the two components. Holes can be easily transferred to the valence band of Fe_2O_3 while electrons transferred to the conduction band of BTO-anneal, followed by the redox reactions. Therefore, the improved charge carriers separation accounts for the improved photocatalytic performance.

In the case of positive polarisation (Figure 7.13(d)), photoexcited electrons in BTO-anneal will accumulate near the interface. In order to involve in the reduction reactions, these electrons need to overcome the barriers or tunnel through Fe_2O_3 layer or have contact with dye solution directly. It has been reported that the surface reactions on a thin layer of TiO_2 can be influenced by the polarisation of underlying $BaTiO_3$ substrate, and

this was attributed to the electrons generated in $BaTiO_3$ tunnelling through TiO_2 thin layer and involving in photoreactions[61,62]. The similar statement was proposed for $BaTiO_3/TiO_2$ and $PbTiO_3/TiO_2$ core-shell photocatalysts [144,145]. However, the effective electron mass of hematite is heavy, which results its low conductivity and limited photocatalytic applications[229,230]. This property can influence the probability of electrons tunnelling through Fe_2O_3 layer, which was calculated below by using the method reported [231,232], see Figure 7.14. The probability for electrons to tunnel through is negligible even for a thickness of 1 nm. This implies that the tunnel through mechanism is not the main way for electrons generated in BTO-anneal to have reactions with dye solutions.

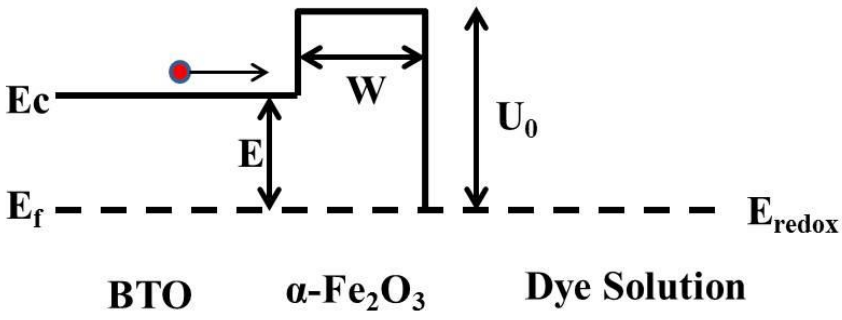

Figure 7.14 Schematic showing the model adopted to calculate the probability for one electron in BTO-anneal to tunnel through α-Fe_2O_3 layer with a thickness of W. E and U_0 are the difference between the conduction band potential and Fermi level after equilibrium achieved between heterostructured photocatalyst and dye solution. $P \approx \frac{16E(U_0 - E)}{U_0^{\,2}} \exp(-2\sqrt{\frac{2m^*(U_0 - E)}{\hbar^2}}W)$ **, Where m* is the effective electron mass of α-Fe_2O_3, herein it was taken as $10m_e$ [228]. For a width of 1 nm, the probability was calculated to be 2×10^{-10}, which indicated that the tunnelling through mechanism was limited for electrons to have reactions with dye solution.**

Considering the optimum photocatalytic activity obtained in BTO-anneal-Fe_2O_3-0.001M, wherein the coupled Fe_2O_3 nanoparticles exist in the form of island-like instead of thin layer, it was considered that the three phase boundaries between $BaTiO_3$-anneal, Fe_2O_3 and dye solutions was critical for high photodegradation rate. The phase boundaries can provide active sites for electrons/holes accumulated in the interface to participate in redox

reactions. Along with increasing loading quantity of Fe_2O_3, the three phase boundaries became rare, which will hinder the redox reactions, and account for the lower photocatalytic activity in samples with higher mass ratio of Fe_2O_3 .

As discussed above, the limited active site due to lack of three phase boundaries in the samples with a thick layer of Fe_2O_3 accounts for the deterioration of photocatalytic activity. Another possible reason is the switch of photon-absorption centre from BTO-anneal to Fe_2O_3, supported by the UV-Vis absorption spectra (See Figure 7.7). The increasing thickness of Fe_2O_3 shell will absorb most of photons due to its optical absorption from near UV to near IR[233], and therefore less light can penetrate and excite ferroelectric core $BaTiO_3$. Therefore, the observed photodegradation rate for the samples with thick layer of Fe_2O_3 was more or less similar to the pure Fe_2O_3 (See Figure 7.10).

Overall, based on the discussion above, it can be concluded that the enhanced photocatalytic activity obtained in the heterostructure was mainly related to the improved charge carriers separation due to the surface decoration with α-Fe_2O_3. Meanwhile, the direct contact between BTO-anneal, Fe_2O_3 and dye solution was important to maintain the high photodegradation rate.

Another phenomenon which should be mentioned is that it can be expected that the polarisation of BTO-anneal influence the charge carries behaviours in the attached Fe_2O_3. In positive polarisation, electrons will move towards the interface while holes accumulated near the interface in the case of negative polarisations. The efficient separation can hinder recombination and extend the charge carrier lifetime of Fe_2O_3. The similar statement about the effect of ferroelectric polarisation on the charge carries in the contacted semiconductor was reported[234], where the built-in electric field of BTO nanocrystal can separate the photo-induced charge carriers of surface-attached Ag_2O.

Furthermore, the chemical stability of heterostructured BTO-anneal-Fe_2O_3 was investigated through recycling the photocatalysts after several runs of photodecolourisations (Figure 7.15). No significant deterioration in photocatalytic activity of BTO-anneal-Fe_2O_3-0.001M was observed after three times of recycling, indicating a good photochemical stability of the synthesised photocatalyst. Moreover, the comparison of XRD patterns between photocatalysts before and after three times usage showed minor changes in the phase composition (Figure 7.16), supporting the good recyclability of heterostructured BTO-anneal-Fe_2O_3 photocatalysts.

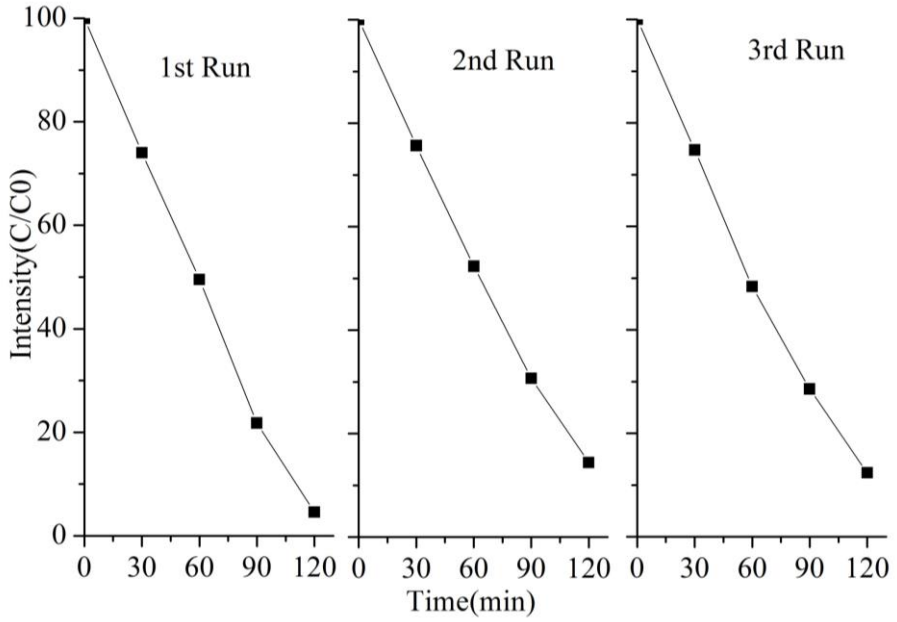

Figure 7.15 Photodecolourisation profiles of RhB using heterostructured BTO-anneal-Fe_2O_3-0.001M under solar simulator in the recycling reactions. The minor change in the decolourisation percentage after three recycles indicated good photocatatytic stability.

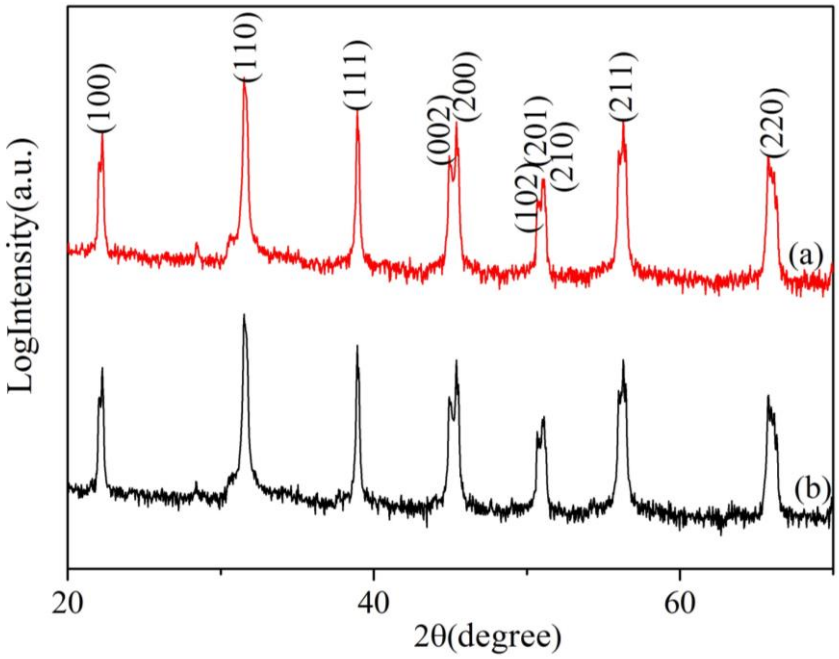

Figure 7.16 XRD patterns of BTO-anneal-Fe_2O_3-0.001M (a) before photodecolourisation reactions and (b) after photodecolourisation reactions. Minor changes were observed, indicating a good stability of photocatalyst.

7.3 Summary

In this chapter, the influence of ferroelectric dipole of $BaTiO_3$-anneal on the photocatalytic activity of heterostructured $BaTiO_3$-anneal-α-Fe_2O_3 was investigated. The heterostructured photocatalysts $BaTiO_3$-anneal-α-Fe_2O_3 with different mass ratio of Fe_2O_3 were successfully synthesised supported by XRD, SEM/EDX, TEM/EDX and XPS analysis.

The optimum photocatalytic activity was obtained in $BaTiO_3$-anneal-Fe_2O_3-0.001M, and its photodecolourisation rate of RhB dye under solar light was two times and five times that of pure $BaTiO_3$-anneal and Fe_2O_3 respectively. The improved photocatalytic performance was attributed to the combined effective photon absorption in BTO-anneal and efficient charge carrier separation in the interface due to heterojunction band alignment. Meanwhile, it was found that the direct contact between $BaTiO_3$-anneal, Fe_2O_3 and dye solution was essential for the high photodegradation rate. The three phase

boundaries provide active sites for charge carriers accumulated in the interface to take part in the redox reactions. With increasing of loading quantity of Fe_2O_3, the enhancement in photocatalytic activity deteriorated due to the lack of active site and the prohibited photon-absorption of BTO-anneal due to the existence of thick Fe_2O_3 layer. In addition, the ferroelectric polarisation of $BaTiO_3$-anneal can be expected to facilitate charge carrier separation and extend charge carrier lifetime in the attached semiconductor Fe_2O_3.

Furthermore, good photocatalytic stability of heterostructured photocatalysts was demonstrated in the recycling test. In summary, heterojunction between ferroelectric photocatalyst $BaTiO_3$-anneal with built-in electric field and semiconductor α-Fe_2O_3 provides a new strategy to manipulate the charge carrier separation, and to design efficient photocatalysts.

Chapter 8

Summary, conclusions and future work

8.1 Summary and conclusions

The aim of this project was to investigate the photocatalytic activity of ferroelectric barium titanate in degradation of organic dye molecules and to demonstrate its promising applications in semiconductor photocatalysis. Based on the former reported surface photochemistry properties of ferroelectric materials, the hypothesis was proposed that ferroelectrics, i.e. photocatalysts with internal field should possess priority in semiconductor photocatalysis due to the inhibited charge carrier recombination arising from depolarisation field. Barium titanate was chosen as the research object and photodecolourisation of organic dyes was performed to assess the photocatalytic activity.

The first stage was to surface decorate as-received $BaTiO_3$ with nanostructured Ag particles through photodeposition method and to investigate the effect of photodeposition time, pH of initial dye solution on the photoactivity. Metallic Ag nanoparticles were successfully loaded onto the surface of $BaTiO_3$ and the surface decoration by the noble metal nanoparticles was shown to enhance the photocatalytic efficiency. This improvement was attributed to the facile electron transport from $BaTiO_3$ to Ag nanoparticles on the surface and inhibited recombination. However, the enhancement was optimum at the photodeposition time of 30 seconds. Along with the increase of photodepostion time, the size and quantity of Ag nanoparticles increased as well while the photocatalytic performance deteriorated. The exceed loading Ag nanoparticles can act as hole traps, enhancing recombination and/or blocking the surface active sites for redox reactions proceed. Therefore, photodeposition for 30 seconds was determined to apply for other studies in this project.

After comparison of photodecolourisation profiles in different pH conditions, it was concluded that Ag-BTO-30s showed the highest potodecolourisation rate under acid conditions, despite of a lowest adsorption of RhB in dark conditions for 30 mins. This illustrated that dye adsorption was not the rate-determining steps in the overall process. The multiple roles of pH, e.g. modifying the surface charge of photocatalysts and generation of various reactive radicals account for the inconsistent between adsorption and overall photodecolourisation rate. Moreover, the main reactive species generated during phorodecolourisation process were determined through adding in scavengers. According to the phenomenon that the reaction rate dropped after adding in the hydroxyl radical scavenger – ethanol, hydroxyl radicals were claimed to be the main active species in the process.

The second stage was to probe into the influence of ferroelectricity of BTO on its photocatalytic activity through direct comparison between non-ferroelectric cubic BTO and ferroelectric tetragonal BTO. A simple thermal treatment was carried out to drive phase transformation and provided a direct way to study the effect of ferroelectricity. X-ray diffraction demonstrated the ferroelectric tetragonal phase increased from 8% in pre-anneal sample to 33% in post-anneal sample. Ag nanoparticle deposition was performed to improve the activity further.

It was found that ferroelectric BTO adsorbed more RhB molecules compare with non-ferroelectric BTO, which was attributed to the surface bound charge and external screening effect in ferroelectric materials. With respect to the photodecolourisation performance, Ag-BTO-anneal, which contains more ferroelectric phase, showed the highest photodecolourisation rate. This phenomenon was relate to the spatial separation of electron-hole pairs due to ferroelectricity, and reduced recombination between charge carriers. The enhancement of Ag loading effect was more obvious in ferroelectric BTO-

anneal. This was regarded to be due to the preferential location of Ag nanoparticles on C+ regions where excessive electrons were available.

The third stage was to further investigate the potential effect of ferroelectricity on the mechanism and pathways of photodegradation of RhB in our ferroelectric catalyst system. By comparing the photodegradation profiles with Ag-BTO-anneal under different irradiation conditions, it was found that photoassisted degradation due to visible light hardly contribute to the overall degradation and only photocatalytic degradation existed. This was considered to be related to the band bending in ferroelectric BTO and the resultant barriers between the photocatalysts and dye molecules, which prohibited the electron-injection from dye molecules to the conduction band of BTO.

According to the change of UV-Vis absorption spectra and ^{1}H NMR spectra with the irradiation time, it was concluded that the cleavage of the chromophore structure of RhB dominated over deethylation in the initial stage of degradation due to a slight hypsochromic wavelength shift. This was related to the degradation mechanism, where only photocatalytic degradation contributed and less likely selectively attacking the alkylamine group. Furthermore, the intermediates produced in the degradation process in Ag-BTO-anneal system was also monitored by GC-MS and determined to be mainly benzoic acid. Overall, there is no significant change in degradation pathways and intermediates in our ferroelectric photocatalyst system compared to non-ferroelectric TiO_2 system.

The photocatalytic activity of heterostructured BTO-anneal-Fe_2O_3 was studied by coupling ferroelectric BTO with non-ferroelectric semiconductor α-Fe_2O_3. The optimum photocatalytic activity was obtained in BTO-anneal-Fe_2O_3-0.001M, which presented a photodegradation rate two times and five times higher than pure $BaTiO_3$-anneal and

Fe_2O_3 respectively. The enhancement was mainly attributed to the improved charge carriers separation due to the band offset between BTO-anneal and Fe_2O_3. However, the morphology control on the interface was important and the three phase boundaries between BTO-anneal, Fe_2O_3 and dye solution was required to provide active site for photodegradation reactions. In addition, the interaction between the dipole of ferroelectric BTO and hematite can facilitate charge carrier separation and extend charge carrier lifetime. Moreover, the good chemical stability of heterogeneous photocatalysts was also demonstrated.

In conclusion, ferroelectric barium titanate was demonstrated its advantage in photodecolourisation of organic dye molecules due to the enhanced charge carrier separation arising from its built-in electric field. In addition, it was found that the photocatalytic activity of baritum titanate can be improved through noble-metal-decoration and heterojunction. Moreover, it was shown that the polarisation of ferroelectric barium titanate can be utilized to influence the motion of charge carriers in the adjacent semiconductor. These findings meet the objectives of this project, and contribute to the understanding of ferroelectric materials in the application of semiconductor photocatalysis. The hypothesis proposed in the beginning of this project, i.e. ferroelectric barium titanate did show superiority in photocolourisation of organic dyes, was demonstrated through this study. Overall, this project provides a new strategy to improve the photocatalytic efficiency, i.e. utilizing the internal electric field of ferroelectric material to enhance charge carriers separation, and opens a new window for designing efficient photocatalysts in the future.

8.2 Future work

In this section, a range of future research areas which continue the work carried out in this project is suggested. These include:

- Investigation of $BaTiO_3$ thin film. The object of study in this project is $BaTiO_3$ powder provided by Sigma-Aldrich. Due to its powder form, its polarisation is arbitrary and it is not so easy to control its polarisation as thin films, which can be polarised to have C+, as-received, and C- surfaces using atomic force microscopy (AFM)[49]. Then the effect of surfaces with different polarisation directions on its photocatalytic activity can be investigated systematically by exposing thin films under super-band gap irradiation. In addition, the form of thin film provides a convenient way to study its photoelectrochemical properties, e.g. photocurrent, flat band potential etc. which can provides more deep understanding about the ferroelectric materials. However, it should be noted that from the point of an efficient semiconductor photocatalyst, the particulate system possesses a bigger surface area and more reactive sites for photochemical reactions than thin film system.
- Size and morphology control of $BaTiO_3$. As mentioned in the former point, $BaTiO_3$ powder used in this work is provided by the company, and its average particle size is around 400 nm and surface area only 2 m^2/g. Therefore, there are still spaces for improvement to obtain a smaller size and bigger surface area, which normally benefit for efficient photocatalysts. Moreover, in addition to nanoparticles, other nano-morphologies of ferroelectric $BaTiO_3$ have been reported[26], such as nanotube, nanowire. These nanostructures in other semiconductor systems have been regarded to be able to facilitate charge carrier transport while maintain a big surface area[14]. Therefore, application of these nanostructures on ferroelectric $BaTiO_3$ could be intriguing future work. But it should be considered the size effect of ferroelectric materials when reducing the size of $BaTiO_3$.

- Band gap engineering of $BaTiO_3$. Due to the large band gap of $BaTiO_3$, it shows low photoactivity under visible light irradiation. Searching for an efficient photocatalyst which can perform photocatalytic reactions effectively under visible light is becoming a hot spot in this research area. Therefore, band gap engineering which have been widely adopted for other semiconductor systems can be performed on ferroelectric $BaTiO_3$ to enhance its visible-light-harvesting. It should be noted that band gap engineering through doping can induce impurities into ferroelectric materials, and change its carrier density, which may influence its internal screening. Then the effected polarisation will impact on its photocatalytic activity. This should be taken into account during doping in ferroelectric materials.
- Surface modification of $BaTiO_3$ by two cocatalysts. In this work, only noble metal silver nanoparticles are photodeposited on $BaTiO_3$, and Ag nanoparticles act as electron trap to further enhance carrier separation. Meanwhile, some metal oxides, e.g. IrO_2, RuO_2, etc. are proved to be able to promote oxidation[235]. Therefore, it could be interesting to have both electron traps and hole traps on the surface of $BaTiO_3$, which can potentially enhance the photocatalytic activity further.
- Water splitting and photoreduction of carbon dioxide. Water purification, i.e. organic dye degradation is the main target of this project. The photocatalytic activity is assessed by photodecolourisation of organic dye. Actually, the potential application of ferroelectric photocatalysis can be extended to other areas, such as water splitting and photoreduction of carbon dioxide. Then the influence of ferroelectricity of $BaTiO_3$ on its efficiency in H_2 and/or O_2 production can be investigated.

These studies were not carried out in this project due to the time restrictions. In addition, the studies on ferroelectric thin films and other applications of semiconductor photocatalysis are beyond the research scope of this project, which mainly focus on the water purification/ organic dye degradation with ferroelectric barium titanate powder.

References

1. Ong, S.-T., Keng, P.-S., Lee, W.-N., Ha, S.-T. & Hung, Y.-T. Dye Waste Treatment. *Water* **3,** 157–176 (2011).

2. Chen, C., Ma, W. & Zhao, J. Semiconductor-mediated photodegradation of pollutants under visible-light irradiation. *Chem. Soc. Rev.* **39,** 4206–4219 (2010).

3. Konstantinou, I. K. & Albanis, T. A. TiO2-assisted photocatalytic degradation of azo dyes in aqueous solution: kinetic and mechanistic investigations. *Appl. Catal. B Environ.* **49,** 1–14 (2004).

4. Chowdhury, S. & Balasubramanian, R. Graphene/semiconductor nanocomposites (GSNs) for heterogeneous photocatalytic decolorization of wastewaters contaminated with synthetic dyes: A review. *Appl. Catal. B Environ.* **160–161,** 307–324 (2014).

5. Hoffmann, M. R., Martin, S. T., Choi, W. & Bahnemann, D. W. Environmental Applications of Semiconductor Photocatalysis. *Chem. Rev.* **95,** 69–96 (1995).

6. Mills, A., Davies, R. H. & Worsley, D. Water purification by semiconductor photocatalysis. *Chem. Soc. Rev.* **22,** 417–425 (1993).

7. Maeda, K. & Domen, K. New Non-Oxide Photocatalysts Designed for Overall Water Splitting under Visible Light. *J. Phys. Chem. C* **111,** 7851–7861 (2007).

8. Herrmann, J.-M. Heterogeneous photocatalysis: fundamentals and applications to the removal of various types of aqueous pollutants. *Catal. Today* **53,** 115–129 (1999).

9. Mills, A. & Le Hunte, S. An overview of semiconductor photocatalysis. *J. Photochem. Photobiol. A Chem.* **108,** 1–35 (1997).

10. Linsebigler, A. L., Lu, G. & Yates, J. T. Photocatalysis on TiO2 Surfaces: Principles, Mechanisms, and Selected Results. *Chem. Rev.* **95,** 735–758 (1995).

11. Dunn, S. Time to think outside the box. *Mater. Today* **14,** 302 (2011).

12. Qu, Y. & Duan, X. Progress, challenge and perspective of heterogeneous photocatalysts. *Chem. Soc. Rev.* **42,** 2568–2580 (2013).

13. Xiaobo Chen Liejin Guo,and Samuel S. Mao, S. S. Semiconductor-based Photocatalytic Hydrogen Generation. *Chem. Rev.* **110,** 6503–6570 (2010).

14. Tong, H. *et al.* Nano-photocatalytic Materials: Possibilities and Challenges. *Adv. Mater.* **24,** 229–251 (2012).

15. Scott, J. F. *FerroelectricMemories*. (Springer, 2000).

16. Jaffe, B., Cook, J. M. & Jaffe, H. *Piezoelectric Ceramics*. (Academic Press, 1971).

17. Yang, W. C., Rodriguez, B. J., Gruverman, A. & Nemanich, R. J. Photo electron emission microscopy of polarity-patterned materials. *J. Phys. Condens. Matter* **17,** S1415–S1426 (2005).

18. Giocondi, J. L. & Rohrer, G. S. Spatially Selective Photochemical Reduction of Silver on the Surface of Ferroelectric Barium Titanate. *Chem. Mater.* **13,** 241–242 (2001).

19. Giocondi, J. L. & Rohrer, G. S. Spatial Separation of Photochemical Oxidation and Reduction Reactions on the Surface of Ferroelectric BaTiO3. *J. Phys. Chem. B* **105,** 8275–8277 (2001).

20. Dunn, S., Jones, P. M. & Gallardo, D. E. Photochemical Growth of Silver Nanoparticles on c- and c+ Domains on Lead Zirconate Titanate Thin Films. *J. Am. Chem. Soc.* **129,** 8724–8728 (2007).

21. Kalinin, S. V *et al.* Atomic Polarization and Local Reactivity on Ferroelectric Surfaces: A New Route toward Complex Nanostructures. *Nano Lett.* **2,** 589–593 (2002).

22. Cabrera, A. L., Vargas, F. & Albers, J. J. Adsorption of carbon dioxide by ferroelectric lithium niobate. *Surf. Sci.* **336,** 280–286 (1995).

23. Cabrera, A. L., Vargas, F. & Zarate, R. A. Adsorption of carbon dioxide by barium titanate: Evidence of adsorption process mediated by a dipole-dipole interaction. *J. Phys. Chem. Solids* **55,** 1303–1307 (1994).

24. Xu, Y. *Ferroelectric mateials and their applications*. (North-Holland, 1991).

25. Haertling, G. H. Ferroelectric Ceramics: History and Technology. *J. Am. Ceram. Soc.* **82,** 797–818 (1999).

26. Varghese, J., Whatmore, R. W. & Holmes, J. D. Ferroelectric nanoparticles, wires and tubes: synthesis, characterisation and applications. *J. Mater. Chem. C* **1,** 2618–2638 (2013).

27. Auciello, O., Scott, J. F. & Ramesh, R. The Physics of Ferroelectric Memories. *Phys. Today* **51,** 22–27 (1998).

28. Conklin, D., Park, T.-H., Nanayakkara, S., Therien, M. J. & Bonnell, D. A. Controlling Polarization Dependent Reactions to Fabricate Multi-Component Functional Nanostructures. *Adv. Funct. Mater.* **21,** 4712–4718 (2011).

29. Tiwari, D. & Dunn, S. Photochemistry on a polarisable semi-conductor: what do we understand today? *J. Mater. Sci.* **44,** 5063–5079 (2009).

30. Eng, L. M. Nanoscale domain engineering and characterization of ferroelectric domains. *Nanotechnology* **10,** 405–411 (1999).

31. Landis, C. M. & Sirohi, J. in *Encycl. Aerosp. Eng.* (John Wiley & Sons, Ltd, 2010). doi:10.1002/9780470686652.eae230

32. Zhang, Z. & Yates, J. T. Band Bending in Semiconductors: Chemical and Physical Consequences at Surfaces and Interfaces. *Chem. Rev.* **112,** 5520–5551 (2012).

33. Jones, P. M., Gallardo, D. E. & Dunn, S. Photochemical Investigation of a Polarizable Semiconductor, Lead-Zirconate-Titanate. *Chem. Mater.* **20,** 5901–5906 (2008).

34. Bhardwaj, A., Burbure, N. V, Gamalski, A. & Rohrer, G. S. Composition Dependence of the Photochemical reduction of Ag by Ba1−xSrxTiO3. *Chem. Mater.* **22,** 3527–3534 (2010).

35. Dunn, S. *et al.* Using the surface spontaneous depolarization field of ferroelectrics to direct the assembly of virus particles. *Appl. Phys. Lett.* **85,** 3537 (2004).

36. Hu, Y. Effects of an Inner Helmholtz Layer on the Dielectric Dispersion of Colloidal Suspensions. *Langmuir* **14,** 271–276 (1998).

37. Jones, P. M. & Dunn, S. Interaction of Stern layer and domain structure on photochemistry of lead-zirconate-titanate. *J. Phys. D. Appl. Phys.* **42,** 65408 (2009).

38. Akdogan, E. K., Rawn, C. J., Porter, W. D., Payzant, E. A. & Safari, A. Size effects in PbTiO3 nanocrystals: Effect of particle size on spontaneous polarization and strains. *J. Appl. Phys.* **97,** - (2005).

39. Ishikawa, K., Yoshikawa, K. & Okada, N. Size effect on the ferroelectric phase transition in PbTiO3 ultrafine particles. *Phys. Rev. B* **37,** 5852–5855 (1988).

40. Zhao, Z. *et al.* Grain-size effects on the ferroelectric behavior of dense nanocrystalline BaTiO3 ceramics. *Phys. Rev. B* **70,** 24107 (2004).

41. Li, X. & Shih, W.-H. Size Effects in Barium Titanate Particles and Clusters. *J. Am. Ceram. Soc.* **80,** 2844–2852 (1997).

42. Uchino, K., Sadanaga, E. & Hirose, T. Dependence of the Crystal Structure on Particle Size in Barium Titanate. *J. Am. Ceram. Soc.* **72,** 1555–1558 (1989).

43. Yen, F. S., Hsiang, H. I. & Chang, Y. H. Cubic to tetragonal phase transformation of ultrafine BaTiO?3? crystallites at room temperature. *Jpn. J. Appl. Phys.* **34,** 6149–6155 (1995).

44. Nuraje, N. & Su, K. Perovskite ferroelectric nanomaterials. *Nanoscale* **5,** 8752–8780 (2013).

45. Shih, W. Y., Shih, W.-H. & Aksay, I. A. Size dependence of the ferroelectric transition of small BaTiO3 particles: Effect of depolarization. *Phys. Rev. B* **50,** 15575–15585 (1994).

46. Frey, M. H. & Payne, D. A. Grain-size effect on structure and phase transformations for barium titanate. *Phys. Rev. B* **54,** 3158–3168 (1996).

47. Gruverman, A. & Kholkin, A. Nanoscale ferroelectrics: processing, characterization and future trends. *Reports Prog. Phys.* **69,** 2443 (2006).

48. Dunn, S., Jones, P. M. & Gallardo, D. E. Photochemical Growth of Silver Nanoparticles on c- and c+ Domains on Lead Zirconate Titanate Thin Films. *J. Am. Chem. Soc.* **129,** 8724–8728 (2007).

49. Tiwari, D., Dunn, S. & Zhang, Q. Impact of Zr/Ti ratio in the PZT on the photoreduction of silver nanoparticles. *Mater. Res. Bull.* **44,** 1219–1224 (2009).

50. Dunn, S., Tiwari, D., Jones, P. M. & Gallardo, D. E. Insights into the relationship between inherent materials properties of PZT and photochemistry for the development of nanostructured silver. *J. Mater. Chem.* **17,** 4460 (2007).

51. Jones, P. M. & Dunn, S. Photo-reduction of silver salts on highly heterogeneous lead zirconate titanate. *Nanotechnology* **18,** 185702 (2007).

52. Xiaoyan Liu, Kenji Kitamura, Kazuya Terabe, H. H. and N. O. Photocatalytic nanoparticle deposition on LiNbO3 nanodomain patterns via photovoltaic effect. *Appl. Phys. Lett.* **91,** 44101 (2007).

53. Tiwari, D. & Dunn, S. Photochemical reduction of Al3 + to Al0 over a ferroelectric photocatalyst — LiNbO3. *Mater. Lett.* **79,** 18–20 (2012).

54. Sun, Y. & Nemanich, R. J. Photoinduced Ag deposition on periodically poled lithium niobate: Wavelength and polarization screening dependence. *J. Appl. Phys.* **109,** 104302–104307 (2011).

55. Sun, Y., Eller, B. S. & Nemanich, R. J. Photo-induced Ag deposition on periodically poled lithium niobate: Concentration and intensity dependence. *J. Appl. Phys.* **110,** 84303–84307 (2011).

56. Kim, S., Schoenberg, M. R. & Rappe, A. M. Polarization-dependence of palladium deposition on ferroelectric lithium niobate (0001) surfaces. *Phys. Rev. Lett.* **107,** 1–5 (2011).

57. Dunn, S. & Tiwari, D. Influence of ferroelectricity on the photoelectric effect of LiNbO[sub 3]. *Appl. Phys. Lett.* **93,** 92905 (2008).

58. Schultz, A. M., Zhang, Y., Salvador, P. A. & Rohrer, G. S. Effect of Crystal and Domain Orientation on the Visible-Light Photochemical Reduction of Ag on BiFeO3. *ACS Appl. Mater. Interfaces* **3,** 1562–1567 (2011).

59. Habicht, S., Nemanich, R. J. & Gruverman, A. Physical adsorption on ferroelectric surfaces: photoinduced and thermal effects. *Nanotechnology* **19,** 495303 (2008).

60. Burbure, N. V., Salvador, P. A. & Rohrer, G. S. Influence of Dipolar Fields on the Photochemical Reactivity of Thin Titania Films on BaTiO3 Substrates. *J. Am. Ceram. Soc.* **89,** 2943–2945 (2006).

61. Burbure, N. V, Salvador, P. A. & Rohrer, G. S. Photochemical Reactivity of Titania Films on BaTiO3 Substrates: Origin of Spatial Selectivity. *Chem. Mater.* **22,** 5823–5830 (2010).

62. Burbure, N. V., Salvador, P. A. & Rohrer, G. S. Photochemical Reactivity of Titania Films on BaTiO 3 Substrates: Influence of Titania Phase and Orientation. *Chem. Mater.* **22,** 5831–5837 (2010).

63. Zhang, Y., Schultz, A. M., Salvador, P. A. & Rohrer, G. S. Spatially selective visible light photocatalytic activity of TiO2/BiFeO3 heterostructures. *J. Mater. Chem.* **21,** 4168–4174 (2011).

64. Kalinin, S. V. *et al.* Ferroelectric Lithography of Multicomponent Nanostructures. *Adv. Mater.* **16,** 795–799 (2004).

65. Li, D. & Bonnell, D. A. Ferroelectric lithography. *Ceram. Int.* **34,** 157–164 (2008).

66. Yun, Y., Kampschulte, L., Li, M., Liao, D. & Altman, E. I. Effect of Ferroelectric Poling on the Adsorption of 2-Propanol on LiNbO3(0001). *J. Phys. Chem. C* **111,** 13951–13956 (2007).

67. Yun, Y. & Altman, E. I. Using Ferroelectric Poling to Change Adsorption on Oxide Surfaces. *J. Am. Chem. Soc.* **129,** 15684–15689 (2007).

68. Li, D. *et al.* Direct in situ determination of the polarization dependence of physisorption on ferroelectric surfaces. *Nat. Mater.* **7,** 473–477 (2008).

69. Zhao, M. H., Bonnell, D. A. & Vohs, J. M. Effect of ferroelectric polarization on the adsorption and reaction of ethanol on BaTiO3. *Surf. Sci.* **602,** 2849–2855 (2008).

70. Zhao, M. H., Bonnell, D. A. & Vohs, J. M. Influence of ferroelectric polarization on the energetics of the reaction of 2-fluoroethanol on BaTiO3. *Surf. Sci.* **603,** 284–290 (2009).

71. Garra, J., Vohs, J. M. & Bonnell, D. A. The effect of ferroelectric polarization on the interaction of water and methanol with the surface of LiNbO3(0 0 0 1). *Surf. Sci.* **603,** 1106–1114 (2009).

72. Sanna, S., Hölscher, R. & Schmidt, W. G. Polarization-dependent water adsorption on the LiNbO3(0001) surface. *Phys. Rev. B* **86,** 205407 (2012).

73. Inoue, Y., Yoshioka, I. & Sato, K. Polarization effects upon adsorptive and catalytic properties. 1. Carbon monoxide oxidation over palladium deposited on lithium niobate (LiNbO3) ferroelectrics. *J. Phys. Chem.* **88,** 1148–1151 (1984).

74. Watanabe, Y., Okano, M. & Masuda, A. Surface Conduction on Insulating BaTiO3 Crystal Suggesting an Intrinsic Surface Electron Layer. *Phys. Rev. Lett.* **86,** 332–335 (2001).

75. Inoue, Y., Sato, K. & Suzuki, S. Polarization effects upon adsorptive and catalytic properties. 2. Surface electrical conductivity of nickel(II) oxide deposited on lithium niobate (LiNbO3) and its changes upon gas adsorption. *J. Phys. Chem.* **89,** 2827–2831 (1985).

76. Yang, W. C., Rodriguez, B. J., Gruverman, A. & Nemanich, R. J. Polarization-dependent electron affinity of LiNbO[sub 3] surfaces. *Appl. Phys. Lett.* **85,** 2316–2318 (2004).

77. Hooton, J. A. & Merz, W. J. Etch Patterns and Ferroelectric Domains in BaTi{\mathrm{O}}_{3} Single Crystals. *Phys. Rev.* **98,** 409–413 (1955).

78. Nassau, K., Levinstein, H. J. & Loiacono, G. M. THE DOMAIN STRUCTURE AND ETCHING OF FERROELECTRIC LITHIUM NIOBATE. *Appl. Phys. Lett.* **6,** (1965).

79. Sones, C. L., Mailis, S., Brocklesby, W. S., Eason, R. W. & Owen, J. R. Differential etch rates in z-cut LiNbO3 for variable HF/HNO3 concentrations. *J. Mater. Chem.* **12,** 295–298 (2002).

80. Garrity, K., Kolpak, A. M., Ismail-Beigi, S. & Altman, E. I. Chemistry of Ferroelectric Surfaces. *Adv. Mater.* **22,** 2969–2973 (2010).

81. Fujishima, A. & Honda, K. Electrochemical Photolysis of Water at a Semiconductor Electrode. *Nature* **238,** 37–38 (1972).

82. Kudo, A. & Miseki, Y. Heterogeneous photocatalyst materials for water splitting. *Chem. Soc. Rev.* **38,** 253 (2009).

83. Kudo, A. Development of photocatalyst materials for water splitting. *Int. J. Hydrogen Energy* **31,** 197–202 (2006).

84. Mao, J., Li, K. & Peng, T. Recent advances in the photocatalytic CO2 reduction over semiconductors. *Catal. Sci. Technol.* **3,** 2481–2498 (2013).

85. Roy, S. C., Varghese, O. K., Paulose, M. & Grimes, C. A. Toward Solar Fuels: Photocatalytic Conversion of Carbon Dioxide to Hydrocarbons. *ACS Nano* **4,** 1259–1278 (2010).

86. Marszewski, M., Cao, S., Yu, J. & Jaroniec, M. Semiconductor-based photocatalytic CO2 conversion. *Mater. Horiz.* - (2015). doi:10.1039/C4MH00176A

87. Chen, D. & K. Ray, A. Removal of toxic metal ions from wastewater by semiconductor photocatalysis. *Chem. Eng. Sci.* **56,** 1561–1570 (2001).

88. Peral, J., Domenech, X. & Ollis, D. F. Heterogeneous photocatalysis for purification, decontamination and deodorization of air. *J. Chem. Technol. Biotechnol.* **70,** 117–140 (1997).

89. Zhao, J. & Yang, X. D. Photocatalytic oxidation for indoor air purification: a literature review. *Build. Environ.* **38,** 645–654 (2003).

90. Gaya, U. I. & Abdullah, A. H. Heterogeneous photocatalytic degradation of organic contaminants over titanium dioxide: A review of fundamentals, progress and problems. *J. Photochem. Photobiol. C Photochem. Rev.* **9,** 1–12 (2008).

91. Li, L., Salvador, P. A. & Rohrer, G. S. Photocatalysts with internal electric fields. *Nanoscale* (2013). doi:10.1039/C3NR03998F

92. Zhang, Z., Wang, C.-C., Zakaria, R. & Ying, J. Y. Role of Particle Size in Nanocrystalline TiO2-Based Photocatalysts. *J. Phys. Chem. B* **102,** 10871–10878 (1998).

93. Beydoun, D., Amal, R., Low, G. & McEvoy, S. Role of Nanoparticles in Photocatalysis. *J. Nanoparticle Res.* **1,** 439–458 (1999).

94. Bi, Y., Ouyang, S., Umezawa, N., Cao, J. & Ye, J. Facet Effect of Single-Crystalline Ag3PO4 Sub-microcrystals on Photocatalytic Properties. *J. Am. Chem. Soc.* **133,** 6490–6492 (2011).

95. Selloni, A. Crystal growth: Anatase shows its reactive side. *Nat Mater* **7,** 613–615 (2008).

96. Anpo, M. The design and development of highly reactive titanium oxide photocatalysts operating under visible light irradiation. *J. Catal.* **216,** 505–516 (2003).

97. Choi, W., Termin, A. & Hoffmann, M. R. The Role of Metal Ion Dopants in Quantum-Sized TiO2: Correlation between Photoreactivity and Charge Carrier Recombination Dynamics. *J. Phys. Chem.* **98,** 13669–13679 (1994).

98. Ni, M., Leung, M. K. H., Leung, D. Y. C. & Sumathy, K. A review and recent developments in photocatalytic water-splitting using for hydrogen production. *Renew. Sustain. Energy Rev.* **11,** 401–425 (2007).

99. Maeda, K. Photocatalytic water splitting using semiconductor particles: History and recent developments. *J. Photochem. Photobiol. C Photochem. Rev.* **12,** 237–268 (2011).

100. Fox, M. A. & Dulay, M. T. Heterogeneous photocatalysis. *Chem. Rev.* **93,** 341–357 (1993).

101. Chen, X. & Burda, C. The Electronic Origin of the Visible-Light Absorption Properties of C-, N- and S-Doped TiO2 Nanomaterials. *J. Am. Chem. Soc.* **130,** 5018–5019 (2008).

102. Asahi, R. Visible-Light Photocatalysis in Nitrogen-Doped Titanium Oxides. *Science (80-.).* **293,** 269–271 (2001).

103. Hitoki, G. *et al.* An oxynitride{,} TaON{,} as an efficient water oxidation photocatalyst under visible light irradiation ([small lambda] [less-than-or-equal] 500 nm). *Chem. Commun.* 1698–1699 (2002). doi:10.1039/B202393H

104. Min Ji, S. *et al.* Photocatalytic hydrogen production from water-methanol mixtures using N-doped Sr2Nb2O7 under visible light irradiation: effects of catalyst structure. *Phys. Chem. Chem. Phys.* **7,** 1315–1321 (2005).

105. Sakthivel, S. *et al.* Enhancement of photocatalytic activity by metal deposition: characterisation and photonic efficiency of Pt, Au and Pd deposited on TiO2 catalyst. *Water Res.* **38,** 3001–3008 (2004).

106. Liu, S. X., Qu, Z. P., Han, X. W. & Sun, C. L. A mechanism for enhanced photocatalytic activity of silver-loaded titanium dioxide. *Catal. Today* **93–95,** 877–884 (2004).

107. Rupa, A. V., Manikandan, D., Divakar, D. & Sivakumar, T. Effect of deposition of Ag on TiO2 nanoparticles on the photodegradation of Reactive Yellow-17. *J. Hazard. Mater.* **147,** 906–913 (2007).

108. Linic, S., Christopher, P. & Ingram, D. B. Plasmonic-metal nanostructures for efficient conversion of solar to chemical energy. *Nat. Mater.* **10,** 911–21 (2011).

109. Wang, P., Huang, B., Dai, Y. & Whangbo, M.-H. Plasmonic photocatalysts: harvesting visible light with noble metal nanoparticles. *Phys. Chem. Chem. Phys.* **14,** 9813–25 (2012).

110. Kowalska, E., Mahaney, O. O. P., Abe, R. & Ohtani, B. Visible-light-induced photocatalysis through surface plasmon excitation of gold on titania surfaces. *Phys. Chem. Chem. Phys.* **12,** 2344–2355 (2010).

111. Baker, D. R. & Kamat, P. V. Photosensitization of TiO2 Nanostructures with CdS Quantum Dots: Particulate versus Tubular Support Architectures. *Adv. Funct. Mater.* **19,** 805–811 (2009).

112. Domen, K., Naito, S., Soma, M., Onishi, T. & Tamaru, K. Photocatalytic decomposition of water vapour on an NiO-SrTiO3 catalyst. *J. Chem. Soc.{,} Chem. Commun.* 543–544 (1980). doi:10.1039/C39800000543

113. Kadowaki, H. *et al.* Overall Splitting of Water by RuO2-Loaded PbWO4 Photocatalyst with d10s2-d0 Configuration. *J. Phys. Chem. C* **111,** 439–444 (2006).

114. Ma, B. *et al.* Enhancement of Photocatalytic Water Oxidation Activity on IrOx−ZnO/Zn2−xGeO4−x−3yN2y Catalyst with the Solid Solution Phase Junction. *J. Phys. Chem. C* **114,** 12818–12822 (2010).

115. Maeda, K. & Domen, K. Photocatalytic Water Splitting: Recent Progress and Future Challenges. *J. Phys. Chem. Lett.* **1,** 2655–2661 (2010).

116. Kim, H. G. *et al.* Fabrication of CaFe2O4/MgFe2O4 bulk heterojunction for enhanced visible light photocatalysis. *Chem. Commun.* 5889–5891 (2009). doi:10.1039/B911805E

117. Sivula, K. *et al.* Photoelectrochemical Water Splitting with Mesoporous Hematite Prepared by a Solution-Based Colloidal Approach. *J. Am. Chem. Soc.* **132,** 7436–7444 (2010).

118. Li, H. *et al.* Mesoporous Au/TiO2 Nanocomposites with Enhanced Photocatalytic Activity. *J. Am. Chem. Soc.* **129,** 4538–4539 (2007).

119. Takahara, Y., Kondo, J. N., Takata, T., Lu, D. & Domen, K. Mesoporous Tantalum Oxide. 1. Characterization and Photocatalytic Activity for the Overall Water Decomposition. *Chem. Mater.* **13,** 1194–1199 (2001).

120. Liu, J., Sun, Y. & Li, Z. Ag loaded flower-like BaTiO3 nanotube arrays: Fabrication and enhanced photocatalytic property. *CrystEngComm* **14,** 1473–1478 (2012).

121. Cao, J., Ji, Y., Tian, C. & Yi, Z. Synthesis and enhancement of visible light activities of nitrogen-doped BaTiO3. *J. Alloys Compd.* **615,** 243–248 (2014).

122. Li, Z., Yu, T., Zou, Z. & Ye, J. Degradation in photocatalytic activity induced by hydrogen-related defects in nano-LiNbO3 material. *Appl. Phys. Lett.* **88,** 071917 (2006).

123. Gao, F. *et al.* Visible-Light Photocatalytic Properties of Weak Magnetic BiFeO3 Nanoparticles. *Adv. Mater.* **19,** 2889–2892 (2007).

124. Li, S., Lin, Y.-H., Zhang, B.-P., Nan, C.-W. & Wang, Y. Photocatalytic and magnetic behaviors observed in nanostructured BiFeO3 particles. *J. Appl. Phys.* **105,** 56105 (2009).

125. Cho, C. M. *et al.* Low-Temperature Hydrothermal Synthesis of Pure BiFeO3 Nanopowders Using Triethanolamine and Their Applications as Visible-Light Photocatalysts. *J. Am. Ceram. Soc.* **91,** 3753–3755 (2008).

126. Xian, T. *et al.* Photocatalytic properties of BiFeO3 nanoparticles with different sizes. *Mater. Lett.* **65,** 1573–1575 (2011).

127. Inoue, Y., Sato, K., Sato, K. & Miyama, H. Photoassisted water decomposition by ferroelectric lead zirconate titanate ceramics with anomalous photovoltaic effects. *J. Phys. Chem.* **90,** 2809–2810 (1986).

128. Inoue, Y., Sato, K. & Sato, K. Photovoltaic and photocatalytic behaviour of a ferroelectric semiconductor, lead strontium zirconate titanate, with a polarization axis perpendicular to the surface. *J. Chem. Soc. Faraday Trans. 1 Phys. Chem. Condens. Phases* **85,** 1765–1774 (1989).

129. Inoue, Y., Hayashi, O. & Sato, K. Photocatalytic activities of potassium-doped lead niobates and the effect of poling. *J. Chem. Soc. Faraday Trans.* **86,** 2277–2282 (1990).

130. Bhardwaj, A., Burbure, N. V & Rohrer, G. S. Enhanced Photochemical Reactivity at the Ferroelectric Phase Transition in Ba1−xSrxTiO3. *J. Am. Ceram. Soc.* **93,** 4129–4134 (2010).

131. Guo, R., Fang, L., Dong, W., Zheng, F. & Shen, M. Enhanced Photocatalytic Activity and Ferromagnetism in Gd Doped BiFeO3 Nanoparticles. *J. Phys. Chem. C* **114,** 21390–21396 (2010).

132. Nath, R. K., Zain, M. F. M., Kadhum, A. A. H. & Kaish, A. B. M. A. An investigation of LiNbO3 photocatalyst coating on concrete surface for improving indoor air quality. *Constr. Build. Mater.* **54,** 348–353 (2014).

133. Stock, M. & Dunn, S. Influence of the Ferroelectric Nature of Lithium Niobate to Drive Photocatalytic Dye Decolorization under Artificial Solar Light. *J. Phys. Chem. C* **116,** 20854–20859 (2012).

134. Stock, M. & Dunn, S. LiNbO3—A Polar Material for Solid-Gas Artificial Photosynthesis. *Ferroelectrics* **419,** 9–13 (2011).

135. Stock, M. & Dunn, S. LiNbO3- A new material for artificial photosynthesis. *Ultrason. Ferroelectr. Freq. Control. IEEE Trans.* **58,** 1988–1993 (2011).

136. Park, S. *et al.* A ferroelectric photocatalyst for enhancing hydrogen evolution: polarized particulate suspension. *Phys. Chem. Chem. Phys.* **16,** 10408–10413 (2014).

137. Fan, X. *et al.* A Bulk Boron-Based Photocatalyst for Efficient Dechlorination: K3B6O10Br. *Chem. Mater.* (2014). doi:10.1021/cm500597e

138. Inoue, Y., Okamura, M. & Sato, K. A thin-film semiconducting titanium dioxide combined with ferroelectrics for photoassisted water decomposition. *J. Phys. Chem.* **89,** 5184–5187 (1985).

139. Inoue, Y., Sato, K., Sato, K. & Miyama, H. A device type photocatalyst using oppositely polarized ferroelectric substrates. *Chem. Phys. Lett.* **129,** 79–81 (1986).

140. Li, S., Lin, Y.-H., Zhang, B.-P., Li, J.-F. & Nan, C.-W. BiFeO3/TiO2core-shell structured nanocomposites as visible-active photocatalysts and their optical response mechanism. *J. Appl. Phys.* **105,** 54310 (2009).

141. Zhu, A., Zhao, Q., Li, X. & Shi, Y. BiFeO3/TiO2 Nanotube Arrays Composite Electrode: Construction, Characterization, and Enhanced Photoelectrochemical Properties. *ACS Appl. Mater. Interfaces* **6,** 671–679 (2013).

142. Huang, H. *et al.* Efficient Photocatalytic Activity of PZT/TiO2 Heterojunction under Visible Light Irradiation. *J. Phys. Chem. C* **113,** 14264–14269 (2009).

143. Li, L., Liu, X., Zhang, Y., Salvador, P. A. & Rohrer, G. S. Heterostructured (Ba,Sr)TiO3/TiO2 core/shell photocatalysts: Influence of processing and structure on hydrogen production. *Int. J. Hydrogen Energy* **38,** 6948–6959 (2013).

144. Li, L. *et al.* Visible light photochemical activity of heterostructured PbTiO3-TiO2 core-shell particles. *Catal. Sci. Technol.* **2,** 1945–1952 (2012).

145. Li, L., Rohrer, G. S. & Salvador, P. A. Heterostructured Ceramic Powders for Photocatalytic Hydrogen Production: Nanostructured TiO2 Shells Surrounding Microcrystalline (Ba,Sr)TiO3 Cores. *J. Am. Ceram. Soc.* **95,** 1414–1420 (2012).

146. Vijatović, M. M., Bobić, J. D. & Stojanović, B. D. History and Challenges of Barium Titanate: Part I. *Sci. Sinter.* **40,** 155–165 (2008).

147. Jona, F. & Shirane, G. *Ferroelectric crystals*. (Pergamon Press, 1962). at <http://books.google.co.uk/books?id=TKEsAAAAYAAJ>

148. Zhong, W., Vanderbilt, D. & Rabe, K. M. Phase Transitions in BaTiO3 from First Principles. *Phys. Rev. Lett.* **73,** 1861–1864 (1994).

149. Suzuki, K. & Kijima, K. Optical Band Gap of Barium Titanate Nanoparticles Prepared by RF-plasma Chemical Vapor Deposition. *Jpn. J. Appl. Phys.* **44,** 2081–2082 (2005).

150. Vijatović, M. M., Bobić, J. D. & Stojanović, B. D. History and challenges of barium titanate: Part II. *Sci. Sinter.* **40,** 235–244 (2008).

151. Klein, S. a, Wilk, S. J., Thornton, T. J. & Posner, J. D. Formation of nanopores in suspended lipid bilayers using quantum dots. *J. Phys. Conf. Ser.* **109,** 012022 (2008).

152. https://www.emdmillipore.com/US/en/product/Rhodamine-B-%28C.I.45170%29,MDA_CHEM-107599.

153. Zhou, W. *et al.* Mesoporous TiO2/α-Fe2O3: Bifunctional Composites for Effective Elimination of Arsenite Contamination through Simultaneous Photocatalytic Oxidation and Adsorption. *J. Phys. Chem. C* **112,** 19584–19589 (2008).

154. Peng, L., Xie, T., Lu, Y., Fan, H. & Wang, D. Synthesis, photoelectric properties and photocatalytic activity of the Fe2O3/TiO2 heterogeneous photocatalysts. *Phys. Chem. Chem. Phys.* **12,** 8033–8041 (2010).

155. Chang, L.-H., Yeh, Y.-L. & Chen, Y.-W. Preferential oxidation of CO in hydrogen stream over nano-gold catalysts prepared by photodeposition method. *Int. J. Hydrogen Energy* **33,** 1965–1974 (2008).

156. Herrmann, J.-M., Disdier, J. & Pichat, P. Photocatalytic deposition of silver on powder titania: Consequences for the recovery of silver. *J. Catal.* **113,** 72–81 (1988).

157. Chan, S. C. & Barteau, M. A. Preparation of Highly Uniform Ag/TiO2 and Au/TiO2 Supported Nanoparticle Catalysts by Photodeposition. *Langmuir* **21,** 5588–5595 (2005).

158. Smith, W. *et al.* The effect of Ag nanoparticle loading on the photocatalytic activity of TiO2 nanorod arrays. *Chem. Phys. Lett.* **485,** 171–175 (2010).

159. http://srdata.nist.gov/xps/selEnergyType.aspx.

160. Sung-Suh, H. M., Choi, J. R., Hah, H. J., Koo, S. M. & Bae, Y. C. Comparison of Ag deposition effects on the photocatalytic activity of nanoparticulate TiO2 under visible and UV light irradiation. *J. Photochem. Photobiol. A Chem.* **163,** 37–44 (2004).

161. Xiong, Z., Ma, J., Ng, W. J., Waite, T. D. & Zhao, X. S. Silver-modified mesoporous TiO2 photocatalyst for water purification. *Water Res.* **45,** 2095–2103 (2011).

162. He, J., Ichinose, I., Kunitake, T. & Nakao, A. In Situ Synthesis of Noble Metal Nanoparticles in Ultrathin TiO2−Gel Films by a Combination of Ion-Exchange and Reduction Processes. *Langmuir* **18,** 10005–10010 (2002).

163. Lassaletta, G. *et al.* Thermal and photochemical methods for the preparation of thin films of cermet materials. *J. Mater. Sci.* **31,** 2325–2332 (1996).

164. Wen, L., Liu, B., Liu, C. & Zhao, X. Preparation, characterization and photocatalytic property of Ag-loaded TiO2 powders using photodeposition method. *J. Wuhan Univ. Technol. Sci. Ed.* **24,** 258–263 (2009).

165. Zhang, H., Wang, G., Chen, D., Lv, X. & Li, J. Tuning Photoelectrochemical Performances of Ag−TiO2 Nanocomposites via Reduction/Oxidation of Ag. *Chem. Mater.* **20,** 6543–6549 (2008).

166. Vinodgopal, K. & Kamat, P. V. Photochemistry on surfaces: photodegradation of 1,3-diphenylisobenzofuran over metal oxide particles. *J. Phys. Chem.* **96,** 5053–5059 (1992).

167. Li, Y., Lu, G. & Li, S. Photocatalytic transformation of rhodamine B and its effect on hydrogen evolution over Pt/TiO2 in the presence of electron donors. *J. Photochem. Photobiol. A Chem.* **152,** 219–228 (2002).

168. Baran, W., Adamek, E. & Makowski, A. The influence of selected parameters on the photocatalytic degradation of azo-dyes in the presence of TiO2 aqueous suspension. *Chem. Eng. J.* **145,** 242–248 (2008).

169. Awazu, K. *et al.* A plasmonic photocatalyst consisting of silver nanoparticles embedded in titanium dioxide. *J. Am. Chem. Soc.* **130,** 1676–80 (2008).

170. Meng, F. & Sun, Z. A mechanism for enhanced hydrophilicity of silver nanoparticles modified TiO2 thin films deposited by RF magnetron sputtering. *Appl. Surf. Sci.* **255,** 6715–6720 (2009).

171. Liu, X., Yang, Y., Shi, X. & Li, K. Fast photocatalytic degradation of methylene blue dye using a low-power diode laser. *J. Hazard. Mater.* **283,** 267–275 (2015).

172. Khanna, A. & Shetty K, V. Solar photocatalysis for treatment of Acid Yellow-17 (AY-17) dye contaminated water using Ag@TiO2 core–shell structured nanoparticles. *Environ. Sci. Pollut. Res.* **20,** 5692–5707 (2013).

173. Vignesh, K., Hariharan, R., Rajarajan, M. & Suganthi, A. Visible light assisted photocatalytic activity of TiO2–metal vanadate (M=Sr, Ag and Cd) nanocomposites. *Mater. Sci. Semicond. Process.* **16,** 1521–1530 (2013).

174. Chong, M. N., Jin, B., Chow, C. W. K. & Saint, C. Recent developments in photocatalytic water treatment technology: A review. *Water Res.* **44,** 2997–3027 (2010).

175. Muruganandham, M., Sobana, N. & Swaminathan, M. Solar assisted photocatalytic and photochemical degradation of Reactive Black 5. *J. Hazard. Mater.* **137,** 1371–1376 (2006).

176. Sakthivel, S. *et al.* Solar photocatalytic degradation of azo dye: comparison of photocatalytic efficiency of ZnO and TiO2. *Sol. Energy Mater. Sol. Cells* **77,** 65–82 (2003).

177. Akpan, U. G. & Hameed, B. H. Parameters affecting the photocatalytic degradation of dyes using TiO2-based photocatalysts: A review. *J. Hazard. Mater.* **170,** 520–529 (2009).

178. Gonçalves, M. S. T., Oliveira-Campos, A. M. F., Pinto, E. M. M. S., Plasência, P. M. S. & Queiroz, M. J. R. P. Photochemical treatment of solutions of azo dyes containing TiO2. *Chemosphere* **39,** 781–786 (1999).

179. Hayat, K., Gondal, M. A., Khaled, M. M., Yamani, Z. H. & Ahmed, S. Laser induced photocatalytic degradation of hazardous dye (Safranin-O) using self synthesized nanocrystalline WO3. *J. Hazard. Mater.* **186,** 1226–1233 (2011).

180. Li, K. *et al.* Ag–AgBr/CaWO4 composite microsphere as an efficient photocatalyst for degradation of Acid Red 18 under visible light irradiation: Affecting factors, kinetics and mechanism. *J. Mol. Catal. A Chem.* **394,** 105–113 (2014).

181. Daneshvar, N., Salari, D. & Khataee, A. R. Photocatalytic degradation of azo dye acid red 14 in water: investigation of the effect of operational parameters. *J. Photochem. Photobiol. A Chem.* **157,** 111–116 (2003).

182. Du, W., Xu, Y. & Wang, Y. Photoinduced Degradation of Orange II on Different Iron (Hydr)oxides in Aqueous Suspension: Rate Enhancement on Addition of Hydrogen Peroxide, Silver Nitrate, and Sodium Fluoride. *Langmuir* **24,** 175–181 (2008).

183. Šojić, D. V, Anderluh, V. B., Orčić, D. Z. & Abramović, B. F. Photodegradation of clopyralid in TiO2 suspensions: Identification of intermediates and reaction pathways. *J. Hazard. Mater.* **168,** 94–101 (2009).

184. Khodja, A. A., Sehili, T., Pilichowski, J.-F. & Boule, P. Photocatalytic degradation of 2-phenylphenol on TiO2 and ZnO in aqueous suspensions. *J. Photochem. Photobiol. A Chem.* **141,** 231–239 (2001).

185. Bell, A. T. The Impact of Nanoscience on Heterogeneous Catalysis. *Science (80-.).* **299,** 1688–1691 (2003).

186. Kwei, G. H., Lawson, A. C., Billinge, S. J. L. & Cheong, S. W. Structures of the ferroelectric phases of barium titanate. *J. Phys. Chem.* **97,** 2368–2377 (1993).

187. Tanaka, K., Padermpole, K. & Hisanaga, T. Photocatalytic degradation of commercial azo dyes. *Water Res.* **34,** 327–333 (2000).

188. Chun, H., Yizhong, W. & Hongxiao, T. Influence of adsorption on the photodegradation of various dyes using surface bond-conjugated TiO2/SiO2 photocatalyst. *Appl. Catal. B Environ.* **35,** 95–105 (2001).

189. McCafferty, E. & Wightman, J. P. Determination of the concentration of surface hydroxyl groups on metal oxide films by a quantitative XPS method. *Surf. Interface Anal.* **26,** 549–564 (1998).

190. Bickley, R. I., Gonzalez-Carreno, T., Lees, J. S., Palmisano, L. & Tilley, R. J. D. A structural investigation of titanium dioxide photocatalysts. *J. Solid State Chem.* **92,** 178–190 (1991).

191. Wang, X. *et al.* Photocatalytic Overall Water Splitting Promoted by an α–β phase Junction on Ga2O3. *Angew. Chemie Int. Ed.* **51,** 13089–13092 (2012).

192. Koleżyński, A. & Tkacz-Śmiech, K. From the Molecular Picture to the Band Structure of Cubic and Tetragonal Barium Titanate. *Ferroelectrics* **314,** 123–134 (2005).

193. Zhou, H., Qu, Y., Zeid, T. & Duan, X. Towards highly efficient photocatalysts using semiconductor nanoarchitectures. *Energy Environ. Sci.* **5,** 6732 (2012).

194. Yu, K. *et al.* Visible light-driven photocatalytic degradation of rhodamine B over NaBiO3: pathways and mechanism. *J. Phys. Chem. A* **113,** 10024–32 (2009).

195. Fu, H., Zhang, S., Xu, T., Zhu, Y. & Chen, J. Photocatalytic Degradation of RhB by Fluorinated Bi 2 WO 6 and Distributions of the Intermediate Products. *Environ. Sci. Technol.* **42,** 2085–2091 (2008).

196. He, Z. *et al.* Photocatalytic degradation of rhodamine B by Bi(2)WO(6) with electron accepting agent under microwave irradiation: mechanism and pathway. *J. Hazard. Mater.* **162,** 1477–86 (2009).

197. Fu, H., Pan, C., Yao, W. & Zhu, Y. Visible-Light-Induced Degradation of Rhodamine B by Nanosized Bi2WO6. *J. Phys. Chem. B* **109,** 22432–22439 (2005).

198. Luan, J., Ma, K., Li, Y. & Zou, Z. Photophysical and photocatalytic properties of novel Y2GaSbO7 and Y2YbSbO7 photocatalysts under visible light irradiation. *J. Mater. Sci.* **46,** 813–823 (2011).

199. HE, Z., YANG, S., JU, Y. & SUN, C. Microwave photocatalytic degradation of Rhodamine B using TiO2 supported on activated carbon: Mechanism implication. *J. Environ. Sci.* **21,** 268–272 (2009).

200. Chen, F., Zhao, J. & Hidaka, H. Highly selective deethylation of rhodamine B : Adsorption and photooxidation pathways of the dye on the TiO 2 / SiO 2 composite photocatalyst. *Int. J. Photoenergy* **05,** 209–217 (2003).

201. LI, J., MA, W., LEI, P. & ZHAO, J. Detection of intermediates in the TiO2-assisted photodegradation of Rhodamine B under visible light irradiation. *J. Environ. Sci.* **19,** 892–896 (2007).

202. Wu, T., Liu, G., Zhao, J., Hidaka, H. & Serpone, N. Photoassisted Degradation of Dye Pollutants. V. Self-Photosensitized Oxidative Transformation of Rhodamine B under Visible Light Irradiation in Aqueous TiO2 Dispersions. *J. Phys. Chem. B* **102,** 5845–5851 (1998).

203. Wang, Q., Chen, C., Zhao, D., Ma, W. & Zhao, J. Change of adsorption modes of dyes on fluorinated TiO2 and its effect on photocatalytic degradation of dyes under visible irradiation. *Langmuir* **24,** 7338–45 (2008).

204. Li, J. *et al.* Photodegradation of dye pollutants on one-dimensional TiO2 nanoparticles under UV and visible irradiation. *J. Mol. Catal. A Chem.* **261,** 131–138 (2007).

205. Liu, G., Li, X., Zhao, J., Hidaka, H. & Serpone, N. Photooxidation Pathway of Sulforhodamine-B. Dependence on the Adsorption Mode on TiO 2 Exposed to Visible Light Radiation. *Environ. Sci. Technol.* **34,** 3982–3990 (2000).

206. Zhao, J. *et al.* Photoassisted Degradation of Dye Pollutants. 3. Degradation of the Cationic Dye Rhodamine B in Aqueous Anionic Surfactant/TiO2 Dispersions under Visible Light Irradiation: Evidence for the Need of Substrate Adsorption on TiO2 Particles. *Environ. Sci. Technol.* **32,** 2394–2400 (1998).

207. Hashimoto, K., Hiramoto, M. & Sakata, T. Photo-induced electron transfer from adsorbed rhodamine B to oxide semiconductor substrates in vacuo: Semiconductor dependence. *Chem. Phys. Lett.* **148,** 215–220 (1988).

208. Butler, M. A. & Ginley, D. S. Prediction of Flatband Potentials at Semiconductor-Electrolyte Interfaces from Atomic Electronegativities. *J. Electrochem. Soc.* **125,** 228–232 (1978).

209. Kim, Y. Il, Atherton, S. J., Brigham, E. S. & Mallouk, T. E. Sensitized layered metal oxide semiconductor particles for photochemical hydrogen evolution from nonsacrificial electron donors. *J. Phys. Chem.* **97,** 11802–11810 (1993).

210. Butler, M. A. Photoelectrolysis and physical properties of the semiconducting electrode WO3 . *J. Appl. Phys.* **48,** 1914 (1977).

211. Fan, H. *et al.* Photoinduced Charge Transfer Properties and Photocatalytic Activity in Bi2O3/BaTiO3 Composite Photocatalyst. *ACS Appl. Mater. Interfaces* **4,** 4853–4857 (2012).

212. Pearson, R. G. Absolute electronegativity and hardness: application to inorganic chemistry. *Inorg. Chem.* **27,** 734–740 (1988).

213. Xu, Y. & Schoonen, M. A. A. The absolute energy positions of conduction and valence bands of selected semiconducting minerals. *Am. Mineral.* **85,** 534–556 (2000).

214. Fan, Y. *et al.* Highly Selective Deethylation of Rhodamine B on TiO2 Prepared in Supercritical Fluids. *Int. J. Photoenergy* **2012,** 1–7 (2012).

215. Natarajan, T., Natarajan, K., Bajaj, H. & Tayade, R. Enhanced photocatalytic activity of bismuth-doped TiO2 nanotubes under direct sunlight irradiation for degradation of Rhodamine B dye. *J. Nanoparticle Res.* **15,** 1–18 (2013).

216. Stock, M. & Dunn, S. LiNbO3--a new material for artificial photosynthesis. *IEEE Trans. Ultrason. Ferroelectr. Freq. Control* **58,** 1988–93 (2011).

217. Hatch, S. M., Briscoe, J. & Dunn, S. A self-powered ZnO-nanorod/CuSCN UV photodetector exhibiting rapid response. *Adv. Mater.* **25,** 867–71 (2013).

218. Di Paola, A., García-López, E., Marcì, G. & Palmisano, L. A survey of photocatalytic materials for environmental remediation. *J. Hazard. Mater.* **211–212,** 3–29 (2012).

219. Wang, G. *et al.* Facile Synthesis of Highly Photoactive α-Fe2O3-Based Films for Water Oxidation. *Nano Lett.* **11,** 3503–3509 (2011).

220. Moniz, S. J. A., Shevlin, S. A., An, X., Guo, Z.-X. & Tang, J. Fe2O3–TiO2 Nanocomposites for Enhanced Charge Separation and Photocatalytic Activity. *Chem. – A Eur. J.* **20,** 15571–15579 (2014).

221. Guo, Y., Zhang, G., Liu, J. & Zhang, Y. Hierarchically structured [small alpha]-Fe2O3/Bi2WO6 composite for photocatalytic degradation of organic contaminants under visible light irradiation. *RSC Adv.* **3,** 2963–2970 (2013).

222. Yamashita, T. & Hayes, P. Analysis of XPS spectra of Fe2+ and Fe3+ ions in oxide materials. *Appl. Surf. Sci.* **254,** 2441–2449 (2008).

223. Chang, J.-C. *et al.* Chemistry in a confined space: characterization of nitrogen-doped titanium oxide nanotubes produced by calcining ammonium trititanate nanotubes. *J. Mater. Chem.* **21,** 4605–4614 (2011).

224. Sun, S.-P. *et al.* Decolorization of an azo dye Orange G in aqueous solution by Fenton oxidation process: Effect of system parameters and kinetic study. *J. Hazard. Mater.* **161,** 1052–1057 (2009).

225. Fan, Z., Wen, X., Yang, S. & Lu, J. G. Controlled p- and n-type doping of Fe2O3 nanobelt field effect transistors. *Appl. Phys. Lett.* **87,** - (2005).

226. Moniz, S. J. A., Shevlin, S. A., Martin, D. J., Guo, Z.-X. & Tang, J. Visible-light driven heterojunction photocatalysts for water splitting - a critical review. *Energy Environ. Sci.* **8,** 731–759 (2015).

227. Watanabe, Y. Electrical transport through Pb(Zr,Ti)O3 p-n and p-p heterostructures modulated by bound charges at a ferroelectric surface: Ferroelectric p-n diode. *Phys. Rev. B* **59,** 11257–11266 (1999).

228. Watanabe, Y. Energy band diagram of ferroelectric heterostructures and its application to the thermodynamic feasibility of ferroelectric FET. *Solid State Ionics* **108,** 59–65 (1998).

229. Huda, M. N., Walsh, A., Yan, Y., Wei, S.-H. & Al-Jassim, M. M. Electronic, structural, and magnetic effects of 3d transition metals in hematite. *J. Appl. Phys.* **107,** - (2010).

230. Meng, X. *et al.* Theoretical Understanding of Enhanced Photoelectrochemical Catalytic Activity of Sn-Doped Hematite: Anisotropic Catalysis and Effects of Morin Transition and Sn Doping. *J. Phys. Chem. C* **117,** 3779–3784 (2013).

231. Sze, S. M. & Ng, K. K. in *Phys. Semicond. Devices* 415–465 (John Wiley & Sons, Inc., 2006). doi:10.1002/9780470068328.ch8

232. Loh, L., Briscoe, J. & Dunn, S. Enhanced performance with bismuth ferrite perovskite in ZnO nanorod solid state solar cells. *Nanoscale* 7072–7078 (2014). doi:10.1039/c4nr00911h

233. Wheeler, D. A., Wang, G., Ling, Y., Li, Y. & Zhang, J. Z. Nanostructured hematite: synthesis, characterization,charge carrier dynamics, and photoelectrochemical properties. *Energy Environ. Sci.* **5,** 6682–6702 (2012).

234. Li, H. *et al.* Enhanced Ferroelectric-Nanocrystal-Based Hybrid Photocatalysis by Ultrasonic-Wave-Generated Piezophototronic Effect. *Nano Lett.* **15,** 2372–2379 (2015).

235. Wang, D. *et al.* Core/Shell Photocatalyst with Spatially Separated Co-Catalysts for Efficient Reduction and Oxidation of Water. *Angew. Chemie Int. Ed.* **52,** 11252–11256 (2013).

Appendix A—Publications and Presentations

Publications

- **Yongfei Cui,** Joe Briscoe, Steve Dunn, Effect of Ferroelectricity on Solar-Light-Driven Photocatalytic Activity of $BaTiO_3$ –Influence on the Carrier Separation and Stern Layer Formation, ***Chemistry of Materials, 2013, 25, 4215−4223***
- **Yongfei Cui,** Stephen M. Goldup , Steve Dunn, Photodegradation of Rhodamine B over Ag modified ferroelectric $BaTiO_3$ under simulated solar light: pathways and mechanism, ***RSC Advances, 2015, 5，30372-30379***
- **Yongfei Cui,** Joe Briscoe, Steve Dunn, An investigation into the effect of ferroelectricity of $BaTiO_3$ on the photocatalytic activity in dye decolourisation, ***Advances in Science and Technology, 2014, 93, 190-195*** **(Conference Proceeding)**
- **Yongfei Cui,** Joe Briscoe, Steve Dunn, Influence of ferroelectric dipole on the photocatalytic activity of $BaTiO_3$/α-Fe_2O_3, ***Thin Solid Film, Under Review***
- **Yongfei Cui,** Joe Briscoe, Yaqiong Wang, Nadja Tarakina, Steve Dunn, Enhanced photocatalytic activity of ferroelectric $BaTiO_3$/α-Fe_2O_3 heterostructured photocatalyst, ***In preparation***

Presentations

- Effect of Ferroelectricity on Solar-Light-Driven Photocatalytic Activity of $BaTiO_3$ –Influence on the Carrier Separation and Stern Layer Formation, ***The 20th Joint Annual Conference of CSCST-SCI, September 14, 2013, London, UK*** **(Oral Presentation)**
- Effect of Ferroelectricity on Solar-Light-Driven Photocatalytic Activity of $BaTiO_3$ –Influence on the Carrier Separation and Stern Layer Formation, ***2014***

CIMTEC, 6th Forum on New Materials, June 15-19, 2014, Montecatini Terme, Italy **(Oral Presentation)**

- The influence of ferroelectricity on the photocatalytic activity of heterogeneous catalyst –$BaTiO_3$/α-Fe_2O_3, ***2015 E-MRS Spring Meeting, May 11-15, 2015, Lille, France*** **(Poster)**
- The influence of ferroelectricity on the photocatalytic activity of heterogeneous catalyst –$BaTiO_3$/α-Fe_2O_3 , ***2015 Joint IEEE International Symposium on Applications of Ferroelectric (ISAF), International Symposium on Integrated Functionalities (ISIF), and Piezoresponse Force Microscopy Workshop (PFM) (ISAF-ISIF-PFM 2015), May 24-27, 2015, Singapore,*** **(Oral presentation)**

Appendix B—Awards and Honours

- Second Prize of Oral Presentation, The 20th Joint Annual Conference of CSCST-SCI (Chinese Science & Technology in the UK and the SCI Chinese UK Group), September 14, 2013, London, UK
- Best Poster, 2015 E-MRS(European Materials Research Society) Spring Meeting, Symposium N, May 11-15, 2015, Lille, France
- Honourable Mention, 2015 ABTA(Association of British Turkish Academics) Doctoral Researcher Awards, May 16, 2015, London, UK

Acknowledgements

I would like to thank my supervisor Dr. Steve Dunn, who guided me through my PhD project in the past four years. He was always there to cheer me up when I was frustrated, give me a clue when I was stuck, and make me feel comfortable to study in UK. From the discussions with him, I developed my research skills and learned how to become a qualified researcher. I also really appreciate Dr. Joe Briscoe, who provided me lots of brilliant ideas and suggestions. He was kind and patient to spare his time to discuss with me on my projects. I would also like to thank Dr. Steve Goldup, who helped me a lot with chemical experiments and analysis. My sincere thanks also go to Dr. Rory Wilson, Dr. Nadja Tarakina, Dr. Krystelle Mafina, Dr. Zofia Luklinska, Dr. Ian Sandersand, Dr. Harold Toms and Mr Russell Bailey, who assisted me in gathering the experimental data of my work. Furthermore, I would like to thank my lovely colleagues and friends. It is them who make a fantastic studying atmosphere around me. Their encouragement and support helped me to go through the stressful moments and made my PhD life a colourful and unforgettable experience in my life.

My thanks also go to my beloved family, my parents and my elder sister. Although they know little about my PhD projects, they always back me up, care about me, and support me no matter how far I live from them. Without them, I will never achieve this. My special thanks go to my girlfriend Miss Zhen Xu, whose considerate care and support aid me to overcome the troubles and go through my PhD.

Lastly, I would like to appreciate Chinese Scholarship Council for providing me with financial support for my PhD program.